A SINGLE-STAGE PASSIVE VIBRATION ISOLATION SYSTEM FOR SCANNING

TUNNELING MICROSCOPY

A Thesis

presented to

the Faculty of California Polytechnic State University,

San Luis Obispo

In Partial Fulfillment

of the Requirements for the Degree

Master of Science in Mechanical Engineering

by

Toan Le

August 2020

COMMITTEE MEMBERSHIP

TITLE: A Single-stage Passive Vibration Isolation System
          for Scanning Tunneling Microscopy

AUTHOR: Toan Le

DATE SUBMITTED: August 2020

COMMITTEE CHAIR: Eltahry Elghandour, Ph.D.
                    Professor of Mechanical Engineering

COMMITTEE MEMBER: Gregory Scott, Ph.D.
                     Professor of Chemistry and Biochemistry

COMMITTEE MEMBER: Hemanth Porumamilla, Ph.D.
                     Professor of Mechanical Engineering

ABSTRACT

A Single-stage Passive Vibration Isolation System for Scanning Tunneling
Microscopy

Toan Le

Scanning Tunneling Microscopy (STM) uses quantum tunneling effect to study the surfaces of materials on an atomic scale. Since the probe of the microscope is on the order of nanometers away from the surface, the device is prone to noises due to vibrations from the surroundings. To minimize the random noises and floor vibrations, passive vibration isolation is a commonly used technique due to its low cost and simpler design compared to active vibration isolation, especially when the entire vibration isolation system (VIS) stays inside an Ultra High Vacuum (UHV) environment. This research aims to analyze and build a single-stage passive VIS for an STM. The VIS consists of a mass-spring system staying inside an aluminum hollow tube. The mass-spring system is comprised of a circular copper stage suspended by a combination of six extension springs, and the STM stays on top of the copper stage. Magnetic damping with neodymium magnets, which induces eddy currents in the copper conductor, is the primary damping method to reduce the vibrations transferred to the mass-spring system. FEMM and MATLAB® are used to model magnetic flux density and damping coefficients from eddy current effect, which will help determine the necessary damping ratios for the VIS. Viton, which demonstrates a high compatibility with vacuum environments, will also serve as a great damping material between joints and contacts for the housing tube. Viton will be modeled as a Mooney-Rivlin hyperelastic material whose material parameters are previous studied, and Abaqus will be used as a Finite Element Analysis software to study the Viton gaskets' natural frequencies. The natural frequencies of the aluminum hollow tube will also be investigated through Abaqus.

Keywords: dynamics, vibrations, scanning tunneling microscope, Viton, viscoelastic, visco-hyperelastic, eddy currents, magnetic damping, FEA, MATLAB®, Abaqus, FEMM.

ACKNOWLEDGMENTS

To my family

my mom, my dad, my sister

for all the times I must choose between what is easy and what is right

TABLE OF CONTENTS

LIST OF TABLES

LIST OF FIGURES

Chapter 1

INTRODUCTION

1.1 BACKGROUND

In the early 1980s, Gerd Binnig, Heinrich Rohrer, Christoph Gerber, and Edmund Weibel successfully built a Scanning Tunneling Microscope (STM) in the IBM Research Laboratory in Zurich, Switzerland. The STM uses the quantum tunneling effect to study surfaces of materials on an atomic scale. The instrument consists of a probe (typically a metal tip) scanning just above a conductive surface. When the two conducting electrodes at different voltage potentials are separated by a very thin insulating barrier (air or vacuum), the electrons can penetrate this barrier and establish a small flow of current.[19] Although staying very close to each other, the electrodes are not actually in physical contact, which allows the tunneling effect to occur due to the wave-particle duality of electrons. Since the quantum tunneling effect decays exponentially[10] with the increasing distance between the scanning tip and the surface of the conductive material, the distance between two electrodes must be kept within a few angstroms to just a few nanometers (Figure 1.1).
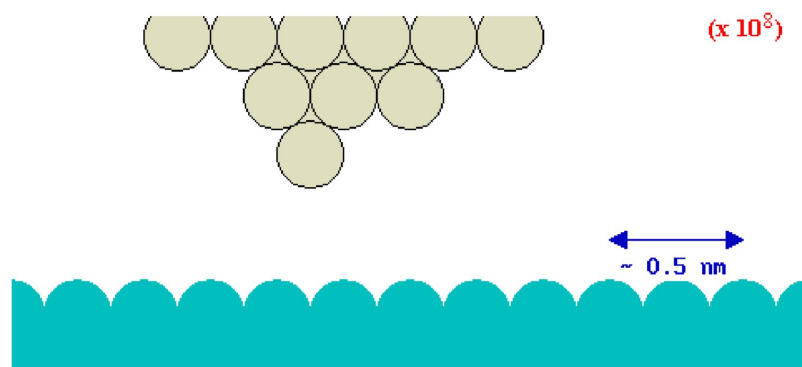
Figure 1.1: An atomic scale view with the STM tip and material's surface[27]

Constructing a working STM, therefore, is a challenging task. The original design of a Binnig and Rohrer's STM, shown in Figure 1.2, consists of a base L, which is positioned

by a piezoelectric three-legged stepper with electrostatically clampable feet. By adjusting voltage applied to base L, the stepper crawls forward to move sample S into a tunneling range of tip T. The piezoelectric positioners X, Y, and Z then move tip T into an exact relationship with sample S.[19] The entire STM stays on a Vibration Isolation System (VIS) P, which keeps the whole system mechanically stable and isolates any random noises and floor vibrations that will disturb the STM while it is running.
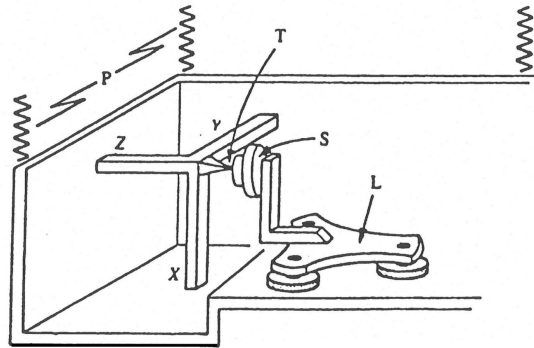
Figure 1.2: A schematic of the Binnig and Rohrer's STM[19]

Once the tip and the sample are within the tunneling range, the STM can be operated under a constant height mode (CHM) or a constant current mode (CCM), which are shown in Figure 1.3. In the CHM, the tip-to-sample distance is kept as a constant by a closed-loop control system while tunneling current is recorded. This technique allows the tip to scan rapidly across the material's surface.[2] However, the surface must be relatively flat[28] in which the differences in altitude should be less than a few angstroms,[2] otherwise the tip can easily crash into the surface. Vice versa, in CCM, the current is maintained as a constant preset value, and the vertical tip position is continuously adjusted by a closed-loop feedback circuit.[2] By using either method, a topographic image in the sub-angstrom scale can be displayed. Figure 1.4 shows one of a first few images produced by the Binnig and Rohrer's STM. Because the invention of STM (and later the AFM or the Atomic Force Microscopy allowing non-conductive materials to be scanned) has opened up entirely new fields to study the structure of matters, Gerd Binnig and Heinrich Rohrer were awarded the Nobel Prize in Physics in 1986.

(a) Constant height mode (CHM)   (b) Constant current mode (CCM)
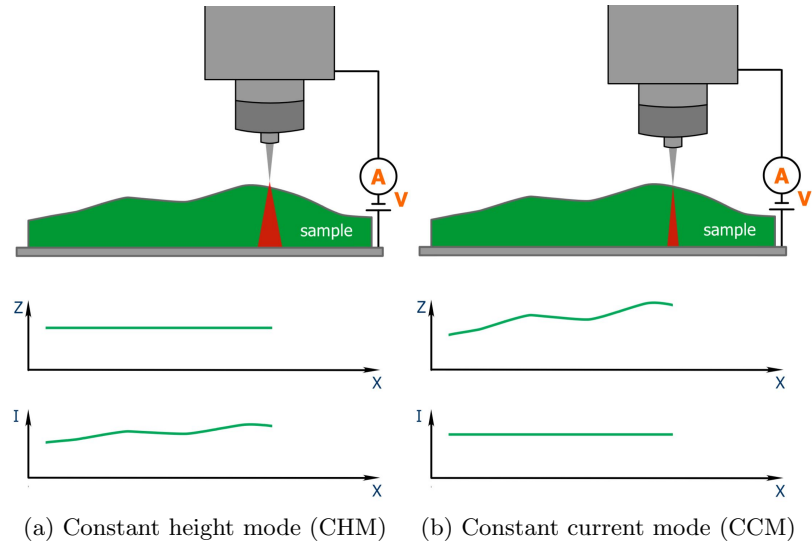
Figure 1.3: Two imaging methods for STM[28]
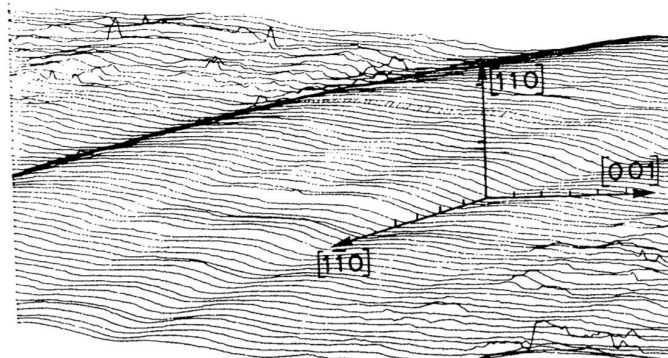
Figure 1.4: An STM's topography of a gold's surface at room temperature[3]

1.2 THE LYDING STM

The Lyding STM, which was originally developed by Professor Joe Lyding at the University of Illinois at Urbana-Champaign, is an extremely compact and rigid version of the STM.[19] Figure 1.5 shows the Lyding STM, which contains two concentric piezoelectric tubes: an outer and an inner tube. The outer tube is used to move the sample holder in the range of a few millimeters and to compensate for thermal changes. The inner tube has a scanning metal tip, which is mounted along the tube's center line and faces a vertical sample attached to a sample holder.

The outer tube is attached to a quartz tube through a thermal compensation collar. The material used for the collar is carefully chosen so that it expands and contracts at the same rate as the scanning metal tip. This will ensure that the tip-to-sample distance remains constant, and data acquisition can be performed over a wide range of ambient temperatures. The outer tube is metalized so that the outside is grounded, and voltages can be applied to the inside of the tube. The grounded outer surface provides shielding for the inside as well as the outside of the inner tube. By applying asymmetric sawtooth waveform to the inner surface, the piezoelectric outer tube will uniformly change its length and move the sample holder. With the ramp portion of the applied sawtooth signal, the outer tube contracts, and sample holder starts moving in one direction. Once the sample holder has gained some momentum, the sudden drop portion of the applied sawtooth signal jerks the rails back, which leaves the sample holder one step away from where it was. Reversing the symmetry of the sawtooth signal causes the sample holder to move in the other direction. This motion is referred to as the coarse sample translation.[19] By repeating this motion, the sample can be translated at a rate of 0.2 mm/s that is visible to the naked eye.[24]

The inner tube is used to finely adjust the tip-to-sample distance. Similarly to the outer tube, it is metalized, but the inner surface is grounded instead of the outer one, which helps provide coaxial shielding to the signal wires within the tube. The outer surface is divided into four quadrants, which is shown in Figure 1.6. With equal voltages applied to all four quadrants, the inner tube will change its thickness uniformly, so the tip can move in the z-axis. By applying equal but opposite voltages to quadrants 1 and 3, one quadrant becomes thinner while the other one gets thicker so that the inner tube can bend along the x-axis. Similarly, by applying equal but opposite signals to quadrants 2 and 4, the inner tube will deflect in the y direction. Since these movements are so small compared to the length of the inner tube, the motions are considered planar in the xy-plane. In addition, because the metalized quartz rail system is not level, gravity tends to pull the sample holder to the same position. Figure 1.7 shows two examples of surface images scanned by the Lyding STM. In Figure 1.7a, the red dashed line is approximately 25 nanometers long.
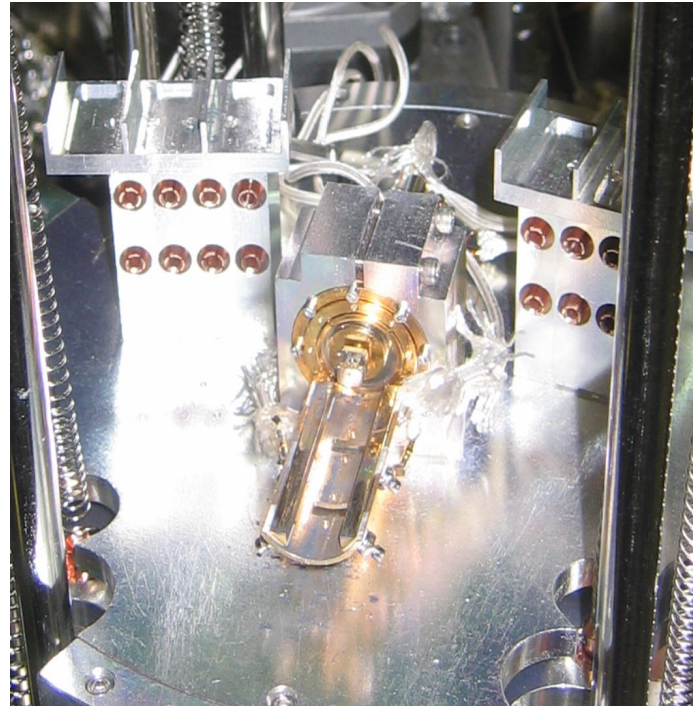
(a) The Lyding STM mounted on an Al stage with two storing units in the back
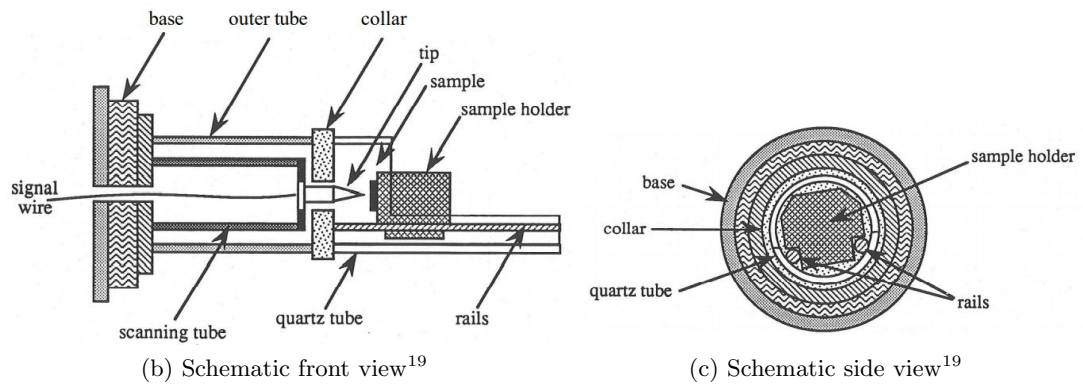
(b) Schematic front view[19]

(c) Schematic side view[19]

Figure 1.5: Configuration of the Lyding STM
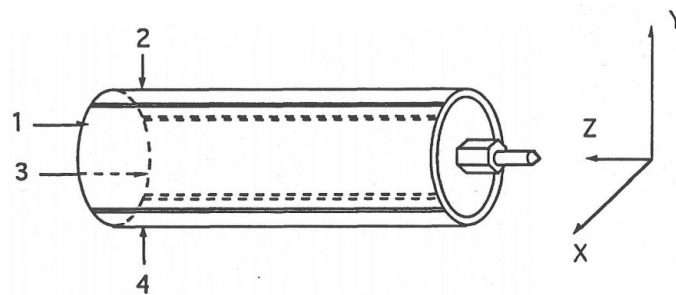
Figure 1.6: Inner tube of the Lyding STM[19]

(a) Carbon nanotube (white) on hydrogen-passivated silicon

(b) Clean silicon surface with Miller indices of (100)[39]
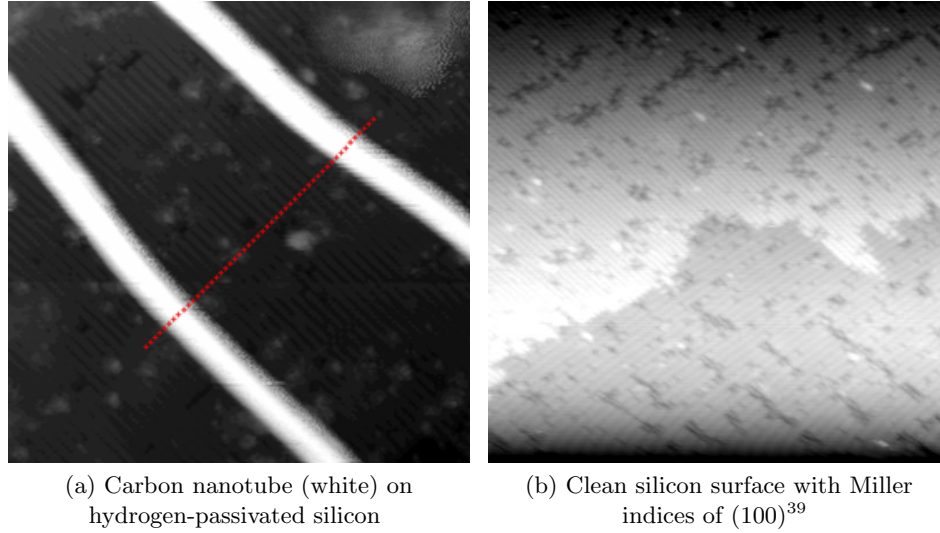
Figure 1.7: Scanned images (400x400 Å) from the Lyding STM

1.3 Previous Designs of VIS

The first VIS that Binnig and Rohrer built has permanent magnets levitating on a superconducting lead bowl (Figure 1.8a). To achieve the superconducting state, the lead bowl is cooled to a few Kelvin, and the system uses about 20 liters of liquid helium per hour.[2] The vacuum chamber is essentially "an exsicator with lots of Scotch tape." Later, this system was modified to have the VIS suspended by rubber bands instead, which indicates that superconducting levitation might be unnecessary.[2] Binnig and Rohrer discuss another VIS where the STM would stay on a stack of metal plates separated by Viton, which is an Ultra High Vacuum (UHV) compatible material (Figure 1.8b).

(a) First VIS with superconducting lead bowl

(b) VIS with metal stacks and Viton
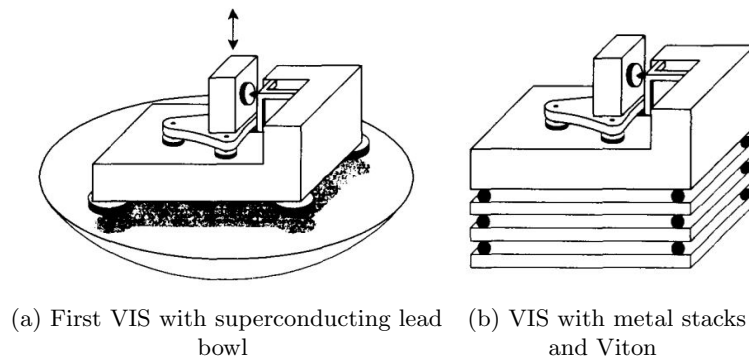
Figure 1.8: VIS designed by Binnig and Rohrer[2]

6

Multiple designs of VIS have been shown over the years. Okano *et al.* discuss two systems: a two-stage coil-spring VIS with eddy current dampers and a metal-stack system with rubber pieces among metal plates.[29] Figure 1.9 illustrates the two-stage system where a base frame (I) is directly connected to the vacuum chamber. The middle frame (II) is suspended from base frame (I) by three coil springs. The exterior frame (III) is then suspended from the middle frame (II) by three other coil springs. Each coil spring is terminated by a rubber ring to attenuate the high frequency propagating along the structure.[29] A magnet (V) is sandwiched between two copper blocks (IV and VI) to provide eddy current damping. This configuration prevents the vertical translational motion as well as the rotational motion about the center of gravity.
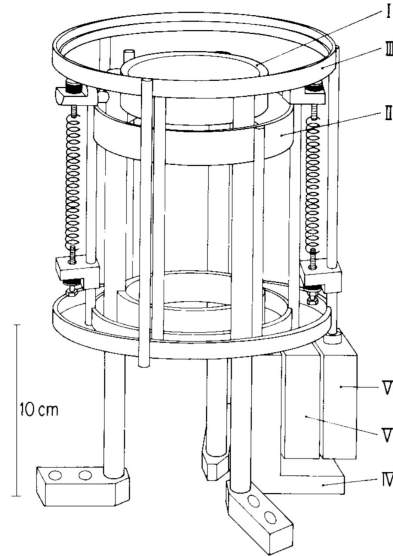
Figure 1.9: Two-stage coil-spring VIS, Okano *et al.*[29]

In the metal-stack VIS, Viton is sandwiched between five metal plates, and the system is designed such that the center of gravity can be adjusted as low as possible for each stage. However, the metal-stack design does not perform as well as the two-stage system.[29] To improve the isolation performance of the metal-stack VIS, Viton is replaced by coil springs at the lowest stack, and both Viton and coil springs are used in the second stack (Figure 1.10). The springs should be carefully chosen so that it will not be fully compressed under weight and will not be bent under load.[29]
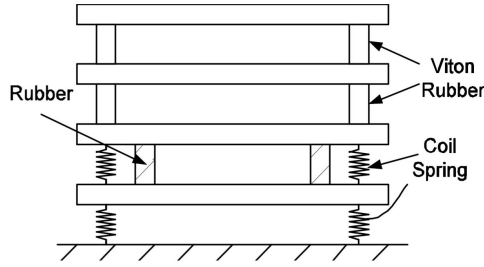
Figure 1.10: VIS with stack plates, Okano *et al.*[29]

Krapf *et al.* use an alternative approach, where the STM is attached on a rigid structure through a bellow (Figure 1.11a). The base structure, which is composed of a rigid tripod mounted on a concrete block, is designed to be as stiff as possible when connected to the ground.[22] The STM is mounted on a 3.5-inch UHV flange, which is linked to the vacuum chamber by a flexible welded bellow.[22] The stiff base structure helps minimize the effects of building vibrations on the STM[6] while the flexible bellow helps absorb any vibrations transferred to the STM.[22] Figure 1.11b shows a similar design developed at the National Institute of Standards and Technology (NIST). Four pneumatic vibration isolation legs support a concrete slab on which "a commercially available shear damped tripod" is mounted.[6] The STM stays in a cube-shaped structure, which is then hung from the vacuum chamber through some extension springs.

(a) Krapf *et al.*'s VIS   (b) NIST's VIS
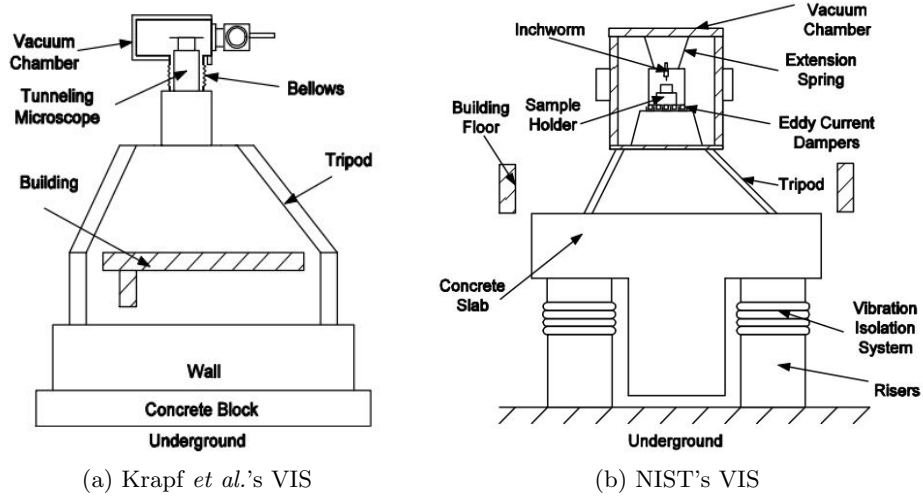
Figure 1.11: Designs of VIS with rigid frames[6]

A mass-spring system seems to be a common design for VIS because of the effectiveness of a suspended system. Figure 1.12 depicts a two-stage VIS used with the Lyding STM at the University of Illinois. This VIS features an aluminum (Al) top stage suspended from the top flange of the vacuum chamber by four vertical extension springs. Four other extension springs connect the Al bottom stage to the top flange as well. Four rods are used to mount the bottom copper (Cu) disk at a fixed height from the top flange. Magnetic damping is applied to both the top and bottom Al stage. U-shape structures sitting on the bottom Al stage will hold magnet pairs facing Cu rectangular blocks, which are attached to the Al top stage. This will provide damping for the Al top stage on which the STM sits. The bottom Cu disk interacts with some magnets fixed to the Al bottom stage to provide magnetic damping for the bottom stage. Some other Cu cylinders are mounted to the top and bottom Al stage to add necessary weights in the confined space of the vacuum chamber.
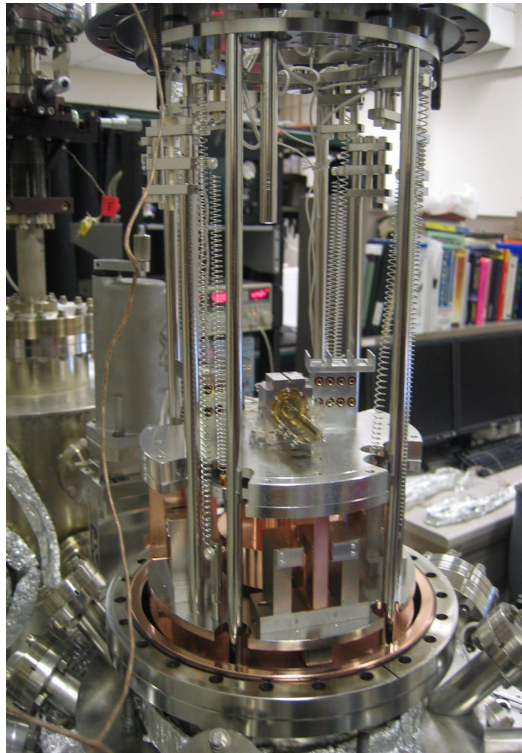
(a) Suspended VIS from the vacuum chamber's stainless steel flange
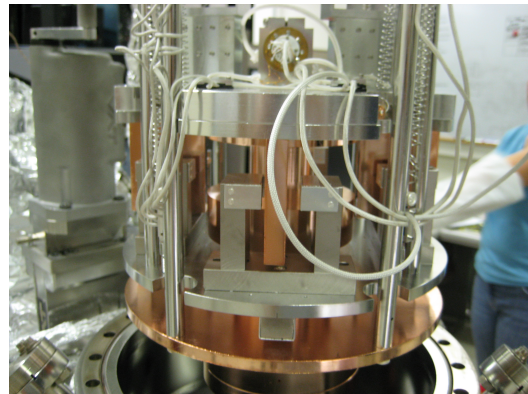
(b) A closer look at the Al top and Al bottom stage

Figure 1.12: A two-stage VIS used at the University of Illinois

1.4 Motivation for Research

Passive vibration isolation is a commonly used system due to its low cost and simpler design compared to active vibration isolation, especially when the entire VIS stays inside a UHV environment. Multi-stage VIS have been used previously, but this design is usually too complex and not cost-effective. Two-stage VIS, in particular, requires additional analyses and experiments compared to a single-stage VIS to ensure the vibration isolation performance of the system. In addition, many mass-spring systems for VIS only arrange extension springs vertically. This poses a challenge for such systems because the torsional stiffness about its center of gravity is often neglected. This thesis, as a result, aims to design, analyze, and build a single-stage passive VIS as well as its housing for the Lyding STM, which will be used in the existing vacuum chamber in a Chemistry lab at Cal Poly University. The single-stage VIS will be suspended by a combination of extension springs, and each spring will form an angle with respect to the main stage. This will help add torsional stiffness to the single-stage VIS.

1.5 Thesis Outline

Chapter 1 is to familiarize audience with the topics of STM and VIS. The remainder of the thesis will be divided into three main parts, and each part represents a topic contributing to the overall design of the VIS.

- Chapter 2 will discuss the dynamic and vibration model for the mass-spring system of the VIS. The base excitation model will be developed to select springs and mass of the main stage necessary for the VIS to achieve vibration isolation. Experiment data will be used to validate the design of the mass-spring system.

- Chapter 3 will present the simulation results for the natural frequency analyses of the aluminum housing as well as the Viton gasket. Abaqus is used as a Finite Element Analysis (FEA) software to extract the eigenvalues, which will be used to select the

housing structure and thickness of Viton gasket. Transient modal dynamics in Abaqus is also used to study the material's responses to an impulse load, which, in turn, demonstrates the damping capability of thick versus thin Viton gaskets.

- Chapter 4 will present the magnetic damping analysis. MATLAB® will be used as the main simulation tool. FEMM (Finite Element Method Magnetics), which is an open-source software, will be used to compare the magnetic flux density $\mathbf{B}$ produced by MATLAB® simulations. The damping coefficients and damping ratios will be shown as a function of gap distance between the copper main stage and the surface of neodymium magnets. These results will be used to select the types and geometry of magnets, as well as providing design constraint for the aluminum housing tube.

At the end, Chapter 5 will summarize the research and propose future work necessary for the development of the VIS.

Chapter 2

DYNAMIC AND VIBRATION ANALYSIS

2.1 Background

There are two models for the mass-spring system of the VIS: the base excitation and the direct excitation. The base excitation model, or sometimes referred to as the displacement transmissibility,[16] is used to model a VIS that could isolate a system of interest from the source of vibration. In the context of VIS for STM, it helps model the VIS to protect the delicate instrument (STM) from the random noises and floor vibrations from the surroundings. The direct excitation model, or usually referred to as the force transmissibility,[16] is used to model a system that protects the ground from vibrations of the mass. In other words, if a vacuum pump is installed, the VIS for this pump should be modeled as a direct excitation model since the force and frequency from this pump is detrimental to the STM. Both models can be readily formulated by drawing the free-body diagram (FBD) and kinetic diagram (KD). In the following sections, the derivation of the base excitation model will be shown. The direct excitation model can be developed in a very similar way, or it could be looked up in most textbooks about mechanical vibrations, such as Inman's *Engineering Vibration*.

2.2 Modes of Vibration

The suspended mass-spring system has six degrees of freedom (DOF). Figure 2.1 shows three translational and three rotational vectors in x, y, and z direction. Vertical mode refers to the translational movement of the stage in the vertical z direction. Yaw mode refers to the rotational movement about z-axis through the centroid. Roll mode is the rotation about x-axis, which then defines pitch mode as the rotation about y-axis. Roll and pitch could be simply referred to as the rocking mode because these movements rock

the stage from side to side. This also means that roll, pitch, and rocking mode can be used interchangeably to refer to the same movement because of the symmetrical circular stage. In the following analyses, only the vertical and yaw mode are considered. The pitch/roll/rocking mode is very similar to the vertical mode, and the translation in the x-axis and y-axis are not considered as these modes are not as substantial as the translation in z direction.
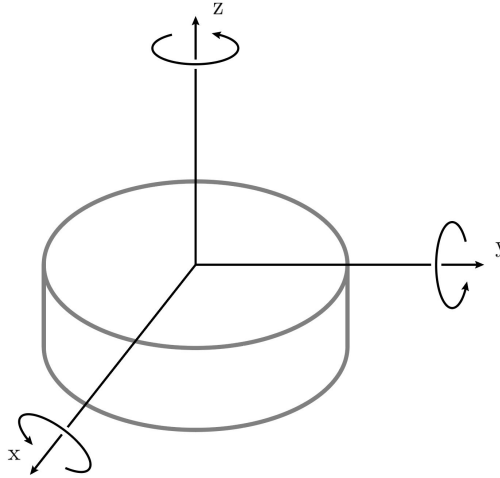
Figure 2.1: Modes of vibration for a 6 DOF system

2.3   Base Excitation Model

In this model, the vibration passing through the top cap of the Al housing is the source of vibration. The mass-spring system as a whole can be modeled as having a generic linear spring with vertical stiffness K_v and a generic viscous damper with vertical damping coefficient C_v. Figure 2.2 illustrates a diagram of the base excitation model. The excitation from the top cap of the housing is assumed to be a sinusoidal signal $y = Y \sin(\omega t)$ with an arbitrary forcing frequency ω. Without loss of generality, assume that the magnitude of displacement, velocity, and acceleration of the top cap is larger than those of the main stage, i.e. $y > z$, $\dot{y} > \dot{z}$, and $\ddot{y} > \ddot{z}$. These assumptions allow us to define the direction for the force vectors, so the magnitude of each force vector should be a positive quantity. The

magnitude of the spring force is then defined as $F_s = K_v(y - z)$, and the magnitude of the viscous damping force is $F_d = C_v(\dot{y} - \dot{z})$.
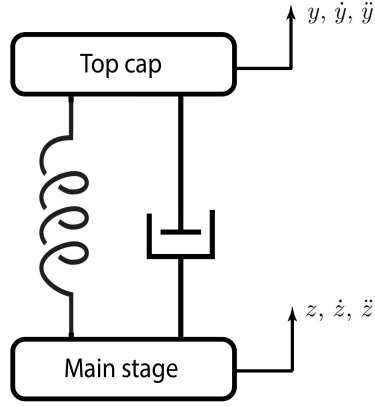
Figure 2.2: Base excitation diagram

Figure 2.3 shows the corresponding FBD and KD of the base excitation model. The inertia force $M\ddot{z}$ must be in the same direction as the positive acceleration defined in Figure 2.2 for the stage. In this scenario, the force causes the acceleration; hence, the resultant vector of F_s and F_d is in the same direction as $M\ddot{z}$ vector.
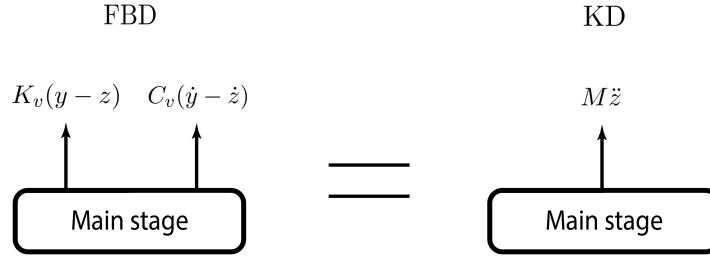
Figure 2.3: FBD and KD of base excitation model

Summing the forces in the vertical direction, we have

$$\left(\sum \overrightarrow{F}_{\text{vertical}} \right)_{\text{FBD}} = \left(\sum \overrightarrow{F}_{\text{vertical}} \right)_{\text{KD}} \tag{2.1}$$

$$K_v(y - z) + C_v(\dot{y} - \dot{z}) = M\ddot{z} \tag{2.2}$$

$$M\ddot{z} + C_v\dot{z} + K_v z = C_v\dot{y} + K_v y \tag{2.3}$$

14

Equation 2.3 above is a linear non-homogeneous ordinary differential equation (ODE). Its general solution consists of one complementary solution and *two* particular solutions. The complementary solution, or homogeneous solution, is found by solving the homogeneous equation. Predictably, the particular solution, or non-homogeneous solution, is found by solving the non-homogeneous equation for *each* forcing function. The homogeneous form of Equation 2.3 is

$$M\ddot{z} + C_v\dot{z} + K_v z = 0 \tag{2.4}$$

$$\ddot{z} + \frac{C_v}{M}\dot{z} + \frac{K_v}{M}z = 0 \tag{2.5}$$

Let the solution for this homogeneous equation be

$$z(t) = Ae^{\lambda t} \tag{2.6}$$

Differentiating Equation 2.6 twice with respect to time t and substituting them to Equation 2.5, the *characteristic equation* is then defined as

$$\lambda^2 + \frac{C_v}{M}\lambda + \frac{K_v}{M} = 0 \tag{2.7}$$

This quadratic equation yields two solutions

$$\lambda_{1,2} = -\frac{C_v}{2M} \pm \frac{1}{2M}\sqrt{C_v^2 - 4K_v M} \tag{2.8}$$

The system is called *underdamped* if the discriminant $C_v^2 - 4K_v M < 0$. Both quadratic solutions λ_1 and λ_2 are imaginary, and the complementary solution has the form

$$z(t) = A_1 e^{\lambda_1 t} + A_2 e^{\lambda_2 t} \tag{2.9}$$

where A_1 and A_2 are coefficients to be determined by the initial conditions once the form of general solution is obtained. Further simplification can be applied by using Euler's formula $\left(e^{xj} = \cos x + j\sin x\right)$. If $C_v^2 - 4K_v M = 0$, the system is *critically damped*. The

15

complementary solution then has the form

$$z(t) = A_1 e^{\lambda_{1,2} t} + t A_2 e^{\lambda_{1,2} t} \qquad (2.10)$$

Finally, if $C_v^2 - 4K_v M > 0$, the system is *overdamped*, and the solution's form is similar to Equation 2.9. In all three cases, the forcing frequency ω does not show up in the solution since the complementary solution only expresses a family of solutions for the ODE. To find the specific response of the system to the forcing functions, we must consider the particular solutions.

By using the definition of natural frequency ($\omega_n^2 = K_v/M$) and the definition of damping ratio ($\zeta = C_v/C_v^{\text{crit}}$), we can rewrite Equation 2.3 as

$$\ddot{z} + 2\zeta\omega_n \dot{z} + \omega_n^2 z = 2\zeta\omega_n \dot{y} + \omega_n^2 y \qquad (2.11)$$

where the critical damping coefficient is defined as $C_v^{\text{crit}} = 2\sqrt{K_v M} = 2M\omega_n$ for convenience. Differentiating the sinusoidal signal twice and substituting these into Equation 2.11, we have

$$\ddot{z} + 2\zeta\omega_n \dot{z} + \omega_n^2 z = 2\zeta\omega_n \left(\omega Y \cos\omega t \right) + \omega_n^2 \left(Y \sin\omega t \right) \qquad (2.12)$$

Equation 2.12 is also a linear non-homogeneous ODE. The particular solution $z_p^1(t)$ for the first forcing function $2\zeta\omega_n(\omega Y \cos\omega t)$ can be found by using Method of Undetermined Coefficients, and the result is

$$z_p^1(t) = \frac{2\zeta\omega_n \omega Y}{\sqrt{(\omega_n^2 - \omega^2)^2 + (2\zeta\omega_n\omega)^2}} \cos\left(\omega t - \beta_1\right) \qquad (2.13)$$

where

$$\beta_1 = \arctan\left(\frac{2\zeta\omega_n\omega}{\omega_n^2 - \omega^2} \right)$$

Similarly, by using the Method of Undetermined Coefficients, the particular solution $z_p^2(t)$ for the second forcing function $\omega_n^2(Y \sin \omega t)$ is

$$z_p^2(t) = \frac{\omega_n^2 Y}{\sqrt{(\omega_n^2 - \omega^2)^2 + (2\zeta\omega_n\omega)^2}} \sin(\omega t - \beta_1) \tag{2.14}$$

From the principle of linear superposition, the total particular solution will be the sum of each particular solution, so the total particular solution $z_p(t)$ is determined as

$$z_p(t) = z_p^1(t) + z_p^2(t) \tag{2.15}$$

$$z_p(t) = \left[\omega_n Y \sqrt{\frac{\omega_n^2 + (2\zeta\omega)^2}{(\omega_n^2 - \omega^2)^2 + (2\zeta\omega_n\omega)^2}} \right]$$
$$\times \left\{ \left[\frac{2\zeta\omega}{\sqrt{\omega_n^2 + (2\zeta\omega)^2}} \right] \cos(\omega t - \beta_1) + \left[\frac{\omega_n}{\sqrt{\omega_n^2 + (2\zeta\omega)^2}} \right] \sin(\omega t - \beta_1) \right\} \tag{2.16}$$

$$z_p(t) = \left[\omega_n Y \sqrt{\frac{\omega_n^2 + (2\zeta\omega)^2}{(\omega_n^2 - \omega^2)^2 + (2\zeta\omega_n\omega)^2}} \right]$$
$$\times \left[\cos\beta_2 \cos(\omega t - \beta_1) + \sin\beta_2 \sin(\omega t - \beta_1) \right] \tag{2.17}$$

$$z_p(t) = \left[\omega_n Y \sqrt{\frac{\omega_n^2 + (2\zeta\omega)^2}{(\omega_n^2 - \omega^2)^2 + (2\zeta\omega_n\omega)^2}} \right] \times \cos(\omega t - \beta_1 - \beta_2) \tag{2.18}$$

where

$$\beta_2 = \arctan\left(\frac{\omega_n}{2\zeta\omega}\right)$$

Let the amplitude of $z_p(t)$ be Z, we then have

$$Z = \omega_n Y \sqrt{\frac{\omega_n^2 + (2\zeta\omega)^2}{(\omega_n^2 - \omega^2)^2 + (2\zeta\omega_n\omega)^2}} \tag{2.19}$$

$$\frac{Z}{Y} = \sqrt{\frac{1 + (2\zeta r)^2}{(1 - r^2)^2 + (2\zeta r)^2}} \tag{2.20}$$

where the frequency ratio $r = \omega/\omega_n$. Equation 2.20 expresses the displacement response of the system to the input displacement magnitude, and it is used to described how motion is transmitted from the housing cap to mass M.

Figure 2.4 shows the plot of displacement ratio Z/Y as a function of frequency ratio r with varying damping ratio ζ. From this plot, it is clear that once $\omega/\omega_n \geq \sqrt{2}$, vibration isolation is achieved: less motion is transferred through the top cap into the main stage ($Z/Y \leq 1$). Although increasing damping ratio is effective around resonance, high damping ratios will have an opposite effect in the vibration isolation region and actually reduce the effectiveness of the mass-spring system. As a result, careful calculations, experiments, and simulations are important to control the right amount of damping ratio for the VIS's mass-spring system.
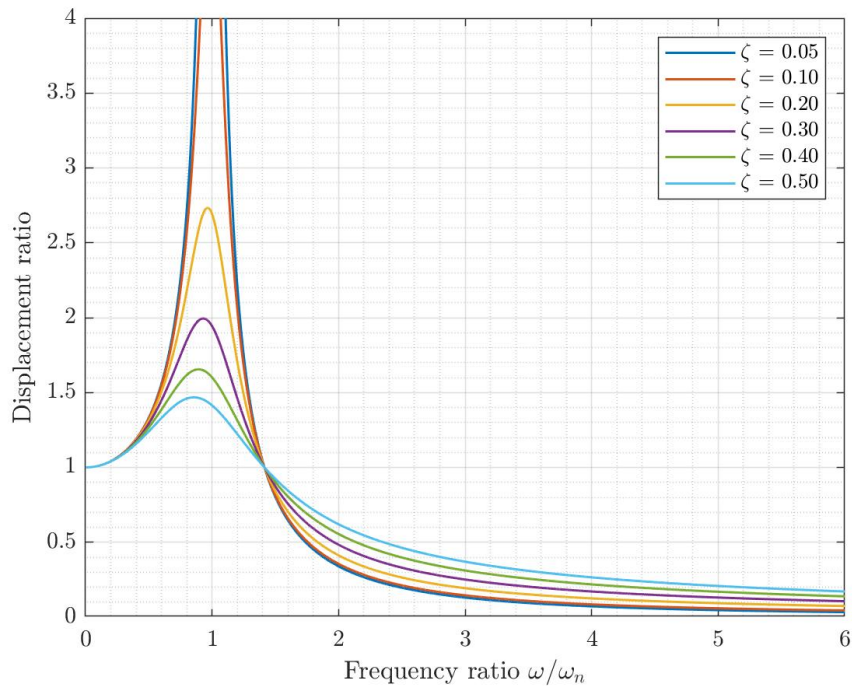
Figure 2.4: Displacement transmissibility of a base excitation model

2.4 INPUT FREQUENCIES

One of the challenges of designing a VIS is to understand the inputs to the system. This depends widely from place to place and from time to time. Even on the same floor of a building, the excitation frequencies and their magnitudes vary depending on a number of factors: the time of day, the number of running equipment, the number of people walking

around the lab, etc. Fortunately, we can estimate the frequency range of the excitation and design the VIS accordingly. Figure 2.5 generalizes the range of input frequencies to the STM. High frequency vibration induced by vacuum pumps and other equipment are much higher than 100 Hz while random vibrations caused by human activities are categorized as low frequency vibration, which is below 100 Hz.
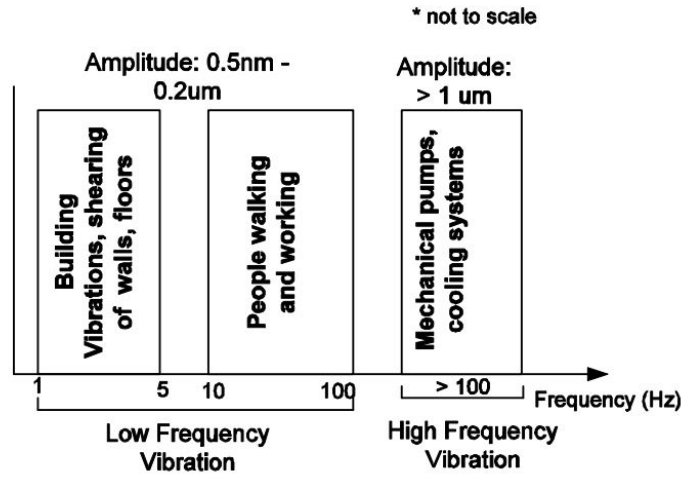
Figure 2.5: Suggested low and high frequency range[6]

Figure 2.6 further explains the low frequency range by showing the typical floor vibration spectra in three different labs. Although these labs are in different locations, their vibration spectra share some common characteristics that we can use to estimate the input frequencies to the VIS.

In Figure 2.6a, the solid curve represents measurements from the accelerometer, and the solid bars show the corresponding displacement amplitudes, which is calculated as follows

$$\frac{|y|}{|\ddot{y}|} = \frac{|Y \sin \omega t|}{|-Y\omega^2 \sin \omega t|} = \frac{1}{\omega^2} \tag{2.21}$$

In this IBM Lab, the building shear and bending vibrations occur between 15–25 Hz.[32] The highest displacement amplitude of approximately 0.2 μm appears near 17 Hz. The peaks at 50 Hz and 100 Hz are less pronounced, probably because they are off-resonance with regard to the lowest-order floor eigenfrequency.[32] The peak at zero is an instrumental artifact,

19
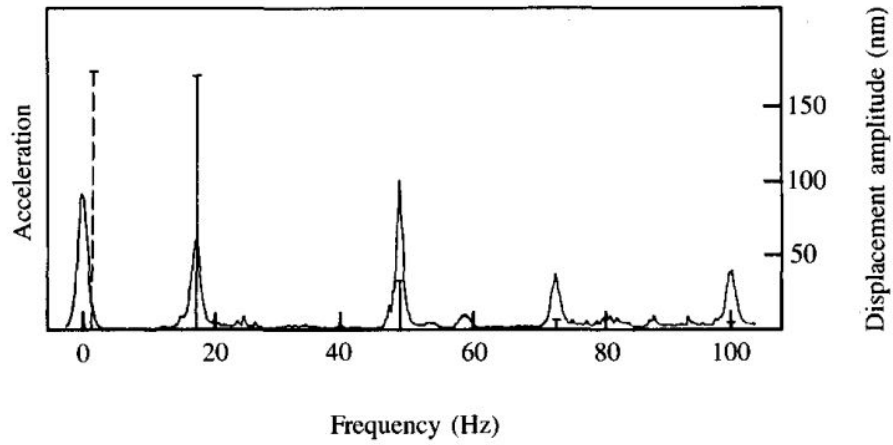
(a) Floor vibration in the IBM Lab[32]
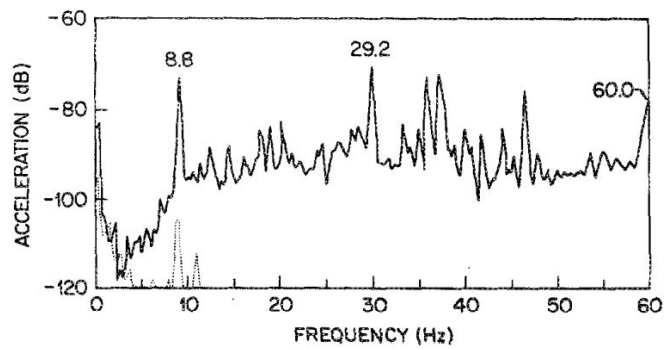
(b) Floor vibration in the AT&T Bell Lab[45]
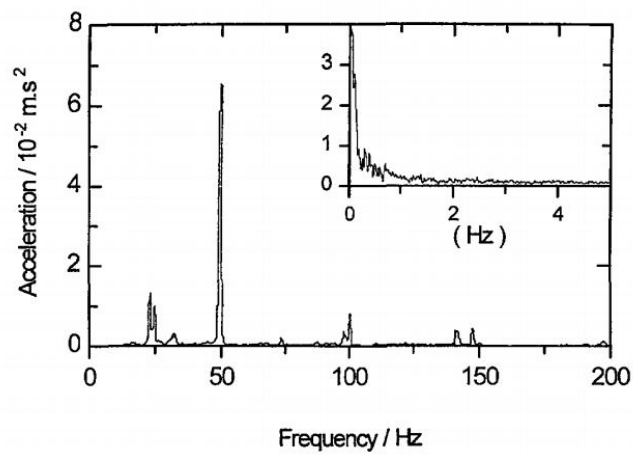
(c) Floor vibration in a lab in France[22]

Figure 2.6: Vertical floor vibration spectrum measured in different labs

which can be ignored. The dashed vertical bar at about 1–3 Hz represents irregular motions caused by people walking and working in the lab. Primary attention, therefore, has to be given to the frequency range between 1–100 Hz.[32]

Figure 2.6b shows similar conclusions but from different sources of inputs. The solid curve represents acceleration with its first peak at 1–3 Hz. The peaks at approximately 9, 29, and 60 Hz originated from ventilation ducts, motors, and transformers respectively.[45]

Figure 2.6c shows four distinguishable peaks in the acceleration plot. The first vibration amplitude reaches a maximum value of 0.13 µm at approximately 25 Hz in the vertical direction, and the second amplitude peak of 0.67 µm is at about 50 Hz. The peaks at about 100 Hz and near 150 Hz are small, but they agree with the categorization in Figure 2.5. The inset for Figure 2.6c represents the underground acceleration magnitude where the peak near 0 Hz is an artifact due to the accelerometer.[22]

Overall, measurements in person should be done once the VIS is completely built to investigate floor vibrations in the Chemistry lab at Cal Poly. However, it is clear that without using vacuum pumps, the VIS should be designed to isolate effectively the input frequencies between 1–100 Hz, since this is mostly encountered in lab environment due to human's activities and building vibrations. The natural frequency of the mass-spring system, therefore, should be close to 1 Hz, so regardless of what input frequencies traveling through the VIS, they will be in the vibration isolation region.

2.5   ANGLED SPRING CONFIGURATION

As discussed in Chapter 1, many VIS with mass-spring systems use only vertical springs to isolate vibrations for vertical mode. To add torsional stiffness about the center of gravity, either a torsional spring or a different configuration of the extension springs should be employed. Using a torsional spring requires a more complex design with additional features in the main stage to hold the torsional spring's legs. In addition, the torsional spring must be fixed with respect to the moving mass-spring system. This requires other

damping solutions since the input vibrations can travel through the torsional spring into the main stage. As a result, a different configuration for the extension springs becomes an attractive idea. Figure 2.7 shows a schematic of such configuration. Two adjacent extension springs are mounted vertically at the rim of the main stage, and they are arranged so that each of them forms an angle ϕ with respect to the main stage. There should be no radial component for any spring because such component is not useful for any mode. By considering each pair as a group and combining multiple groups to suspend the main stage, not only is the VIS suspended similarly to the vertical spring system, but this configuration also provides torsional stiffness inherently without the need for a torsional spring.
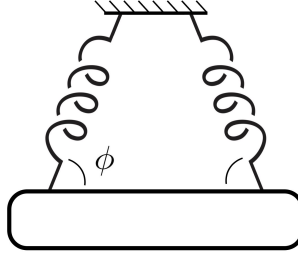
Figure 2.7: A pair of vertical extension springs forming an angle ϕ with main stage

The overall stiffness of the VIS needs to be reconsidered since the arrangement of the springs is no longer vertical. Each linear spring's stiffness, k, will be split into the vertical component (k_v) and horizontal component (k_h) as follows

$$k_v = k \sin \phi \tag{2.22}$$

$$k_h = k \cos \phi \tag{2.23}$$

The overall vertical stiffness K_v for the vertical mode will be the linear combination of n linear springs

$$K_v = n k_v \tag{2.24}$$

$$K_v = n k \sin \phi \tag{2.25}$$

In yaw mode, only one extension spring in each pair is engaged for each rotation direction. The overall tangential stiffness K_t for the yaw mode can be written as

$$K_t = \frac{n}{2}k_h \tag{2.26}$$

$$K_t = \frac{n}{2}k\cos\phi \tag{2.27}$$

2.5.1 NATURAL FREQUENCY OF VERTICAL MODE

Substituting Equation 2.25 into the definition of natural frequency ($\omega_n^2 = K_v/M$) of a rectilinear system, the natural frequency in the vertical direction then becomes

$$\omega_{n,v} = \sqrt{\frac{K_v}{M}} \tag{2.28}$$

$$\omega_{n,v} = \sqrt{\frac{nk\sin\phi}{M}} \tag{2.29}$$

Using Equation 2.29 and the limit for vibration isolation ($\omega/\omega_n \geq \sqrt{2}$) discussed above, we can derive the relationship between the stiffness of one extension spring and mass of stage necessary to achieve vibration isolation

$$\omega \geq \omega_{n,v}\sqrt{2} \tag{2.30}$$

$$\omega \geq \sqrt{\frac{2nk\sin\phi}{M}} \tag{2.31}$$

$$M \geq \frac{2nk\sin\phi}{\omega^2} \tag{2.32}$$

Equation 2.32 indicates the minimum required mass of the main stage to achieve vibration isolation for the VIS, where n extension springs—each with stiffness k—are used, and the input frequency to the VIS is ω.

Similar to the vertical mode, the natural frequency of the rotational system can be defined through an equation of motion. Figure 2.8 illustrates a diagram of the yaw mode. An illustrative linear spring is attached to the circular stage at the rim to represent the overall tangential spring constant K_t produced by the angled spring configuration. Without loss of generality, we can assumed the positive direction of $\theta, \dot{\theta}$, and $\ddot{\theta}$ to be counter-clockwise.
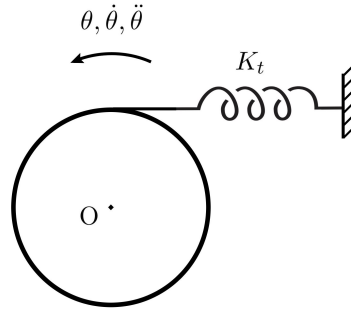
Figure 2.8: Yaw mode diagram

Figure 2.9 shows the corresponding FBD and KD for the yaw mode diagram. The spring force F_t represents the overall tangential force caused by the angled springs in tension. The torsional damping moment M_c due to magnetic damping, which is not shown in the yaw mode diagram above, is in the opposite direction of the assumed motion. The inertia couple $\bar{I}_z \ddot{\theta}$ is in the same direction as the positive angular acceleration defined in Figure 2.8.
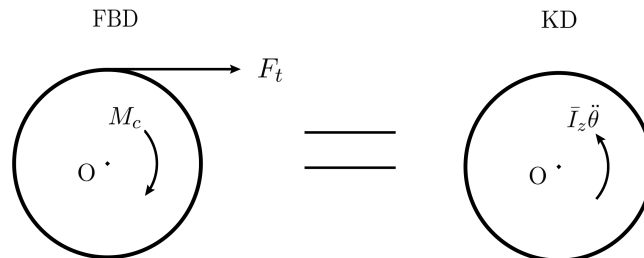
Figure 2.9: FBD and KD for yaw mode

Summing the moment about center O, we have

$$\left(\sum \vec{M}_O\right)_{\text{FBD}} = \left(\sum \vec{M}_O\right)_{\text{KD}} \tag{2.33}$$

$$-R_s F_t - M_c = \bar{I}_z \ddot{\theta} \tag{2.34}$$

$$\bar{I}_z \ddot{\theta} + M_c + R_s F_t = 0 \tag{2.35}$$

$$\bar{I}_z \ddot{\theta} + \bar{R} F_c + R_s F_t = 0 \tag{2.36}$$

where $\bar{I}_z$ is the centroidal moment of inertia, R_s is the radius of the main stage, and $\bar{R}$ is the distance from the centroid of the stage to the magnetic damping vector F_c. Equation 2.36 is a 2$^{\text{nd}}$-order homogeneous ODE whose solution represents the response of the main stage to an angular initial condition. The non-homogeneous ODE form of yaw mode with sinusoidal forcing functions can be analyzed similarly to that of the vertical mode, which will yield the same conclusion for the displacement transmissibility as shown in Figure 2.4.

Using the tangential stiffness K_t derived in Equation 2.27 as well as small angle approximation for $\sin\theta$, we can rewrite F_t as

$$F_t = K_t \left(\Delta x\right) \tag{2.37}$$

$$F_t = K_t \left(R_s \sin\theta\right) \tag{2.38}$$

$$F_t = \left(\frac{n}{2} k \cos\phi\right) \left(R_s \sin\theta\right) \tag{2.39}$$

$$F_t = \left(\frac{n}{2} k R_s \cos\phi\right) \theta \tag{2.40}$$

Moreover, if the magnetic damping is a type of viscous damping, the magnitude of the magnetic damping force can be described similarly to the linear viscous damping force for vertical mode: the force is proportional to the linear velocity. We can then describe F_c as

$$F_c = C_y v_\theta \tag{2.41}$$

$$F_c = C_y \bar{R} \dot{\theta} \tag{2.42}$$

25

where the relationship between linear velocity v_θ and angular velocity $\dot\theta$ is invoked. As a result, Equation 2.36 can be expanded to

$$\bar I_z \ddot\theta + C_y \bar R^2 \dot\theta + \left(\frac{n}{2} k R_s^2 \cos\phi\right)\theta = 0 \tag{2.43}$$

$$\bar I_z \ddot\theta + C_y \bar R^2 \dot\theta + \kappa\theta = 0 \tag{2.44}$$

Using the definition of natural frequency $(\omega_n^2 = \kappa/\bar I_z)$ for a rotational system, we can determine the natural frequency for the yaw mode as

$$\omega_{n,y} = \sqrt{\frac{\kappa}{\bar I_z}} \tag{2.45}$$

$$\omega_{n,y} = \sqrt{\frac{n}{2} k R_s^2 \cos\phi \frac{1}{\bar I_z}} \tag{2.46}$$

$$\omega_{n,y} = \sqrt{\frac{n}{2} k R_s^2 \cos\phi \frac{2}{M R_s^2}} \tag{2.47}$$

$$\omega_{n,y} = \sqrt{\frac{nk \cos\phi}{M}} \tag{2.48}$$

In addition, the discriminant for the yaw mode's characteristic equation is defined as $\Delta_y = (C_y \bar R^2)^2 - 4\bar I_z \kappa$, so the critical damping for yaw mode can be determined as

$$\Delta_y = 0 \tag{2.49}$$

$$(C_y^{\text{crit}} \bar R^2)^2 - 4\bar I_z \kappa = 0 \tag{2.50}$$

$$C_y^{\text{crit}} = \frac{2\sqrt{\bar I_z \kappa}}{\bar R^2} = \frac{2\bar I_z \omega_{n,y}}{\bar R^2} \tag{2.51}$$

Equation 2.48 can be used to calculate the natural frequency for yaw mode after the mass of stage and spring stiffness are chosen using Equation 2.32. The vertical mode, however, will be given priority because it is the most dominant mode for these systems and because the height of the vacuum chamber limits how long the extension springs can be. The following sections will discuss the selection process for extension springs so that the natural frequency for vertical mode should be as close to $1\,\text{Hz}$ as possible.

Before being able to select extension springs, we need to compile a list of available springs from different suppliers and compare them together. Figure 2.10 shows music wire springs collected from websites of two suppliers: Century Spring and The Spring Store.
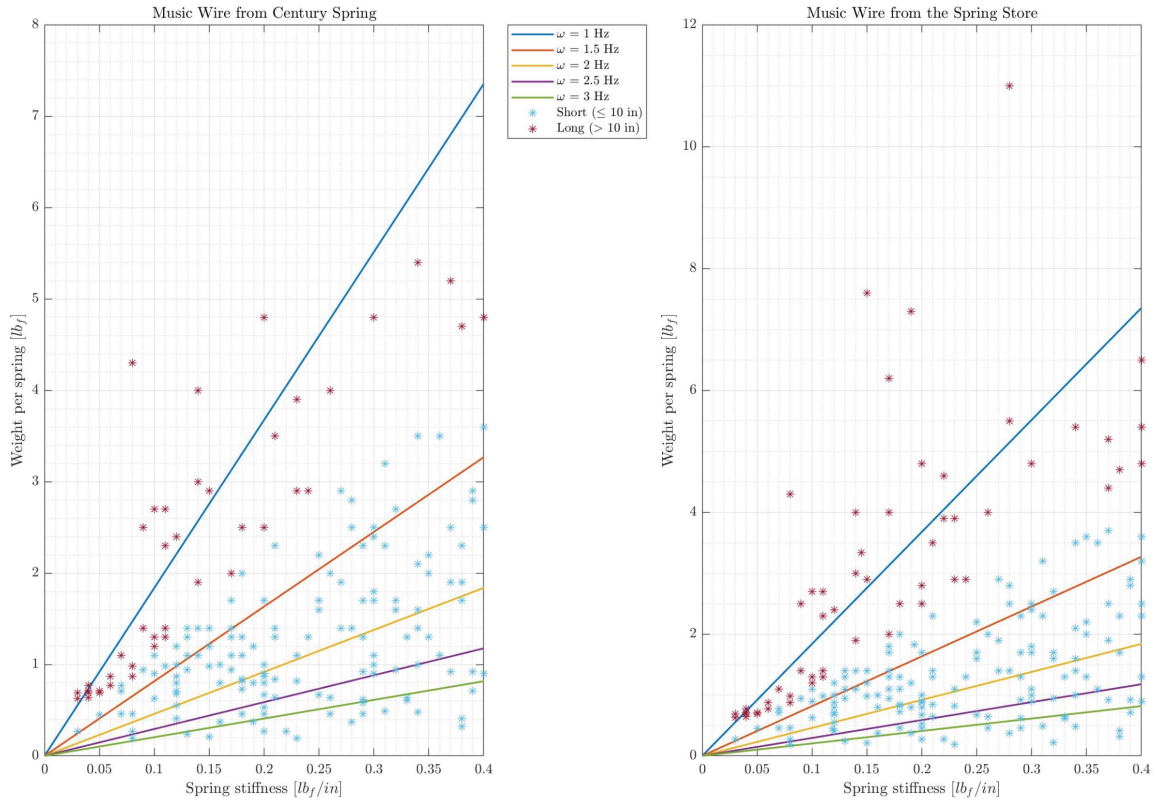
Figure 2.10: Music wire springs from 2 suppliers

Each dot represents a spring, and it is plotted based on the manufacturer's spring constant and the recommended maximum allowable load. The dots are categorized into red group (long springs with initial length > 10 inches) and blue group (short springs with initial length ≤ 10 inches). Assuming that n and ϕ are constants, the input frequencies ω is varied between 1–3 Hz with a 0.5 Hz interval. Since only the equality in Equation 2.32 is plotted as solid lines, it is implied that any spring above a given solid line will successfully isolate that frequency and any other input frequencies below it on the plot. In other words, considering all springs with stiffness of $0.2\,\mathrm{lb_f}/\mathrm{in}$ from Century Spring, for example, there is only one spring that is able to isolate the 1 Hz input vibration since this spring can

withstand a maximum load of $4.8\,\mathrm{lb_f}$ while only $3.7\,\mathrm{lb_f}$ is required to isolate $1\,\mathrm{Hz}$ input vibration. Since it can isolate the input frequency as low as $1\,\mathrm{Hz}$, higher frequencies can also be isolated by this spring. The selected music wire spring for validation experiment is purchased from The Spring Store (Part # PE030-500-103667), and its specifications provided by the manufacturer are shown in Table 2.1.

Table 2.1: Music wire spring used for the 8-spring experiment

Outer dia.	Wire dia.	Initial length	Spring constant	Max load	Initial tension
$0.5\,\mathrm{in}$	$0.03\,\mathrm{in}$	$3.8\,\mathrm{in}$	$0.1\,\mathrm{lb_f/in}$	$2.7\,\mathrm{lb_f}$	$0.1\,\mathrm{lb_f}$

Figure 2.11 shows a wooden frame built to hold 8 angled springs, and different sets of weights are put on a wooden stage to test against the mathematical model. Eight stud anchors with swivel heads are used on the wooden stage to allow free rotation for the springs' hooks so that none of the springs are twisted. The entire wooden frame is then placed on a shaker connected to a spectrum analyzer to collect data to a floppy disk. Since the mass-spring system has low stiffness and almost zero damping, an interval sine sweep is used instead of sweeping through the whole range of interested frequencies. The latter technique can present incorrect frequency responses as the shaker is sweeping at high frequencies while the stage is oscillating at its low natural frequency indefinitely[†]. Moreover, the former method allows us to observe carefully the effectiveness of the mass-spring system in isolating vibration for each interval. An interval of $0.5\,\mathrm{Hz}$ is used for inputs from 0.5–$2\,\mathrm{Hz}$, and an interval of $1\,\mathrm{Hz}$ is used for inputs from 2–$10\,\mathrm{Hz}$. Once data are collected, they are converted to MATLAB® data files.

Figure 2.12 illustrates the frequency response of the wooden stage with three sets of weights: $4\,\mathrm{kg}$, $5\,\mathrm{kg}$, and $6\,\mathrm{kg}$. Figure 2.12a shows the raw absolute magnitude data recorded from the accelerometer, and Figure 2.12b shows the same data plotted in dB scale using the relationship $y_{\mathrm{dB}} = 20\log_{10}(y_{\mathrm{abs}})$. As the main stage gets heavier, the natural frequency decreases as predicted. We can also observe that the vibration isolation starts at roughly 1–$2\,\mathrm{Hz}$ when the data lines cross below $0\,\mathrm{dB}$. This is the crossover frequency. When more

---

[†]Compared to only a few milliseconds required for equipment to collect and process data.

28

Figure 2.11: A test frame with 8 angled springs

weights are applied, however, the wooden frame does not hold up well, and the top starts swinging from side to side instead of just moving up and down as the vertical motion of the shaker. This unintended effect can be seen through the more jagged yellow line compared to the relatively smoother red and blue lines. In Figure 2.12a, the max absolute magnitude of the 6 kg stage is 4 times less than that of the 4 kg because the main stage motion is split between vertical and rocking modes. As a result, we are not able to test the theoretical maximum load of 7.3 kg to achieve the best vibration isolation for the selected music wire springs. Following the trend in this frequency response plot, we can conclude that the higher frequencies can be effectively isolated, so the troubling frequencies are, in fact, the lower ones.

The 8-spring system is intended to be symmetrical so that each mode is uncoupled. However, the motion of the stage during testing suggests a different idea: when the top of the frame displaces from side to side, the symmetrical VIS stays in the rocking mode much longer than in the vertical or yaw mode. This somewhat defeats the purpose of designing the VIS for a dominant vertical mode. Hence, a more viable solution is to use an asymmetric
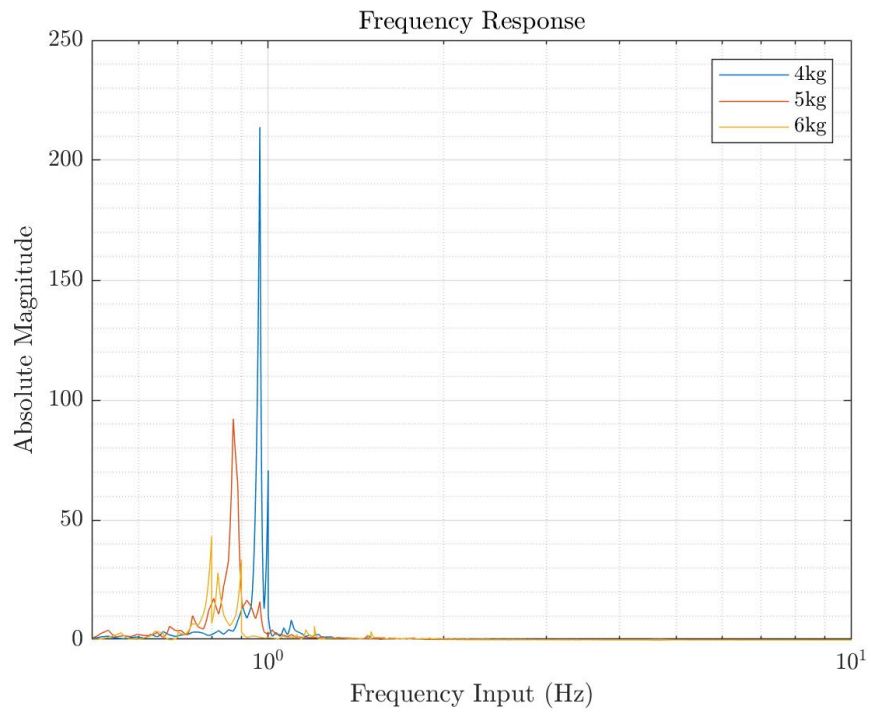
(a) Absolute magnitude recorded from accelerometer
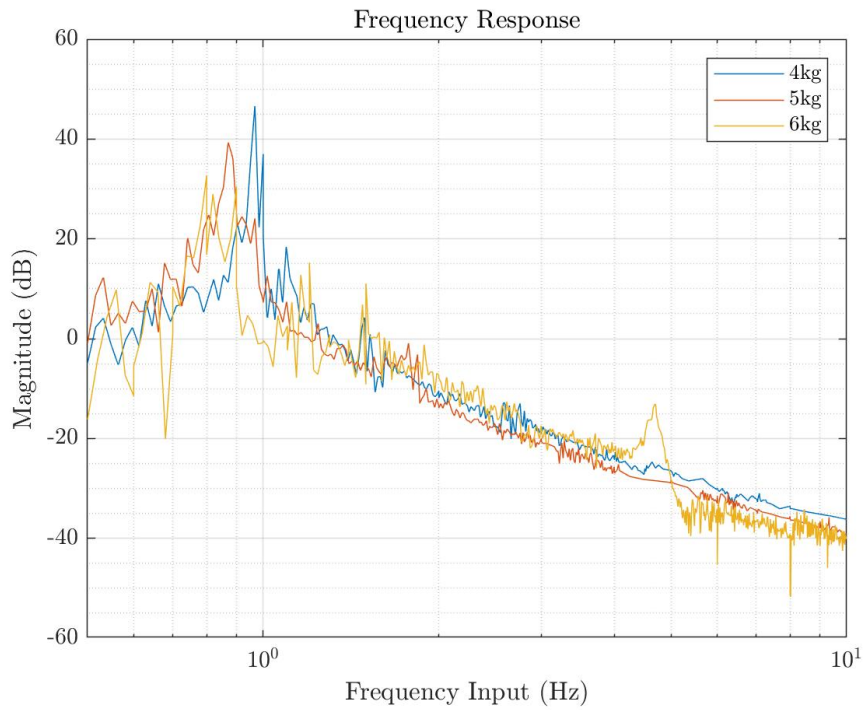
(b) Magnitude converted to dB scale

Figure 2.12: Frequency response of mass-spring system

system with 6 springs to balance between different modes. Fewer springs means that for the same weight of stage, VIS's natural frequency is lower, so a wider range of input frequencies can be isolated. More space beneath the main stage can also be saved for the installation of neodymium magnets.

2.7 6-SPRING SYSTEM

Once the mathematical model is verified, the materials of the main stage and springs must be considered for the actual system to be used in the vacuum chamber. Firstly, since the VIS is a single-stage system, a Cu stage is more favorable than an Al stage considering the tight space in the vacuum chamber. For the same weight, an Al stage takes up three times as much volume as a Cu stage. Not only is Cu vacuum compatible, but a Cu stage can also be used as a conductor for magnetic damping, which can eliminate the need for Cu blocks hanging from an Al stage. Figure 2.13 shows a machined Cu stage for the VIS. The Cu stage weighs 3.95 kg.
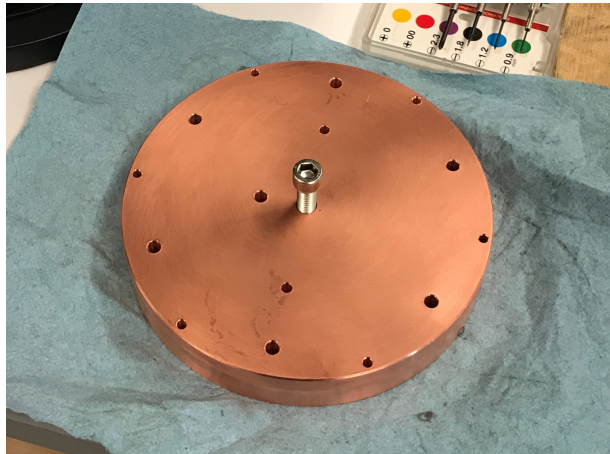
Figure 2.13: A machined Cu stage for VIS

Secondly, instead of music wire, stainless steel extension springs should be used. The vacuum compatible material list recommended by LIGO Laboratory[7] favors the use of stainless steel springs because of its low outgassing property compared to music wire springs made out of carbon steel. Figure 2.14 shows stainless steel springs collected from websites of two suppliers: Century Spring and The Spring Store. Similarly to Figure 2.10,

each dot represents a spring, and it is plotted based on the manufacturer's spring constant and the maximum allowable load. The linear solid lines represents the equality in Equation 2.32, and they implies that any spring above a given solid line will effectively isolate the vibration frequencies below it. Only one spring with stiffness of $0.17\,\mathrm{lb_f}/\mathrm{in}$ can theoretically isolate frequency as low as $1\,\mathrm{Hz}$, but applying max load to this spring causes the Cu stage to touch the bottom of the vacuum chamber. Therefore, we will use the Cu stage at its current weight and will only add extra weights to the stage once the gap between magnets and Cu stage is determined.
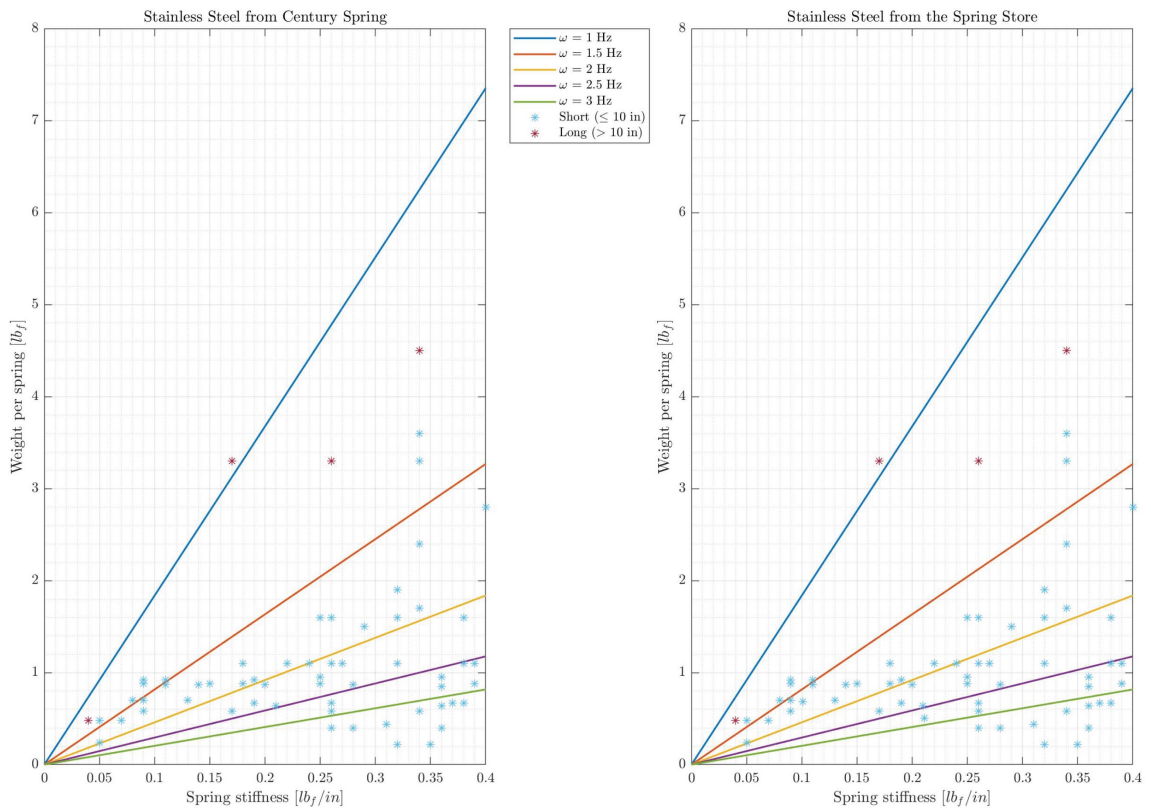
Figure 2.14: Stainless steel springs from 2 suppliers

Table 2.2 shows the manufacturer's specifications of the stainless steel springs purchased from Century Spring (Part # 80657S).

Table 2.2: Stainless steel spring used with Cu stage

Outer dia.	Wire dia.	Initial length	Spring constant	Max load	Initial tension
$0.5\,\mathrm{in}$	$0.036\,\mathrm{in}$	$5\,\mathrm{in}$	$0.17\,\mathrm{lb_f}/\mathrm{in}$	$3.3\,\mathrm{lb_f}$	$0.3\,\mathrm{lb_f}$

Using the spring's specifications in Table 2.2 and the formulas in Shigley's textbook,[4] we can calculate the spring's axial length, vertical length with respect to the Cu stage, and spring stiffness, which are shown in Table 2.3. Appendix A details the MALAB® code used for the calculations.

Table 2.3: Calculated lengths & stiffness of the stainless steel spring

Axial length	Vertical length	Spring stiffness
11.26 in	11.09 in	0.1836 lb$_f$/in

With the current weight of Cu stage and the calculated spring stiffness from manufacturer's specifications, the VIS is expected to have its vertical natural frequency between 1–1.5 Hz, and the vibration isolation should starts at about 1.5 Hz. The discrepancy of spring stiffness between our calculations and the manufacturer's data indicates that tolerances in manufacturing process, especially for the wire and outer diameters, affect the accuracy in determining the spring constant. For example, if the wire diameter assumes the value of 0.037 in while other specifications remain the same, the spring stiffness and axial length become 0.212 lb$_f$/in and 10.708 in respectively. The change of 0.001 in of the wire diameter is very small and within the tolerance of machining capability, so we need to recalculate the natural frequency of each mode from a different perspective. Figure 2.15 shows the measured axial length of one spring in the 6-spring system with the Lyding STM on top of the Cu stage. Using this measured length of 10.1 in, we can calculate the effective spring stiffness using standard Hooke's law for each spring as

$$F = k_{\text{eff}} \Delta x \tag{2.52}$$

$$\frac{M}{6} g = k_{\text{eff}} \left(10.1'' - 5'' \right) \tag{2.53}$$

$$k_{\text{eff}} = \frac{Mg}{6 \left(0.25654 \, \text{m} - 0.127 \, \text{m} \right)} \tag{2.54}$$

$$k_{\text{eff}} = 49.855 \, \text{N/m} \tag{2.55}$$

where $g = 9.81 \, \text{m/s}^2$ is the acceleration of gravity. All units are converted to standard SI units. Then, using Equation 2.29 and Equation 2.48, we can recalculate the natural

frequency of $1.38\,\mathrm{Hz}$ for the vertical mode, which is very close to our estimation above, and the natural frequency of $0.48\,\mathrm{Hz}$ for the yaw mode.
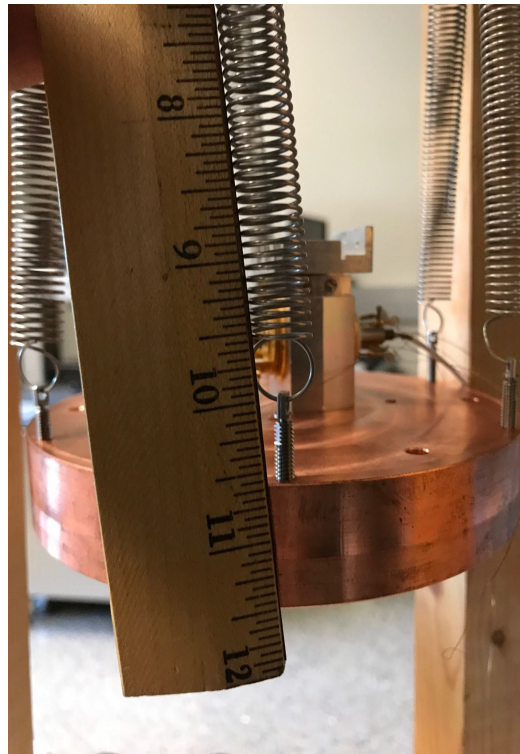
Figure 2.15: Axial length of 6-spring system with Cu stage

Chapter 3

FINITE ELEMENT ANALYSIS

3.1 BACKGROUND

In Chapter 2, the mass-spring VIS is analyzed as a 6-DOF system because the springs' stiffness is much lower than the stage's stiffness, so the Cu stage can be considered rigid. For solid bodies such that the material stiffness is high and the solid structures can no longer be considered perfectly rigid, a different method of analysis must be used for such multiple-DOF systems: the Finite Element Method.

The earliest utilization of minimum energy principles in structural design was proposed by Rayleigh in the late 1800s, which was then extended by Ritz in the early 1900s to a more general framework. Galerkin, in 1915, developed the integral concept of the method of weighted residuals, which is the basis of modern development of Finite Element Analysis (FEA) today. By 1940s, numerical techniques for the boundary value problems were developed with the use of matrix methods. However, not until 1960s was the term FEA coined by Ray Clough, and the development of the numerical method began to flourish with the advance of digital computers. In the late 1980s, commercial software became available in personal computers.[21]

3.2 THE FEA PROCESS

The Finite Element Method, in essence, converts a strong form of the differential equations describing a structure or domain and its corresponding boundary conditions into an integral form—weak form—because the original strong form could be extremely difficult to find the solution using conventional methods. During the process, the domain, whether it is a solid body or a fluid region, is divided into small elements connected by nodes, and

an approximate form of the solution is substituted into the weak form to find the governing equations for each element. The element equations are then assembled appropriately into the global domain to form a system of linear algebraic equations,[21] which could be solved using matrix operation. In the following sections, a few critical steps and concepts are discussed. However, the description should not replace numerous fundamental textbooks about this topic, such as *The Finite Element Method* by Thomas Hughes. Once the concepts are discussed, the natural frequencies of the housing structure for VIS as well as the Viton gaskets can be studied.

3.2.1 PROBLEM DEFINITION & BOUNDARY CONDITIONS

Figure 3.1 shows a 1-dimensional (1D) cantilever beam subjected to a known displacement $\bar{u}$ at the left end, an internal body force per unit length $\vec{b}$, and a point load $\vec{P}$ applied at the right end. The FBD for an infinitesimal element of the beam is also illustrated, where $\vec{f}$ is the internal force and $\Delta\vec{f}$ is the infinitesimal change in internal force.
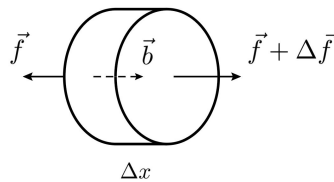
(a) An element of the cantilever beam
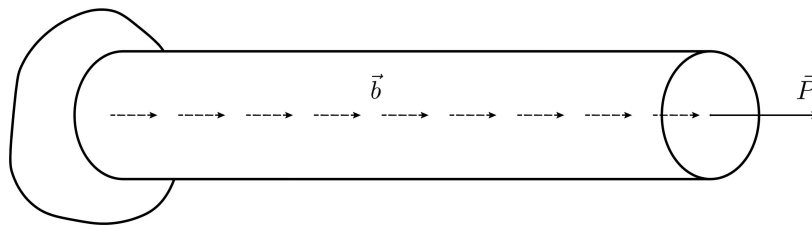
(b) A cantilever beam fixed at left end

Figure 3.1: A cantilever beam and its infinitesimal element

The differential equation for a beam infinitesimal element can be shown as

$$\sum \vec{F}_{\text{horizontal}} = 0 \tag{3.1}$$

$$-f + b\Delta x + f + \Delta f = 0 \tag{3.2}$$

$$b + \frac{\Delta f}{\Delta x} = 0 \tag{3.3}$$

$$b + \frac{d}{dx}(f) = 0 \tag{3.4}$$

$$b + \frac{d}{dx}(A\sigma_x) = 0 \tag{3.5}$$

$$b + \frac{d}{dx}(AE\varepsilon_x) = 0 \tag{3.6}$$

$$b + \frac{d}{dx}\left(AE\frac{du}{dx}\right) = 0 \tag{3.7}$$

$$b + AEu_{,xx} = 0 \tag{3.8}$$

where E is the Young's modulus, u is the axial displacement, the axial stress is related to axial strain by $\sigma_x = E\varepsilon_x$ assuming material is linearly elastic, and axial strain is defined as $\varepsilon_x = du/dx = u_{,x}$. As a result, the strong form (S) is described as follows

$$(\text{S}) \begin{cases} \text{Find } u(x) \text{ such that} \\[2mm] AEu_{,xx} + b = 0 \\[2mm] u(0) = \overline{u} \\[2mm] AEu_{,x}(L) = P \end{cases} \tag{3.9}$$

In commercial FEA software with Graphic User Interface (GUI) such as Abaqus, when we define the sketch, its shape, and boundary conditions (BC), the software will assign the appropriate form of equations as well as the BC values to the geometry, so users do not need to derive the strong form over again. To convert this strong form (S) into a weak form (W), the weighted-residual method will be used. Hence, the weak form can also be referred to as the weighted-residual form in contrast to the strong form defined in Equation 3.9.[30] Moreover, the solutions for the weak form is identical to those of the strong form,[15] which encourages us to study the weak solution of the problem.

To define the weak form, we need to characterize two classes of functions: the trial (candidate) solutions and the weighting functions—variations.[15] The collection of trial solutions ($\mathcal{S}$) consists of all functions $u(x)$ such that they have square-integrable derivatives and take on the displacement BC.[15] In mathematical notation, the previous statement can be written as

$$\mathcal{S} = \left\{ u(x) \mid u(x) \in H^1, \ u(0) = \overline{u} \right\} \tag{3.10}$$

where squared-integrable functions are called H^1 functions and have the following condition

$$\int_0^L (u_{,x})^2 \ dx < \infty \tag{3.11}$$

For the 1D cantilever beam in Figure 3.1, the left end has displacement of $\overline{u}$, which is shown as $u(0) = \overline{u}$ in Equation 3.10. In other contexts, the displacement BC is generally referred to as the essential BC or Dirichlet BC.

The second collection of functions ($\mathcal{V}$) is very similar to the first one, except that we require the weighting functions to be homogeneous at the essential BC. For the 1D cantilever beam in Figure 3.1, this can be written as

$$\mathcal{V} = \left\{ w(x) \mid w(x) \in H^1, \ w(0) = 0 \right\} \tag{3.12}$$

Because the functions $w(x)$ are just *variations* of the actual displacement function or merely *virtual displacements*, their magnitude must be 0, which explains the homogeneous constraint. In fact, the formulations from strong form to weak form of this type can be called the virtual work, or virtual displacement, principles in mechanics,[15] which conveniently adds more names and complexities to our confusions! It is important to mention that even though both $u(0)$ and $w(0)$ have the same value of 0 if the cantilever beam in Figure 3.1 is fixed at the left end, the reasons are entirely different.

Multiplying $w(x)$ to both sides of the strong form in Equation 3.9 and integrating over the domain using integration by part, we can derive the weak form as follows

$$w(AEu_{,xx} + b) = 0 \tag{3.13}$$

$$AE \int_0^L wu_{,xx} \, dx + \int_0^L bw \, dx = 0 \tag{3.14}$$

$$AE \left[wu_{,x} \right]_0^L - AE \int_0^L (u_{,x}w_{,x}) \, dx + \int_0^L bw \, dx = 0 \tag{3.15}$$

$$AE \left[w(L)u_{,x}(L) - w(0)u_{,x}(0) \right] - AE \int_0^L (u_{,x}w_{,x}) \, dx + \int_0^L bw \, dx = 0 \tag{3.16}$$

$$AE \left[w(L)u_{,x}(L) \right] - AE \int_0^L (u_{,x}w_{,x}) \, dx + \int_0^L bw \, dx = 0 \tag{3.17}$$

Using the Dirichlet BC from Equation 3.9 and rearranging Equation 3.17, we can rewrite the weak form as

$$(W) \begin{cases} \text{Find } u \in \mathcal{S} \text{ such that for all } w \in \mathcal{V} \\[2mm] AE \int_0^L (u_{,x}w_{,x}) \, dx = \int_0^L bw \, dx + Pw(L) \end{cases} \tag{3.18}$$

As Equation 3.18 shows, the derivative for $u(x)$ decreases an order because the weighting function $w(x)$ is used to take on an order of derivative. This is particularly helpful in problems where the displacement has higher order derivatives.

So far, a few assumptions of the Galerkin method are introduced to derive the weak form in Equation 3.18. The first one is the displacement BC must be satisfied at the outset: the solution $u(x)$ is sought over a set of candidate functions that already take on the displacement BC.[30] This is established in the collection of trial functions $\mathcal{S}$. The second assumption is the homogeneous constraint on weighting functions: $w(0) = 0$. The third assumption is the limit of choices for $w(x)$ to ensure the same weighting functions are used at the boundary as well as in the domain. This is reflected in Equation 3.18 where a single form of $w(x)$ is used in both integrals and evaluated at the boundary L.

Once the weak form is derived, the Bubnov-Galerkin approximation method[†] can be used to approximate the actual solution of the weak form, which, in turn, gives an approximate solution for the strong form. In other words, the Bubnov-Galerkin approximation method provides a fairly general framework for the numerical solution of the strong form within the context of the weighted-residual formulation[30] that helps derive the weak form.

3.2.3 The Approximate Solution

The differential equation in Equation 3.9 can be solved easily by integrating it twice before substituting two BC to achieve the exact solution. However, the exact solution is not our main concern here since we want to establish a generic scheme to solve more complex strong forms by converting them to weak forms and then generalizing the approximate solution for those forms. The approximate solution, in contrast to the exact solution, follows a discretization process in which a collection of functions are used to express the approximate solution. The approximate solution $\widehat{u}(x)$ for the weak solution $u(x)$ can be described as a finite-dimensional collection of functions[15] such that

$$u(x) \approx \widehat{u}(x) = \sum_{A=1}^{n} N_A(x)d_A + N_0(x)\overline{u} \tag{3.19}$$

where $N_A(x)$ and $N_0(x)$ are interpolation functions or shape functions while d_i can be seen as unknown constants associated with each shape function $N_A(x)$ for now. The form of $\widehat{u}(x)$ is chosen so that it satisfies the displacement BC of $u(0) = \overline{u}$ by requiring all shape functions to be 0 at $x = 0$ except the shape function associated with $\overline{u}$. In other words, $N_A(0) = 0$ and $N_0(0) = 1$ so that

$$\widehat{u}(0) = \sum_{A=1}^{n} N_A(0)d_A + N_0(0)\overline{u} \tag{3.20}$$

$$\widehat{u}(0) = \overline{u} \tag{3.21}$$

[†]Generally referred to as the Galerkin approximation method in many textbooks.

The weighting function $w(x)$, by Galerkin approximation method, takes the form

$$w(x) = \sum_{A=1}^{n} N_A(x) c_A \tag{3.22}$$

where c_A's are arbitrary constants, and the same shape functions are used for both $w(x)$ and $\hat{u}(x)$ so that the homogeneous constraint is maintained: $w(0) = 0$. This is the most popular version of the Galerkin method.[30]

After discretizing the solution form, we can substitute Equation 3.19 and 3.22 into Equation 3.18. The subscript for $\hat{u}(x)$ is changed to avoid errors in indicial notation, and the Galerkin approximation form is derived as follows

$$AE \int_0^L \left[\left(\sum_{B=1}^{n} N_{B,x} d_B + N_{0,x} \bar{u} \right) \left(\sum_{A=1}^{n} N_{A,x} c_A \right) \right] dx = \\ \int_0^L b \left(\sum_{A=1}^{n} N_A c_A \right) dx + P \left(\sum_{A=1}^{n} N_A(L) c_A \right) \tag{3.23}$$

$$\sum_{A=1}^{n} c_A \left(\sum_{B=1}^{n} AE \int_0^L N_{A,x} N_{B,x}\, dx \right) d_B - \sum_{A=1}^{n} c_A \left(\int_0^L b N_A\, dx + P N_A(L) \right) \\ + \sum_{A=1}^{n} c_A \left(AE \int_0^L \bar{u} N_{0,x} N_{A,x}\, dx \right) dx = 0 \tag{3.24}$$

$$\sum_{A=1}^{n} c_A \left[\left(\sum_{B=1}^{n} AE \int_0^L N_{A,x} N_{B,x}\, dx \right) d_B \\ - \left(\int_0^L b N_A\, dx + P N_A(L) - AE \int_0^L \bar{u} N_{0,x} N_{A,x}\, dx \right) \right] = 0 \tag{3.25}$$

If we assign

$$K_{AB} = \sum_{B=1}^{n} AE \int_0^L N_{A,x} N_{B,x}\, dx$$

$$F_A = \int_0^L b N_A\, dx + P N_A(L) - AE \int_0^L \bar{u} N_{0,x} N_{A,x}\, dx$$

then Equation 3.25 can be rewritten as

$$\sum_{A=1}^{n} c_A \left(\sum_{B=1}^{n} K_{AB} d_B - F_A \right) = 0 \tag{3.26}$$

Since c_A's are arbitrary, each set of Equation 3.26 must be identically 0. Therefore, we have

$$\begin{cases} \sum_{B=1}^{n} K_{1B} d_B - F_1 = 0 & \text{for } A = 1 \\ \sum_{B=1}^{n} K_{2B} d_B - F_2 = 0 & \text{for } A = 2 \\ \cdots \\ \sum_{B=1}^{n} K_{nB} d_B - F_n = 0 & \text{for } A = n \end{cases} \tag{3.27}$$

$$\begin{cases} K_{11} d_1 + K_{12} d_2 + \cdots + K_{1n} d_n = F_1 \\ K_{21} d_1 + K_{22} d_2 + \cdots + K_{2n} d_n = F_2 \\ \cdots \\ K_{n1} d_1 + K_{n2} d_2 + \cdots + K_{nn} d_n = F_n \end{cases} \tag{3.28}$$

or in familiar matrix form

$$\begin{bmatrix} K_{11} & K_{12} & \cdots & K_{1n} \\ K_{21} & K_{22} & \cdots & K_{2n} \\ \vdots & \vdots & & \vdots \\ K_{n1} & K_{n2} & \cdots & K_{nn} \end{bmatrix} \times \begin{Bmatrix} d_1 \\ d_2 \\ \vdots \\ d_n \end{Bmatrix} = \begin{Bmatrix} F_1 \\ F_2 \\ \vdots \\ F_n \end{Bmatrix} \tag{3.29}$$

$$\mathbf{Kd} = \mathbf{F} \tag{3.30}$$

where $\mathbf{K}$ is the stiffness matrix, $\mathbf{d}$ is the displacement vector, and $\mathbf{F}$ is the force vector. In structural mechanics, $\mathbf{K}$ is sometimes referred to as the tangent matrix, and $\mathbf{F}$ is the load or residual vector.[21] The Galerkin approximation method leads to a coupled system of linear algebraic equations[15] in which the unknown vector $\mathbf{d}$ can be solved by $\mathbf{d} = \mathbf{K}^{-1}\mathbf{F}$

provided that $\mathbf{K}$ is invertible. Once the values of $\mathbf{d}$ are solved, we can substitute them back to Equation 3.19 to get the complete approximate solution for $\widehat{u}(x)$.

It is important to remember that in discretizing and approximating the exact solution, we construct the finite-dimensional approximation subspaces $\mathcal{S}^h$ and $\mathcal{V}^h$ of $\mathcal{S}$ and $\mathcal{V}$ such that $\mathcal{S}^h \subset \mathcal{S}$ and $\mathcal{V}^h \subset \mathcal{V}$.[15] The approximate solution $\widehat{u}(x)$ belongs to the subset $\mathcal{S}^h$, or $\widehat{u} \in \mathcal{S}^h$, and the collection of weighting functions $w(x)$ belongs to $\mathcal{V}^h$, or $w \in \mathcal{V}^h$. For a graphical interpretation, Figure 3.2 shows the approximate solution domain discretized by triangular shapes only partially covers the exact solution domain.
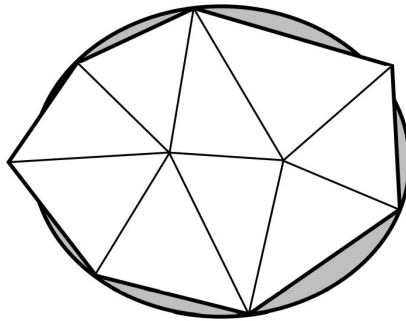
Figure 3.2: Finite element vs. exact domain[30]

3.2.4 ELEMENT TYPES

In Section 3.2.3, we discuss the approximate solution $\widehat{u}(x)$ for the entire domain L of the 1D cantilever beam. In practice, it is more common to discretize a geometric shape into small regions or subdomains with a characteristic length h representing the scale of the *mesh* based on the type of object being studied. A 1D cantilever beam, for example, can be discretized into finite element domains of straight or curved segments, which is shown in Figure 3.3. For a curved edge, an additional node is placed in between the end nodes.

Figure 3.3: Finite element domains in 1D[30]

Two-dimensional geometric shapes, such as plates or thin walls, can be discretized into finite element domains of triangles or quadrilaterals. Figure 3.4 illustrates examples of these shapes where the edges can be straight or curved.
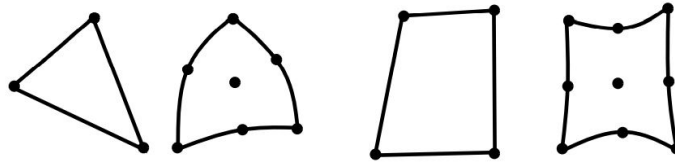
Figure 3.4: Finite element domains in 2D[30]

For three-dimensional objects, the most useful finite element domains are tetrahedral (tets), pentahedral (pies), and hexahedral (bricks) with either straight or curved edges and either flat or non-flat faces.[30] Pentahedral elements are sometimes called prisms or wedges. In Figure 3.5, two tetrahedral elements with straight and curved edges are shown along with straight-edged pentahedral and straight-edged hexahedral element.
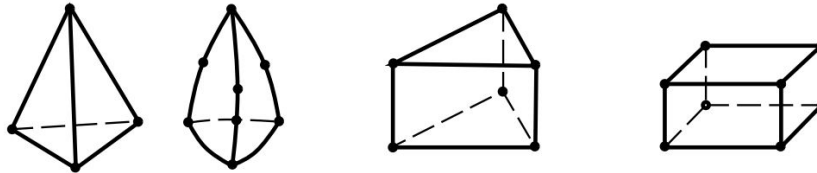
Figure 3.5: Finite element domains in 3D[30]

3.2.5 Shape Functions

For each element type discussed in the previous section, polynomial interpolation functions can be used in the approximate solution form among the nodes. A linear shape function between 2 nodes will result in a straight edge while a quadratic or cubic shape function connecting 3 nodes and 4 nodes respectively will result in a curved edge. Figure 3.6 shows two types of shape functions for a 1D element: linear shape functions for a 2-node element, and quadratic shape functions for a 3-node element. Each shape function, which

is associated with a node, has the value of 1 at the associated node while having the value of 0 at all of the other nodes in the element.
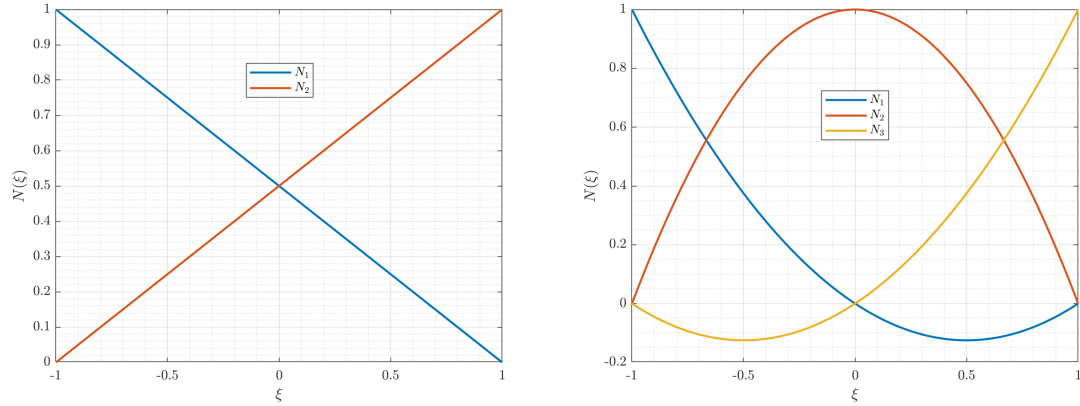
(a) Linear shape functions for a 2-node element   (b) Quadratic shape functions for a 3-node element

Figure 3.6: 1D shape functions plotted together

For the 1D shape functions, a two dimensional graph showing the locations ξ and magnitudes $N(\xi)$ at each node helps visualize the element. Similarly, 2D shape functions need a three dimensional graph to visualize the locations and magnitudes of the functions in an element. Figure 3.7 illustrates three type of shape functions for a 2D element: linear shape functions for a 3-node element, linear shape functions for a 4-node element, and quadratic shape functions for a 9-node element. The shape functions in Figure 3.7a are used for triangular elements while shape functions in Figure 3.7b and Figure 3.7c are for quadrilateral elements. Appendix B highlights the examples of MATLAB® codes used to plot the 2D shape functions of each element type. The shape functions for each 2D element type are also plotted together in Appendix B for visualization.

We may observe that the 4-node quadrilateral element in Figure 3.7b has nodeless interior while there is a node in the center of the 9-node quadrilateral element in Figure 3.7c. In fact, higher-order rectangular elements can be divided into two families based on the methodology used to generate them: the *serendipity* and the *Lagrangian* elements.[30] The polynomials in both families can be represented by Pascal's triangle, although each family has its own diagram to account for the noded or nodeless interior. Figure 3.8 shows the Pascal's triangle for each family. As the name suggested, the interpolation functions
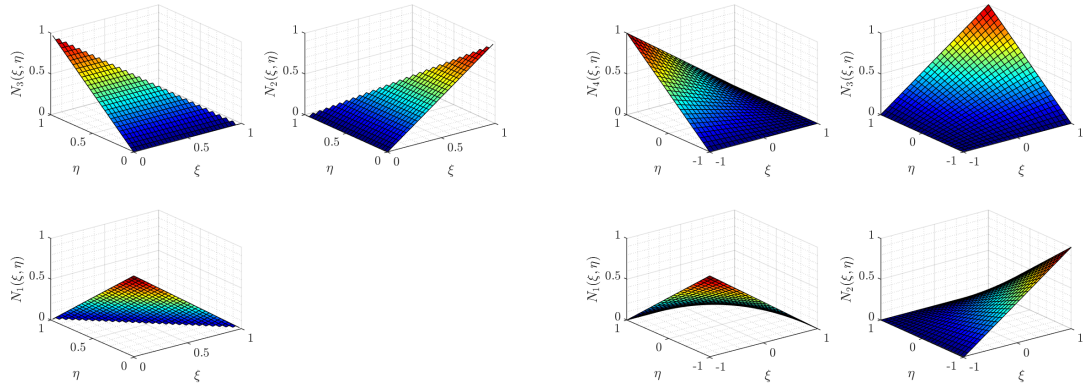
(a) Linear shape functions for a 3-node element

(b) Linear shape functions for a 4-node element
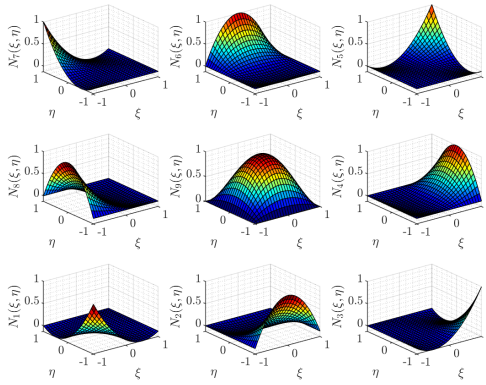
(c) Quadratic shape functions for a 9-node element

Figure 3.7: 2D shape functions plotted individually

of Lagrangian elements can also be determined trivially as products of one-dimensional Lagrange interpolation functions. A general expression for an nth-order Lagrangian interpolation function in one dimension is given as the product sum[21]

$$l_a^{n-1}(x) = \prod_{\substack{b=1 \\ b \neq a}}^{n} \frac{x - x_b}{x_a - x_b} \tag{3.31}$$

$$= \frac{(x - x_1)(x - x_2) \cdots (x - x_{a-1})(x - x_{a+1}) \cdots (x - x_n)}{(x_a - x_1)(x_a - x_2) \cdots (x_a - x_{a-1})(x_a - x_{a+1}) \cdots (x_a - x_n)} \tag{3.32}$$

where $n - 1$ is the degree of polynomial, and a is the nodal coordinate. To generate a 2D shape function at a node, we need to multiply the one dimensional polynomial in each

direction. For example, the center node in Figure 3.7c has the shape function of

$$N_9(x, y) = l_2^2(x) \times l_2^2(y) \tag{3.33}$$

where $l_2^2(x)$ is interpreted as the 2$^{\text{nd}}$-order polynomial for the second node from left to right in the x-direction, and $l_2^2(y)$ reads as the 2$^{\text{nd}}$-order polynomial for the second node in the y-direction. Each of them is defined as

$$l_2^2(x) = \frac{(x - x_8)(x - x_4)}{(x_9 - x_8)(x_9 - x_4)} \tag{3.34}$$

$$l_2^2(y) = \frac{(y - y_2)(y - y_6)}{(y_9 - y_2)(y_9 - y_6)} \tag{3.35}$$

where the subscripts are the neighbors' nodal numbers shown in Figure 3.7c. One of the advantages of using serendipity shape functions is having less equations to solve in the overall system of equations $\mathbf{Kd} = \mathbf{F}$. For example, an 8-node 2D quadrilateral element requires 16 equations to solve for 16 unknowns, which are essentially in the $\mathbf{d}$ array of Equation 3.29. A 9-node 2D quadrilateral element (Figure 3.7c) requires 18 equations. If a structure has tens of thousands of elements, we can really appreciate the computational time of a simpler element type.

(a) Serendipity family   (b) Lagrangian family
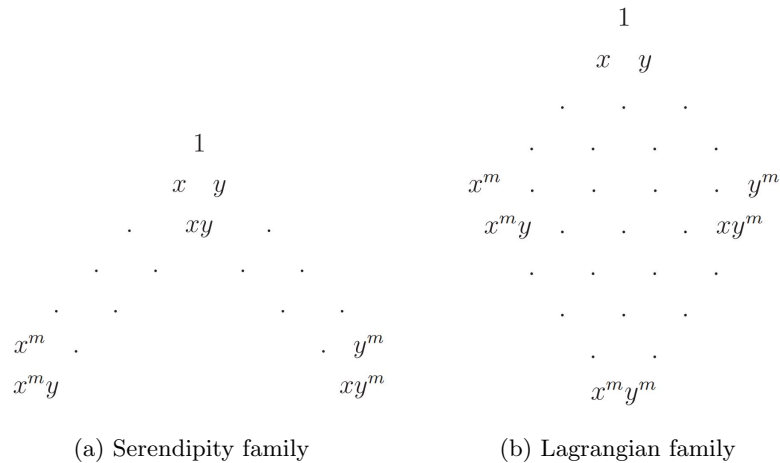
Figure 3.8: Pascal's triangle for 2D elements[30]

In general, higher-order shape functions, such as quadratic or cubic functions, allow us to capture more information between the nodes with the curved edges, which could help avoid some errors in the FEA process. One of the well-known issues of using linear shape functions for 2D quadrilateral elements is shear locking. Sheer locking occurs when the linear shape functions cannot capture the curved edge of a bending load, which causes the element to overestimate shear stress and appear stiffer than it should be. Figure 3.9 demonstrates the shear locking issue for a 2D quadrilateral element under a pure bending load M. To reserve the computational advantage of the elements with linear shape functions, the *incompatible modes* for linear elements may be used. This type of formulation adds internal displacement modes within an element to capture bending deformations.[21] These deformations are internal and do not add global degrees of freedom outside of the element. Since the internal displacement modes do not match across element boundaries, the formulation is named "incompatible modes".

(a) Correct elastic response (b) 4-node element response
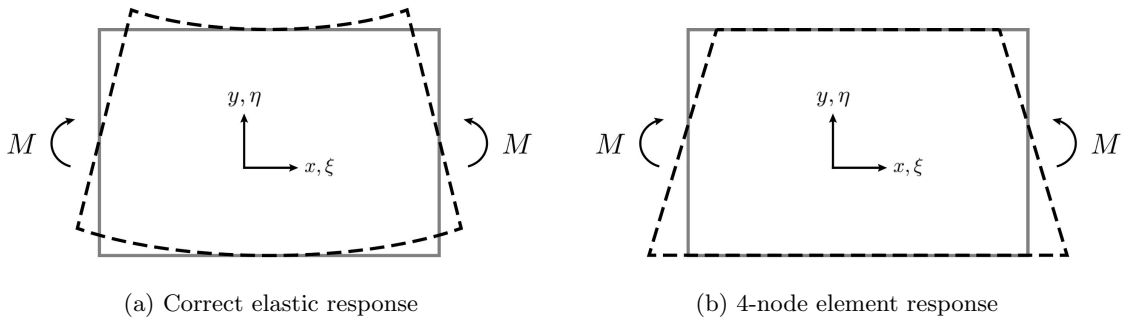
Figure 3.9: Shear locking issue for a 2D quadrilateral element under pure bending M

Volumetric locking is another issue when materials are incompressible. For these types of materials, when the Poisson's ratio ν approaches 0.5, the term $1 - 2\nu$ will approach zero. It becomes a problem when the material tensor D defined in terms of a Lame's constant λ such that the term $1 - 2\nu$ is in the denominator of λ. Once that happens, λ goes to infinity, and convergence does not occur with mesh refinement. Figure 3.10 shows an example of this issue where the displacement is measured on the top right node for two materials with different Poisson's ratio: 0.3 and 0.4999. The *selective reduced integration* method can solve this issue by splitting the material tensor into two components: deviatoric and volumetric tensor. The splitting process can be demonstrated by a simple plane strain

tensor of a linear isotropic elastic material as follows

$$\boldsymbol{D} = \begin{bmatrix} \lambda + 2\mu & \lambda & 0 \\ \lambda & \lambda + 2\mu & 0 \\ 0 & 0 & \mu \end{bmatrix} = \mu \begin{bmatrix} 2 & 0 & 0 \\ 0 & 2 & 0 \\ 0 & 0 & 1 \end{bmatrix} + \lambda \begin{bmatrix} 1 & 1 & 0 \\ 1 & 1 & 0 \\ 0 & 0 & 0 \end{bmatrix} \quad (3.36)$$

$$\boldsymbol{D} = \boldsymbol{D}_{dev} + \boldsymbol{D}_{vol} \quad (3.37)$$

where λ and μ are the usual Lame's constants, and stress is related to strain as $\boldsymbol{\sigma} = \boldsymbol{D}\boldsymbol{\varepsilon}$. The integrals associated with $\boldsymbol{D}_{dev}$ will have full integration while the integrals associated with $\boldsymbol{D}_{vol}$ will have reduced integration, which suggests the name of the method. In some cases, using the selected reduced integration method may cause the element to distort and have an hourglass shape, so an *hourglass stabilization* option can be included.
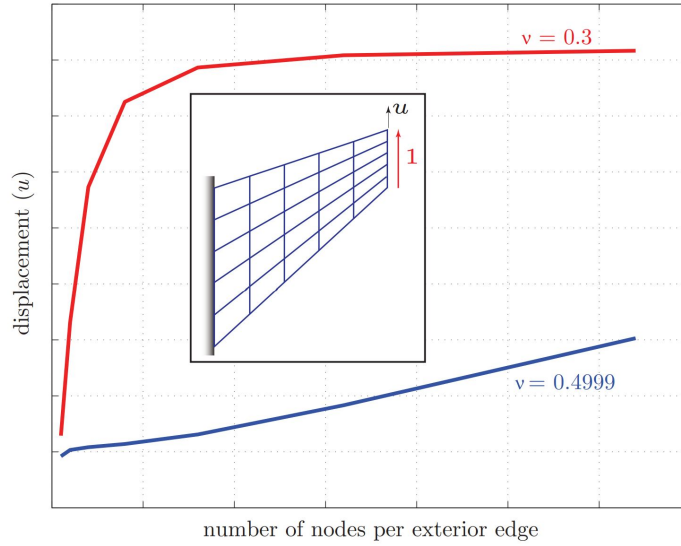
Figure 3.10: Volumetric locking issue[21]

3.2.6 ISOPARAMETRIC MAPPING

Throughout the discussions above, we should notice that the shape functions are conveniently plotted in the coordinate system of (ξ, η) and not in the coordinate system of (x, y) of the structure. The (ξ, η) coordinate system is called the *parent* or *natural* domain that reflects the regular-shaped elements while the (x, y) coordinate system, which reflects

49

the irregular-shaped elements of a structure, is called the *physical* domain. Formulating a problem on the parent domain offers a means for irregular-shaped elements to inherit the well-established completeness and integrability properties of their regular-shaped counterparts.[30] It also greatly simplifies the satisfaction of completeness and continuity conditions that are necessary for convergence.[21]

An isoparametric mapping is a formulation such that the primary unknowns of an element $u^h(\xi)$ and the coordinates of an element $\boldsymbol{x}(\xi)$ are interpolated by the same shape functions. In mathematical form, we have

$$u^h(\xi, \eta) = \sum_{a=1}^{n} N_a(\xi, \eta) d_a^e \tag{3.38}$$

$$\boldsymbol{x}(\xi, \eta) = \sum_{a=1}^{n} N_a(\xi, \eta) \boldsymbol{x}_a^e \tag{3.39}$$

where d_a^e represent the element degrees of freedom, and $\boldsymbol{x}_a^e$ are the vectors with coordinates (x_a^e, y_a^e) pointing from the origin to the positions of each node. The superscript h refers to the association with a mesh or discretization which is parameterized by a characteristic length scale h of an element.[15] Figure 3.11 visualizes the mapping process between the (ξ, η) coordinate system and the (x, y) coordinate system.
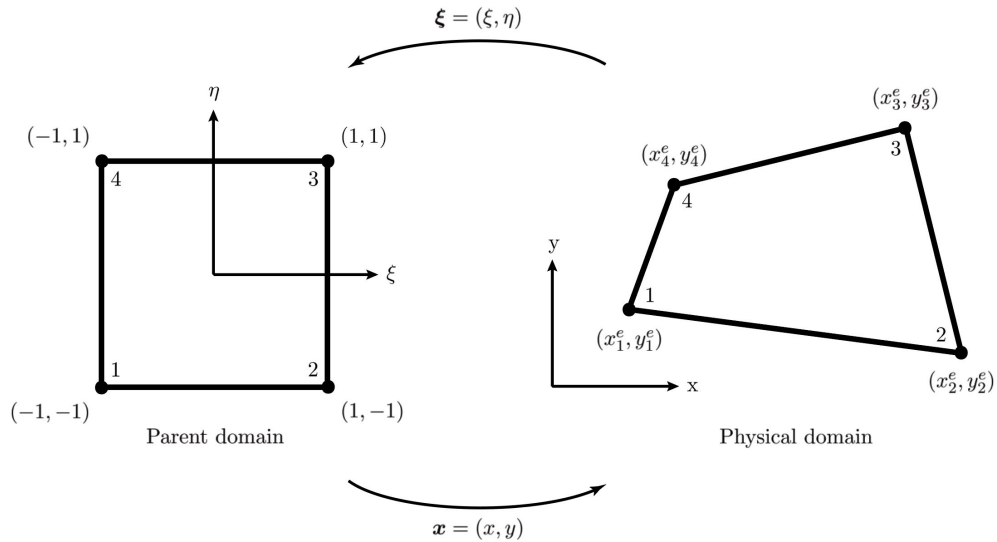
Figure 3.11: Isoparametric mapping for a bilinear quadrilateral element[15]

In the mapping process, we can define the Jacobian matrix as

$$\mathbf{J} = \frac{\partial \boldsymbol{x}}{\partial \boldsymbol{\xi}} \tag{3.40}$$

or in indicial notation: $J_{ij} = \partial x_i / \partial \xi_j$. The determinant of the Jacobian matrix for a 2D transformation, from Equation 3.40, is defined as

$$|\mathbf{J}| = \begin{vmatrix} \frac{\partial x_1}{\partial \xi_1} & \frac{\partial x_1}{\partial \xi_2} \\ \frac{\partial x_2}{\partial \xi_1} & \frac{\partial x_2}{\partial \xi_2} \end{vmatrix} \tag{3.41}$$

$$= \begin{vmatrix} \frac{\partial x}{\partial \xi} & \frac{\partial x}{\partial \eta} \\ \frac{\partial y}{\partial \xi} & \frac{\partial y}{\partial \eta} \end{vmatrix} \tag{3.42}$$

where $\xi_1 \equiv \xi$, $\xi_2 \equiv \eta$, $x_1 \equiv x$, and $x_2 \equiv y$. An infinitesimal area dA in the physical domain can also be transformed to an infinitesimal area $d\xi d\eta$ in the parent domain as follows

$$d\vec{A} = d\vec{x} \times d\vec{y} = \left(\frac{\partial x}{\partial \xi} d\xi \, \hat{\boldsymbol{\imath}} + \frac{\partial y}{\partial \xi} d\xi \, \hat{\boldsymbol{\jmath}} \right) \times \left(\frac{\partial x}{\partial \eta} d\eta \, \hat{\boldsymbol{\imath}} + \frac{\partial y}{\partial \eta} d\eta \, \hat{\boldsymbol{\jmath}} \right) \tag{3.43}$$

$$= \left(\frac{\partial x}{\partial \xi} \frac{\partial y}{\partial \eta} d\xi d\eta - \frac{\partial x}{\partial \eta} \frac{\partial y}{\partial \xi} d\xi d\eta \right) \hat{\boldsymbol{k}} \tag{3.44}$$

$$= |\mathbf{J}| \, d\xi d\eta \, \hat{\boldsymbol{k}} \tag{3.45}$$

or in magnitude form: $dxdy = |\mathbf{J}| \, d\xi d\eta$. This result becomes important in evaluating the integrals appearing in the weak form. The Jacobian determinant, in fact, occurs very often in mathematical contexts, such as the transformation between Cartesian and polar coordinate that $dxdy = r \, drd\theta$.

The strong form in Equation 3.9, which is derived from the FBD, applies to the overall structure with two boundary conditions. Other methods, such as energy-based methods, can also be used to derive the similar differential equation. What makes our discussion so far an FEA process is the application of the formulation over each element that is discretized by a meshing routine. For each element obeying the same set of differential equations, by using shape functions to discretize the solution and then using matrix oper-

ation to solve for primary unknowns (displacement of each node for example), we can then find approximate solution for the discretized domain and other secondary variables. This emphasizes the importance of having two viewpoints: the global and the element viewpoint, which are discussed through the process of isoparametric mapping.

3.2.7 Numerical Integration

Finding the analytical expressions for the integrals in matrices $\mathbf{K}$ and $\mathbf{F}$ is quite challenging, especially with tens of thousands of elements in a structure. An alternative method is the numerical integration. This works particularly well with modern computers since the numerical integration relies on evaluating polynomials at specific points, which makes the process much faster than finding analytical expressions. An appropriate weighting factor is multiplied at each point of evaluation before they are all added together to find the value of integration. An arbitrary integrand $f(x)$ which is smooth and integrable in the physical domain is transformed to the parent domain as

$$\int_a^b f(x)\, dx = \int_{-1}^{1} f\left(\frac{b-a}{2}\xi + \frac{b+a}{2}\right)\left(\frac{b-a}{2}\right) d\xi \tag{3.46}$$

$$= \int_{-1}^{1} g(\xi)\, d\xi \tag{3.47}$$

The transformation is assisted by defining the ratio

$$\frac{x-a}{b-a} = \frac{\xi - (-1)}{1 - (-1)} \tag{3.48}$$

from the limits of each variable: $a \leq x \leq b$ and $-1 \leq \xi \leq 1$. The definite integral in the parent domain is numerically integrated by the formula

$$\int_{-1}^{1} g(\xi)\, d\xi = \sum_{k=1}^{n_p} g(\xi_k) w_k \tag{3.49}$$

where n_p is the number of integration (quadrature) points, ξ_k is the coordinate of the kth integration point, and w_k is the weighting factor at the kth integration point. Similarly, the

numerical integration for a 2D element can be shown as

$$\int_a^b \int_c^d f(x,y)\,dx\,dy = \int_{-1}^1 \int_{-1}^1 f\left(\frac{b-a}{2}\xi + \frac{b+a}{2}, \frac{d-c}{2}\eta + \frac{d+c}{2}\right)|\mathbf{J}|\,d\xi\,d\eta \qquad (3.50)$$

$$= \sum_{k=1}^{n_p}\sum_{l=1}^{n_p} g(\xi_k, \eta_l)w_k w_l \qquad (3.51)$$

where η_l is the coordinate of the lth integration point, w_l is the weighting factor at the lth integration point, and the Jacobian determinant, as a result of changing variables, is

$$|\mathbf{J}| = \left(\frac{b-a}{2}\right)\left(\frac{d-c}{2}\right)$$

which agrees with Equation 3.42.

There are many numerical integration techniques: Trapezoidal rule, Simpson's rule, or Gauss-Legendre quadrature rules. The Trapezoidal rule and Simpson's rule are special cases of the Newton-Cotes quadrature rules. Although these rules are widely used, they are inefficient in the sense that there exist integration rules that are just as accurate but involve fewer integration points.[15] For the Gaussian-Legendre quadrature rules, in order to integrate completely a polynomial order p, the required number of integration points—or sampling points[†]—is rounded to the nearest integer toward infinity following the formula[21]

$$n_p = \frac{p+1}{2} \qquad (3.52)$$

For example, numerically integrating a 4th-order polynomial requires at least 3 integration points for accuracy. Table 3.1 gives a list up to 7 integration points in decimals for one dimension. The derivation for a 3-point Gaussian quadrature formula is shown in Appendix C along with the exact fractional expressions up to 5 integration points. Generally, for multi-dimensional domains, the Gaussian-Legendre quadrature rules can be extended by applying the one-dimensional formulas to each dimension before summing them all up, as shown in Equation 3.51. Figure 3.12 illustrates three integration rules over a 2D quadrilateral parent

---

[†]Some textbooks often call Gauss points as sampling points.

domain: 1 integration point, 2 integration points, and 3 integration points in each dimension. For each dimension, the same quadrature rules highlighted in Table 3.1 can be used.

Table 3.1: Gauss-Legendre quadrature rules

# of points (n_p)	Coordinates (ξ_k)	Weighting factors (w_k)
1	$\xi_1 = 0$	$w_1 = 2$
2	$\xi_1 = -0.5774$	$w_1 = 1$
	$\xi_2 = 0.5774$	$w_2 = 1$
3	$\xi_1 = -0.7746$	$w_1 = 0.5556$
	$\xi_2 = 0$	$w_2 = 0.8889$
	$\xi_3 = 0.7746$	$w_3 = 0.5556$
4	$\xi_1 = -0.8611$	$w_1 = 0.3479$
	$\xi_2 = -0.3400$	$w_2 = 0.6521$
	$\xi_3 = 0.3400$	$w_3 = 0.6521$
	$\xi_4 = 0.8611$	$w_4 = 0.3479$
5	$\xi_1 = -0.9062$	$w_1 = 0.2369$
	$\xi_2 = -0.5385$	$w_2 = 0.4786$
	$\xi_3 = 0$	$w_3 = 0.5689$
	$\xi_4 = 0.5385$	$w_4 = 0.4786$
	$\xi_5 = 0.9062$	$w_5 = 0.2369$
6	$\xi_1 = -0.9325$	$w_1 = 0.1713$
	$\xi_2 = -0.6612$	$w_2 = 0.3608$
	$\xi_3 = -0.2386$	$w_3 = 0.4679$
	$\xi_4 = 0.2386$	$w_4 = 0.4679$
	$\xi_5 = 0.6612$	$w_5 = 0.3608$
	$\xi_6 = 0.9325$	$w_6 = 0.1713$
7	$\xi_1 = -0.9491$	$w_1 = 0.1295$
	$\xi_2 = -0.7415$	$w_2 = 0.2797$
	$\xi_3 = -0.4058$	$w_3 = 0.3818$
	$\xi_4 = 0$	$w_4 = 0.4180$
	$\xi_5 = 0.4058$	$w_5 = 0.3818$
	$\xi_6 = 0.7415$	$w_6 = 0.2797$
	$\xi_7 = 0.9491$	$w_7 = 0.1295$

Once the integrals are numerically evaluated for each element's $\mathbf{K}$ and $\mathbf{F}$, the element stiffness matrix $\mathbf{K}$ and element residual vector $\mathbf{F}$ can be assembled into a global element arrays to solve for the unknowns of interest.

(a) 1 integration point in each direction   (b) 2 integration points in each direction   (c) 3 integration points in each direction
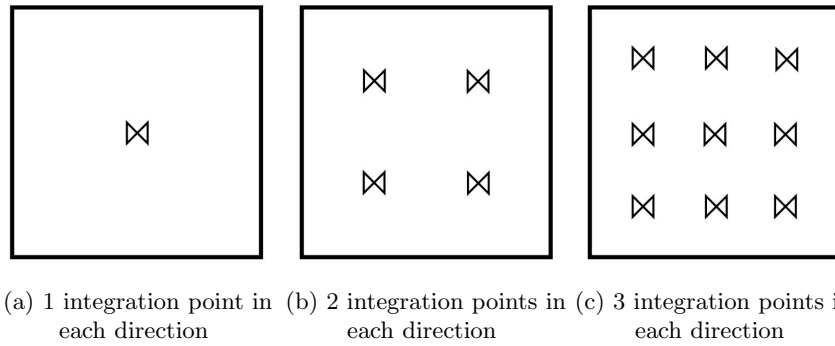
Figure 3.12: Integration points for a 2D quadrilateral parent domain[30]

3.3   VIS HOUSING ENCLOSURE

After the FEA process is discussed, we can review different design iterations for the VIS housing enclosure based on their natural frequencies. Recall that the mass-spring system is designed to have very low natural frequencies for yaw mode as well as vertical mode, which is approximately 1 Hz. An effective VIS, therefore, should have the housing to be as stiff as possible so that its first natural frequency is much higher than the upper limit of the input frequencies, which is expected to be between 1–100 Hz as discussed in Section 2.4. Since the input frequencies to the mass-spring system come from the excitation and resonances of the housing, a large gap between the natural frequencies of the mass-spring system and the housing's 1st natural frequency will allow for a more effective VIS. We can think of an analogy with circuit analysis or signal processing such that we are designing two filters in which the low-pass filter is the mass-spring system while the high-pass filter is the housing enclosure.

Figure 3.13 shows three designs for the housing enclosure: six circular rods, four 90° angles, and a hollow tube with cut-out openings. The 1st case is an extension from the two-stage VIS used at the University of Illinois (Figure 1.12). The 2nd case is the typical design used for CubeSat, and the 3rd case is a novel design using a hollow tube of 0.25$''$ wall thickness.

(a) Case 1: six circular rods   (b) Case 2: four 90° angles   (c) Case 3: a hollow tube

Figure 3.13: Three designs of VIS housing

3.3.1   FEA PROCESS FOR EIGENVALUE PROBLEMS

Similar to the general FEA process for static problems discussed in Section 3.2, the FEA process for dynamic problems starts with the strong form that could be derived through the Newtonian mechanics (forced-based method) or analytical mechanics (energy-based method). For demonstration of the forced-based method, the FBD and KD for an axial beam element are shown in Figure 3.14.
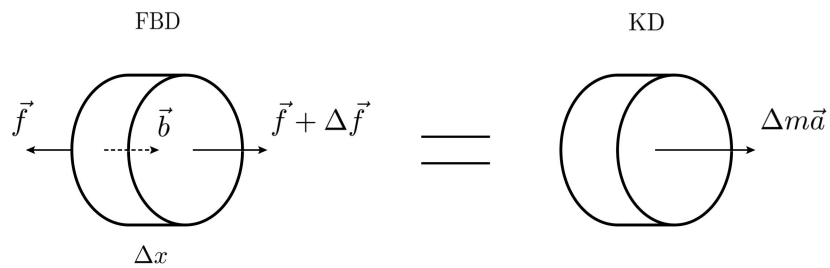
Figure 3.14: FBD and KD for an axial beam element

Summing forces in the horizontal direction gives the following equation

$$\sum \left(\vec{F}_{\text{horizontal}}\right)_{\text{FBD}} = \sum \left(\vec{F}_{\text{horizontal}}\right)_{\text{KD}} \tag{3.53}$$

$$-f + b\Delta x + f + \Delta f = \Delta ma_x \tag{3.54}$$

$$b + \frac{\Delta f}{\Delta x} = \frac{\Delta m}{\Delta x} u_{,tt} \tag{3.55}$$

$$b + \frac{\Delta f}{\Delta x} = \frac{\rho \Delta V}{\Delta x} u_{,tt} \tag{3.56}$$

$$b + AEu_{,xx} = \rho A u_{,tt} \tag{3.57}$$

where $u(x,t)$ is now a function of both displacement x and time t, Δm is the infinitesimal mass of an element, and ρ is the density of the beam. The strong form can be stated that

$$(S) \begin{cases} \text{Find } u(x,t) \text{ such that} \\[2mm] AEu_{,xx} + b = \rho A u_{,tt} \\[2mm] u(0,t) = \overline{u} \\[2mm] AEu_{,x}(L,t) = P \\[2mm] u(x,0) = u_0(x) \\[2mm] u_{,t}(x,0) = \dot{u}_0(x) \end{cases} \tag{3.58}$$

where the last two equations are the initial value conditions (IVC) in contrast to the boundary value conditions (BVC) that we see in the static problems. The weak form, following the same procedure, is defined as

$$(W) \begin{cases} \text{Find } u \in \mathcal{S} \text{ such that for all } w \in \mathcal{V} \\[2mm] AE \int_0^L (u_{,x} w_{,x}) \, dx + \rho A \int_0^L (w u_{,tt}) \, dx = \int_0^L bw \, dx + Pw(L) \end{cases} \tag{3.59}$$

where density ρ is assumed to be constant like the 1-dimensional Young's modulus E. The discretization scheme for u and w are similar to those in Equation 3.19 and Equation 3.22

such that

$$u(x,t) \approx \widehat{u}(x,t) = \sum_{A=1}^{n} N_A(x)d_A(t) + N_0(x)\overline{u} \tag{3.60}$$

$$w(x) = \sum_{A=1}^{n} N_A(x)c_A(t) \tag{3.61}$$

Changing subscript to avoid indicial notation errors and then substituting these equations to the weak form in Equation 3.59 yield

$$\sum_{A=1}^{n} c_A \left[\left(\sum_{B=1}^{n} AE \int_0^L N_{A,x} N_{B,x} \, dx \right) d_B + \left(\sum_{B=1}^{n} \rho A \int_0^L N_A N_B \, dx \right) \ddot{d}_B \right.$$
$$\left. - \left(\int_0^L b N_A \, dx + P N_A(L) - AE \int_0^L \overline{u} N_{0,x} N_{A,x} \, dx \right) \right] = 0 \tag{3.62}$$

Again, if we assign

$$K_{AB} = \sum_{B=1}^{n} AE \int_0^L N_{A,x} N_{B,x} \, dx$$

$$M_{AB} = \sum_{B=1}^{n} \rho A \int_0^L N_A N_B \, dx$$

$$F_A = \int_0^L b N_A \, dx + P N_A(L) - AE \int_0^L \overline{u} N_{0,x} N_{A,x} \, dx$$

then Equation 3.62 can be rewritten as

$$\sum_{A=1}^{n} c_A \left(\sum_{B=1}^{n} K_{AB} \, d_B + \sum_{B=1}^{n} M_{AB} \, \ddot{d}_B - F_A \right) = 0 \tag{3.63}$$

Since c_A's are arbitrary, each set of Equation 3.63 must be identically 0. Therefore, we have

$$\begin{bmatrix} M_{11} & M_{12} & \cdots & M_{1n} \\ M_{21} & M_{22} & \cdots & M_{2n} \\ \vdots & \vdots & & \vdots \\ M_{n1} & M_{n2} & \cdots & M_{nn} \end{bmatrix} \times \begin{Bmatrix} \ddot{d}_1 \\ \ddot{d}_2 \\ \vdots \\ \ddot{d}_n \end{Bmatrix} + \begin{bmatrix} K_{11} & K_{12} & \cdots & K_{1n} \\ K_{21} & K_{22} & \cdots & K_{2n} \\ \vdots & \vdots & & \vdots \\ K_{n1} & K_{n2} & \cdots & K_{nn} \end{bmatrix} \times \begin{Bmatrix} d_1 \\ d_2 \\ \vdots \\ d_n \end{Bmatrix} = \begin{Bmatrix} F_1 \\ F_2 \\ \vdots \\ F_n \end{Bmatrix} \tag{3.64}$$

$$\mathbf{M}\ddot{\mathbf{d}} + \mathbf{K}\mathbf{d} = \mathbf{F} \tag{3.65}$$

where $\mathbf{M}$ is the mass matrix, and $\ddot{\mathbf{d}}$ is the nodal acceleration vector. Equation 3.65 is the generalized formula for multiple-DOF axial vibration systems. Its analogous form for 1D vibration systems is $M\ddot{z} + Kz = F$, which is discussed in Section 2.3. Although axial vibration model is used in the derivation above, Equation 3.65 is also applicable for other types of vibrations, such as transverse vibration. In fact, the matrix form for any damped multiple-DOF systems with external loads can be written as

$$\mathbf{M}\ddot{\mathbf{d}} + \mathbf{C}\dot{\mathbf{d}} + \mathbf{K}\mathbf{d} = \mathbf{F} \tag{3.66}$$

where $\mathbf{C}$ is the viscous damping matrix, and $\dot{\mathbf{d}}$ is the nodal velocity vector.

Considering an undamped system without external forces, we can assume the solution for such system to be $\mathbf{d} = \mathbf{\Phi}(x)e^{i\omega_n t}$ where $\mathbf{\Phi}(x)$ is the nonzero vector containing the magnitude of nodal displacements. Differentiating $\mathbf{d}$ twice and then substituting these into Equation 3.65, we have

$$\mathbf{M}\left[-\mathbf{\Phi}(x)\omega_n^2 e^{i\omega_n t}\right] + \mathbf{K}\left[\mathbf{\Phi}(x)e^{i\omega_n t}\right] = 0 \tag{3.67}$$

$$\left(\mathbf{K} - \omega_n^2\mathbf{M}\right)\mathbf{\Phi}(x)e^{i\omega t} = 0 \tag{3.68}$$

$$\left(\mathbf{K} - \omega_n^2\mathbf{M}\right)\mathbf{\Phi}(x) = 0 \tag{3.69}$$

where $e^{i\omega_n t}$ can be dropped out because it is a non-zero term. Equation 3.69 is a generalized eigenvalue problem that is very familiar to us. Let $\lambda = \omega_n^2$ then the eigenvalues λ are determined to satisfy

$$|\mathbf{K} - \lambda\mathbf{M}| = 0 \tag{3.70}$$

which will allow us to find the corresponding eigenvector $\mathbf{\Phi}(x)$ for each eigenvalue. Directly taking the inverse of $\mathbf{M}$ and multiplying it to the left of $\mathbf{K}$ in Equation 3.69 are quite computationally expensive steps, so other methods, such as the Cholesky decomposition, can be applied to transform the generalized eigenvalue problem into the algebraic eigenvalue problem of the form $(\mathbf{A} - \lambda\mathbf{I})\mathbf{\Phi}$ where $\mathbf{I}$ is the identity matrix. The square root of each

eigenvalue λ yields a natural frequency of the multiple-DOF system while the eigenvectors represent the mode shapes. In fact, a pair of $\{\omega_n, \mathbf{\Phi}(x)\}$ represents the interrelationship between a natural frequency and a mode shape in a multiple-DOF system such that a specific natural frequency will be excited if the corresponding mode shape is applied on the system.

3.3.2 NATURAL FREQUENCIES OF VIS HOUSING

The models in Figure 3.13 are created in SolidWorks, so the native FEA tool for natural frequency study is used to estimate the natural frequencies of the first 4 modes. Table 3.2 lists the material properties used in all FEA models.

Table 3.2: Material properties of Al 6061 used in FEA models

Young's modulus	Poisson's ratio	Density
71 GPa	0.33	2,770 kg/m^3

Table 3.3 shows the natural frequencies of the first 4 modes of each case. In all 3 cases, the models are meshed with tetrahedral elements for quick analyses, and all structures are fixed at the bottom as required by the FEA program. It is interesting to observe that in the first two modes of case 1 and of case 2, the natural frequencies share the same values. Recall that in eigenvalue problems, a repeated eigenvalue can result in two linearly independent eigenvectors when the matrices are nondefective. In multiple-DOF systems, two different mode shapes can excite the same natural frequency, which is typically due to the system's symmetry. For case 2, although it is a common design for CubeSat, the natural frequencies are not as high as expected. It turns out that in most CubeSat structures, the middle section is filled with solid components and masses that increase the overall stiffness of the design, but in our system, the middle section must be hollow to allow for the extension spring setup.

Although the tetrahedral elements are helpful in discretizing complex geometries, they often produce inaccurate results and require an extremely large number of elements for

Table 3.3: SolidWorks's results for the first 4 natural frequencies of 3 cases

	Mode 1 (Hz)	Mode 2 (Hz)	Mode 3 (Hz)	Mode 4 (Hz)
Case 1	74.9	74.9	122.1	345.3
Case 2	49.6	49.6	98.0	313.1
Case 3	478.9	650.6	1,135.4	1,244.8

mesh convergence. However, for the initial analysis in SolidWorks, tetrahedral elements are used for all models because of two reasons. First, we can perform a comparative study for the natural frequencies quickly without wasting too much time on partitioning and setting up interactions or constraints between components. Second, we are only interested in selecting the best candidate that has the highest 1st natural frequency for further detailed study. In addition, although the numerical results for each mode may be incorrect in SolidWorks FEA, by observing the mode shape simulation, we can always judge whether the FEA program breaks the models.

It is apparent that the hollow tube in case 3 is the most promising model. A detailed study in Abaqus is conducted where quadratic shape functions are used to avoid locking issue that is discussed in Section 3.2.5. Shell element family, which is used for the entire model, is an expansion of 2D quadrilateral elements to 3D structures where each node has six DOF (3 translation and 3 rotation components).[40] A constant thickness is assigned to the FEA program to interpolate the shape function throughout the thickness. Figure 3.15 illustrates the first 4 mode shapes of the hollow tube, and Table 3.4 shows the corresponding natural frequency for each mode. From the mode shape simulation, we can expect that once a top and bottom cap are used together with the hollow tube, the overall mode shapes will be more constrained, so the experimental natural frequencies can be higher than what we observe in Abaqus FEA simulation.

Table 3.4: Abaqus's results for the first 4 natural frequencies of case 3

	Mode 1 (Hz)	Mode 2 (Hz)	Mode 3 (Hz)	Mode 4 (Hz)
Case 3	539.34	642.07	752.72	885.76

(a) Mode 1 (b) Mode 2

(c) Mode 3 (d) Mode 4
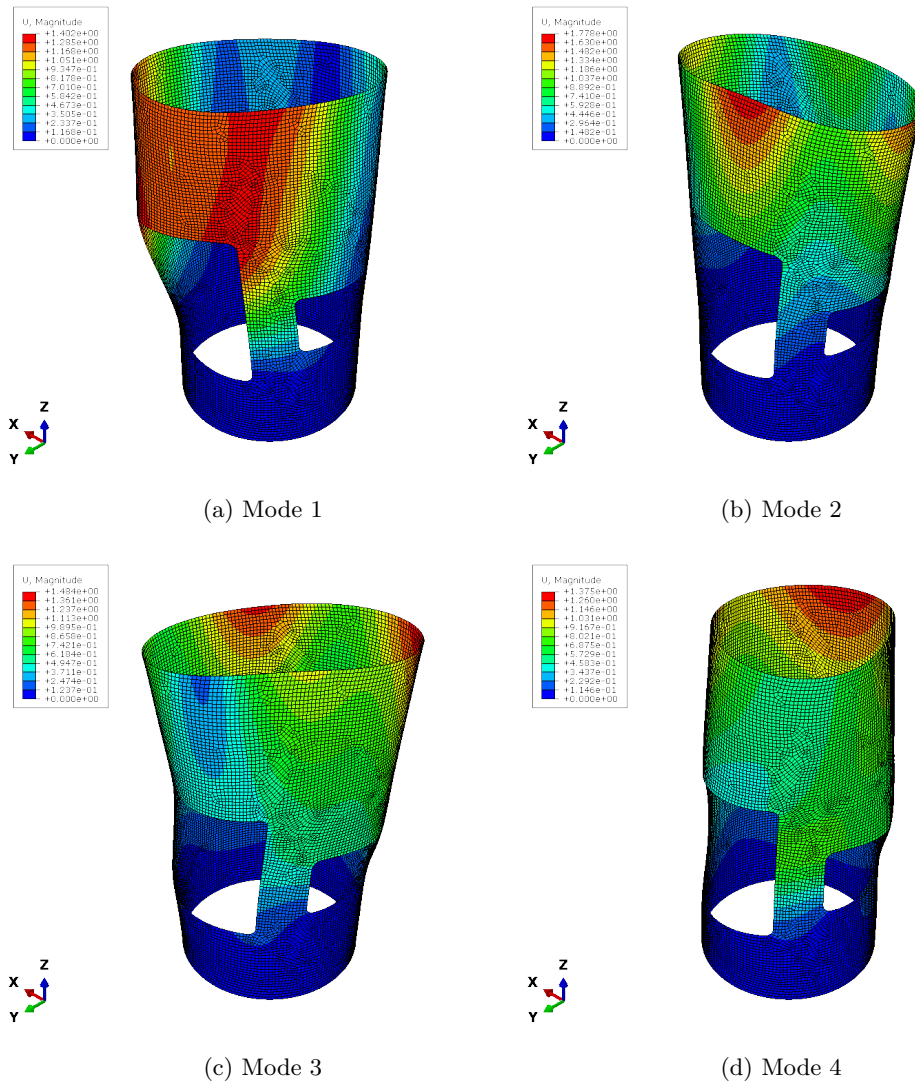
Figure 3.15: First 4 mode shapes simulated in Abaqus

Compared to the shell elements in Abaqus, tetrahedral elements in SolidWorks seem to underestimate the 1st natural frequency while they overestimate the 2nd and higher natural frequencies. Hence, the tetrahedral elements appear to be stiffer than shell elements. This behavior is generally expected for both 2D triangular elements and their 3D counterpart— tetrahedral elements. Figure 3.16 shows the convergence study for the 1st natural frequency using shell elements for the Al housing. The convergence occurs rather quickly, which indicates an advantage of using shell elements for these types of structures.
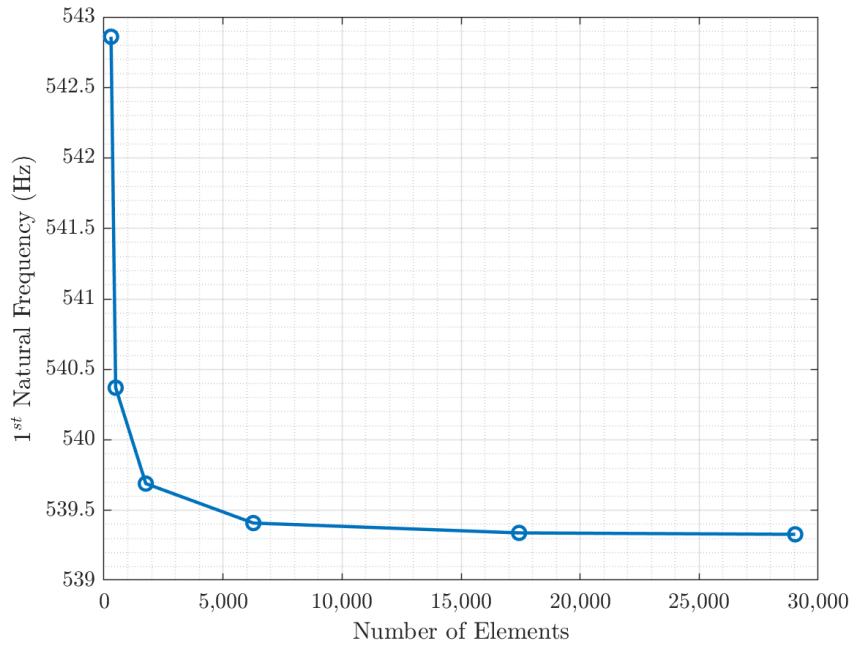
Figure 3.16: Convergence study for the 1ˢᵗ natural frequency of Al housing

3.3.3 Top Cap and Bottom Cap

The top and bottom caps are screwed into the hollow tube using #4-40 vented socket head screws, which are shown in Figure 3.17. In addition to the #4-40 screws, six stud anchors are used on the top cap to attach the extension springs. Since these screws are made of stainless steel, it is much stronger than the Al housing, and failure, if occurs, will be at the root of the internal threads of the housing with the majority of the load is taken by the first thread.[11] Nevertheless, for the VIS under random noise and floor vibrations, the thread failure is less encountered unless the VIS is dropped onto the ground, which is so catastrophic for such sensitive instrument that we should never let this happen. Therefore, the design only focuses on allowing at least 4–5 thread engagement to distribute the load from the weight of the VIS without additional analyses on impact load upon dropping.
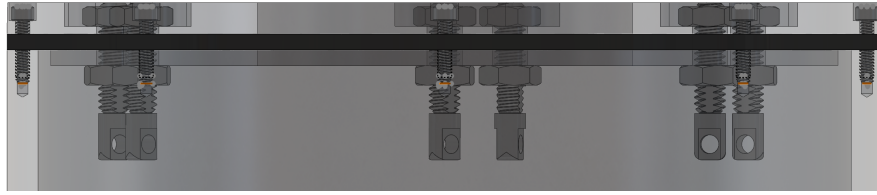
(a) Top cap
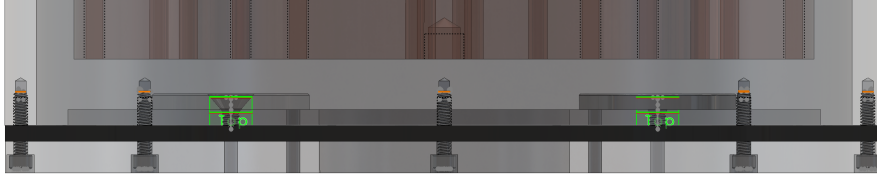
(b) Bottom cap

Figure 3.17: Top cap & bottom cap attached to housing with #4-40 screws

3.4 VITON DAMPER CHARACTERISTICS

As shown in Figure 3.17, the Viton gasket is sandwiched between the top cap and the housing as well as between the housing and the bottom cap. This will allow the Viton to absorb high frequency vibrations since the Al hollow tube has very low damping. There are two different thicknesses that are available on a supplier's website: $1/16''$ and $1/8''$. An overview in terms of material characteristics will be discussed, and, in the following sections, their natural frequencies and transient responses to an impulse load will be investigated. Intuitively, we should expect thicker and heavier Viton gasket to have higher damping capability; however, the natural frequencies are not entirely clear since they are typically proportional to stiffness but inversely proportional to mass.

3.4.1 VISCOELASTIC MATERIALS

Viscoelastic and visco-hyperelastic materials, as the name suggested, possess both the *viscous* and the *elastic* characteristics, which make their behavior inherently non-linear. Because of the viscous part, such materials are time-dependent, which means that they respond to a load gradually over time before reaching an equilibrium. This behavior corresponds to having either or both stress and strain as functions of time. In terms of the

64

elastic characteristic, the main difference between two models is whether the elastic part obeys a linear or a non-linear model. Materials having linear stress-strain responses are categorized as viscoelastic while those having non-linear stress-strain responses are called visco-hyperelastic. In this section, we will discuss the characterization of viscoelastic materials before expanding the concepts to visco-hyperelastic materials.
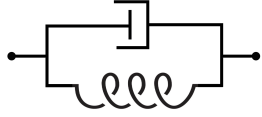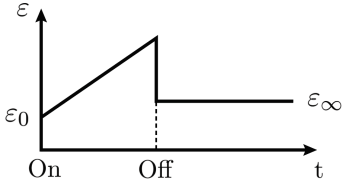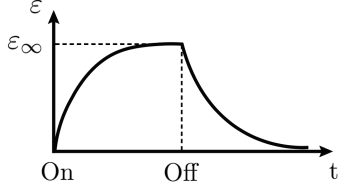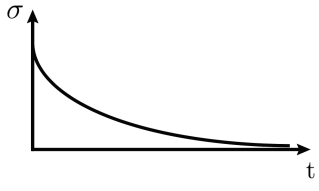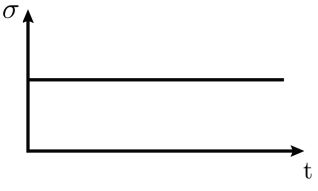
Several classical models are proposed by Maxwell, Kelvin-Voigt, and Zener[1] to characterize viscoelastic materials. In these models, the elastic part is modeled as a spring, and the viscous part is modeled as a damper. Specifically, the Maxwell model features the elastic and viscous parts in series while Kelvin-Voigt model connects them in parallel. The constitutive equations for the stress-strain relationship are

$$\text{Spring:} \quad \sigma_s = E_s \varepsilon_s \tag{3.71}$$

$$\text{Damper:} \quad \sigma_d = c_d \dot{\varepsilon}_d \tag{3.72}$$

where E_s is the Young's modulus of elastic part, and c_d is the viscosity of the dissipative element.[1] The damper's constitutive equation is analogous to the Newton's law of viscosity for fluids: $\tau_{xy} = \mu(\partial u_x / \partial y)$ where u_x is the velocity in the x-direction. Table 3.5 summarizes the models, dynamic equations, as well as the demonstrations of creep and stress relaxation of each model in the time domain. Generally, creep is referred to as the gradual changes of deformation over time under a constant stress. In Table 3.5, creep is observed by switching on and off a constant load. Specifically, when the load is applied, Maxwell model predicts that the strain increases linearly without bound before the load is turned off. Meanwhile, Kelvin-Voigt model predicts that strain increases asymptotically before it gradually decreases once the load is switched off. Stress relaxation, on the other hand, is generally defined as the changes of stress over time when a constant strain is applied.

Table 3.5: Time-domain characteristics of classical viscoelastic models[1]

	Maxwell	Kelvin-Voigt
Model		
Dynamic equations	$\dfrac{c_d}{E_s}\dot{\sigma} + \sigma = c_d\dot{\varepsilon}$	$\sigma = E_s\varepsilon + c_d\dot{\varepsilon}$
Creep		
Stress relaxation		

It is also meaningful to define the viscoelastic responses in the frequency domain. Assume that a viscoelastic material is subjected to a sinusoidal stress such that

$$\sigma = \sigma_0 e^{i\omega t} \tag{3.73}$$

$$\varepsilon = \varepsilon_0 e^{i\omega t} \tag{3.74}$$

where σ_0 is the amplitude of stress, ε_0 is the amplitude of strain, and Euler's formula is used above to assist with the derivation. Using the Maxwell's dynamic equation in Table 3.5, we can show that the amplitude of stress and strain are related by the following form[1]

$$\sigma_0 = \left[\frac{\omega^2\lambda^2}{1 + \omega^2\lambda^2}E_s + i\frac{\omega\lambda}{1 + \omega^2\lambda^2}E_s\right]\varepsilon_0 \tag{3.75}$$

$$\sigma_0 = \left[E'(\omega) + iE'(\omega)\frac{1}{\omega\lambda}\right]\varepsilon_0 \tag{3.76}$$

$$\sigma_0 = \left[E'(\omega) + iE'(\omega)\eta(\omega)\right]\varepsilon_0 \tag{3.77}$$

$$\sigma_0 = \left[E'(\omega) + iE''(\omega)\right]\varepsilon_0 \tag{3.78}$$

66

where $\lambda = c_d/E_s$. The real part $E'(\omega)$ is called *storage modulus*, the imaginary part $E''(\omega)$ is called *loss modulus*, and $\eta(\omega)$ is the *loss factor*. It is obvious that $\eta(\omega)$ is equal to the ratio of loss modulus over the storage modulus. Since the stress-strain relationship is related by a complex form of moduli, the *complex modulus* $E^*(s)$ is often defined as

$$E^*(s) = E^*(i\omega) = E'(\omega) + iE''(\omega) \tag{3.79}$$

where s is the Laplace complex variable: $s = \sigma + i\omega$. Since the stress and strain are assumed to be non-decaying (steady-state) sinusoidal, the σ component vanishes ($\sigma = 0$). Similar steps can be applied to the Kelvin-Voigt model to describe the moduli and loss factor in terms of frequency ω. Table 3.6 shows the frequency-domain characteristics of the Maxwell and Kelvin-Voigt model.

Table 3.6: Frequency-domain characteristics of classical viscoelastic models[1]
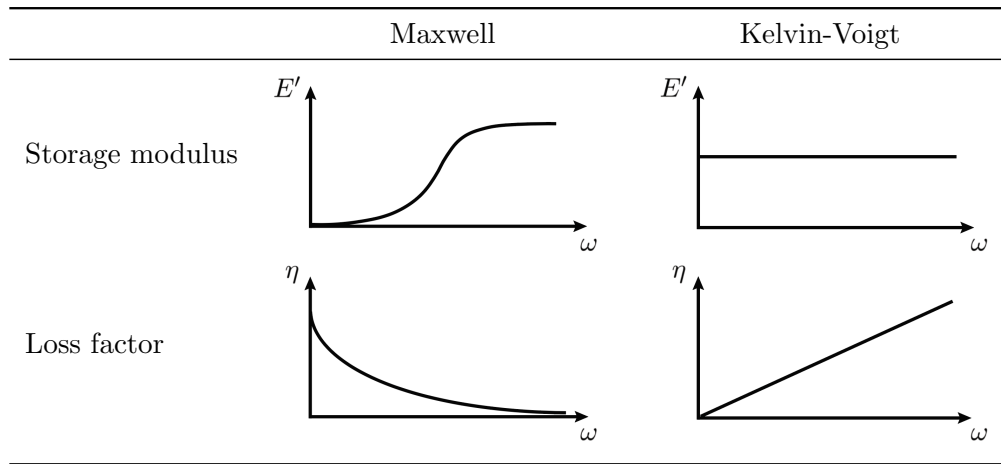
Although these classical theories are helpful in understanding the nature and concepts of viscoelastic materials, some of the responses are unrealistic, and the classical theories have serious limitations in modeling accurately the behavior of viscoelastic materials.[1] Characterization of these viscoelastic materials, in reality, relies heavily on experimental data. Table 3.7 shows several testing methods to measure the dynamic parameters of viscoelastic materials that are necessary for understanding and simulating their behavior. Two popular methods are DMTA[†] and Oberst beam, which are discussed in Appendix E.

[†]DMTA stands for dynamic, mechanical, thermal analyzer.

Method	Freq. (Hz)	Temp. (°C)	Testing mode
DMTA	0.01 to 200	-150 to 300	Shear, tension, bending
Torqued cylinder	50 to 1,500	-40 to 70	Shear
Resonant bar	2.5 to 25,000	-60 to 70	Tension
Oberst beam	10 to 10,000	-60 to 120	Bending of composite beams
Ultrasonic spectroscopy	10^4 to 10^{10}	-35 to 60	Shear

Once the testing data are collected, they are curve-fitted to either time-domain or frequency-domain model to yield key parameters for simulation studies. Multiple advanced models have been introduced, such as the Fractional Derivative (FD), the Golla-Hughes-McTavish (GHM), or the Augmented Temperature Fields model (ATF). The GHM is discussed briefly here, and the other models are left for audience to investigate further. The complex shear modulus $G^*(s)$ in the frequency domain is described as follows

$$G^*(s) = G_0 \left[1 + \sum_{a=1}^{N} \alpha_a \frac{s^2 + 2\zeta_a \omega_a s}{s^2 + 2\zeta_a \omega_a s + \omega_a^2} \right] \tag{3.80}$$

where G_0 is the equilibrium (static) value of shear modulus at $\omega = 0$. The parameters α_a, ζ_a, and ω_a are obtained from the curve fitting process at a given temperature. Function `fmincon` in MATLAB® can be used to assist with the fitting process in which the above parameters are constrained by appropriate conditions. In general, the more mini-oscillators N are used in the GHM model, the more accurate the model will be in comparison to experimental data. For linear, homogeneous, and isotropic viscoelastic materials, the extensional complex modulus $E^*(s)$ can be derived from the complex shear modulus through the relationship

$$G^*(s) = \frac{E^*(s)}{2\big[1 + \nu(s)\big]} \tag{3.81}$$

where $\nu(s)$ is the complex Poisson's ratio. For simplicity, however, a real frequency-independent Possion's ratio $\nu = \nu(s)$ is assumed,[44] which allows the shear and extensional loss factor to be equal: $\eta_E(\omega) = \eta_G(\omega) = \eta(\omega)$.

The Generalized Maxwell Model (GMM) provides an alternative approach to the GHM model such that it enables the modeling process in both time and frequency domains. The GMM method is, in fact, extensively used in many commercial FEA software such as ANSYS.[1] Mathematically, the model is expressed in the time domain by the following Prony series

$$E(t) = E_0 \left[1 + \sum_{a=1}^{N} \alpha_a \exp\left(-\frac{t}{\rho_a} \right) \right] \tag{3.82}$$

where E_0 is the equilibrium modulus at $t = \infty$ when the material is totally relaxed, α_a is the relative modulus, and $\rho_a = \eta_a / E_a$ is the relaxation time constants. The complex modulus in the frequency domain, which can be derived by using Laplace transform, is expressed as

$$E^*(s) = E_0 \left[1 + \sum_{a=1}^{N} \alpha_a \frac{\rho_a s}{\rho_a s + 1} \right] \tag{3.83}$$

Since the GMM model has lower order than the GHM model, it can reduce the complexity in finding the fitting parameters for experimental data. In Abaqus, these parameters can be input directly into the material tab to evaluate the viscous part of the model.

It is also important to mention that the behavior of viscoelastic materials depends primarily on the operating frequency and temperature,[1] and Figure 3.18 demonstrates how these factors affect the storage modulus E' and loss factor η. There are 3 distinct regions for any viscoelastic materials in which the behavior drastically changes: the glassy, the transition, and the rubbery region. For example, for the frequency of 5 Hz in Figure 3.18, the glassy region is approximately below 15 °C, the transition region is between 15–35 °C, and the rubbery region is above 35 °C. These categories apply to both storage modulus and loss factor. Ideally, the viscoelastic materials should be chosen so that they are operated near the peak in loss factor to maximize the damping effect, which is the main purpose in most applications.
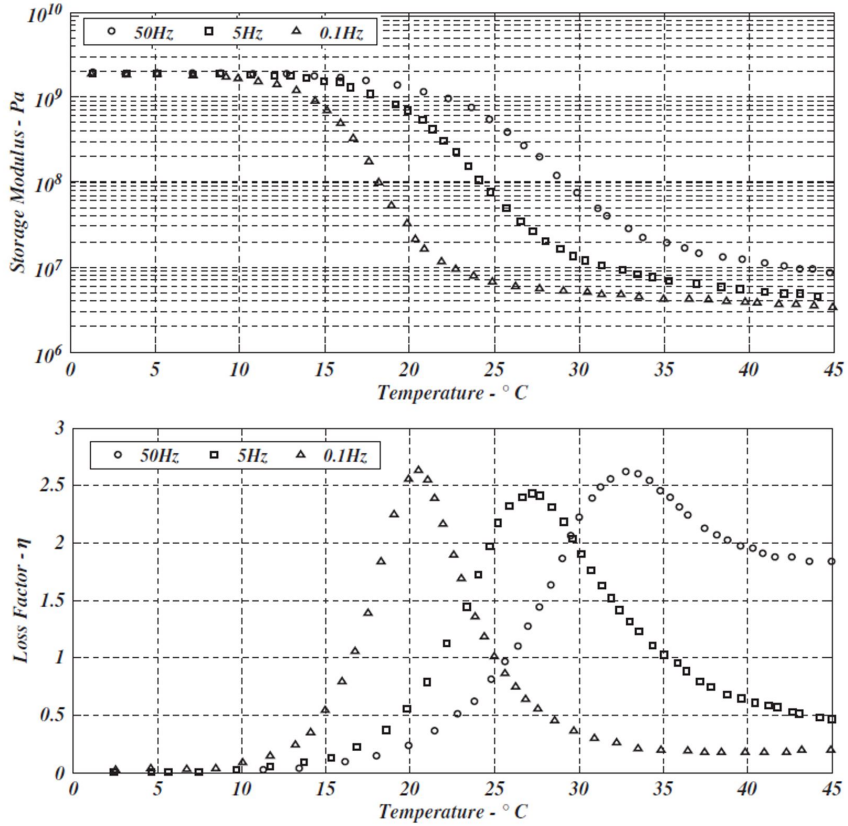
Figure 3.18: Effects of temperature and frequency on storage modulus and loss factor[1]

3.4.2 VISCO-HYPERELASTIC MATERIALS

For visco-hyperelastic materials, instead of a constant Young's modulus reflecting the linear elastic constitutive relationship, the elastic part can be modeled by the hyperelasticity theory where different models such as Neo-Hookean, Mooney-Rivlin, Yeoh, or Ogden model can be used. Viton[†], which is a rubber-like material, is a vacuum compatible elastomer that should be categorized as a visco-hyperelastic material due to its non-linear elastic response. However, the amount of strain also determines whether a hyperelastic model is necessary to model the elastic part. If the strain is below approximately 5–10%,[18] Young's modulus and Poisson's ratio are sufficient while large strain simulations require hyperelastic models to best fit the testing data. For educational purposes, the hyperelastic

---

[†]Fluoroelastomer, or FKM, is the American standard ASTM name of Viton whereas Viton is named after a trademark product of Du Pont's elastomer. They both refer to the same type of material.

70

model, which will be discussed in the next section, is used in this thesis to model Viton gaskets' elasticity.

For the viscous part, time-domain or frequency-domain parameters are defined similarly as discussed in the previous section, and depending on how the materials are tested, they can be input to Abaqus accordingly. However, for the extraction of eigenvalues, the viscous inputs are not required. This can be explained by observing that the natural frequency is proportional to stiffness and inversely proportional to mass. Since mass only depends on material's volume and density, it remains unchanged during steady-state and transient responses at a constant temperature. Stiffness, which depends on part's geometry and material's elasticity, also does not change at a fixed temperature because the equilibrium modulus is defined when the material is static and relaxed. Hence, the viscous part should not affect natural frequency study. However, for transient frequency responses of structures under repeated random impulses, we still need to include the viscous part to ensure an accurate model, so future investigations are necessary to fully characterize this type of materials. If the structures change their shapes or masses while under loading condition, the viscous part needs to be fully incorporated in the analysis.

3.4.3 Mooney-Rivlin Model for Hyperelastic Materials

Each manufacturer has different methods and uses different chemical compositions to make Viton, so samples need to be thoroughly tested before they are used on any applications. During testing, the correct loading type is extremely important to gather correct material parameters to simulate materials' responses for the intended applications. For example, data from uniaxial tension tests are not sufficient to describe the materials' behavior in applications where the materials will be compressed or subjected to biaxial tension. Since the Viton gaskets in our VIS will be sandwiched between Al caps and Al hollow tube, we are interested in studies and data describing Viton samples in uniaxial compression. Performing compression tests on elastomers are relatively difficult due to friction,[18] so an equivalent experimental test for uniaxial compression should be employed. Figure 3.19

shows the equivalence between uniaxial compression and equibiaxial tension. A Viton sheet being subjected to both equibiaxial tensile tractions σ and a hydrostatic stress state $-\sigma$ will experience a resultant uniaxial compression $-\sigma$ as a result of the superposition principle.

Equibiaxial tension   Hydrostatic compression   Uniaxial compression
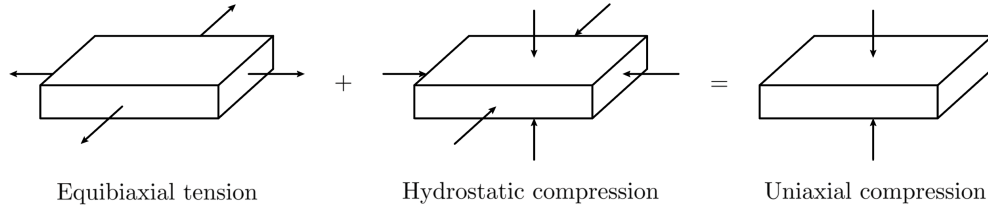
Figure 3.19: Equivalence of equibiaxial tension and uniaxial compression

There are two methods to set up the equibiaxial tension tests: stretching a square sheet in a biaxial testing machine or inflating a circular sample in a pressurized chamber. In a study by Makino *et al.*, the pressurized chamber method is used, and the equivalence of uniaxial compression and equibiaxial tension for Viton is demonstrated. The test sample is clamped at its edge in a pressurized chamber by an annular clamp. A microscope is directed toward the surface of the inflated Viton sheet to measure the coordinates of marked points with respect to inflation pressure. Since Viton exhibits a noticeable viscoelastic behavior as it does not assume an immediate equilibrium position, it is necessary to wait 5–30 minutes depending on the stretch ratios before taking measurements.[25] Once the experimental data are collected, the stretches and stresses are calculated and plotted as shown in Figure 3.20.
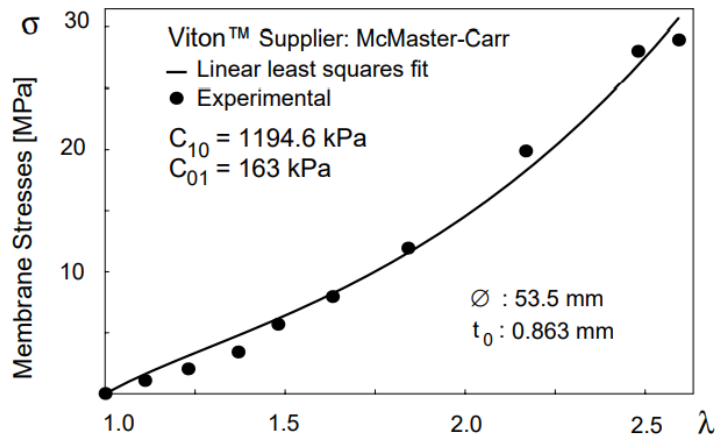
Figure 3.20: Least squares fit of the experimental data for Viton samples[25]

Subsequently, the two-parameter first-order Mooney-Rivlin model is used to generate a response curve to fit over the experimental data. Equation 3.84 shows the strain energy function for the first-order Mooney-Rivlin model such that

$$W = C_{10}(I_1 - 3) + C_{01}(I_2 - 3) \tag{3.84}$$

where I_1 and I_2 are the first and second strain invariants while C_{10} and C_{01} are material constants to be determined. The invariants are defined in terms of principal stretches $\lambda_1, \lambda_2,$ and λ_3 that are in the 1-direction, 2-direction, and 3-direction respectively

$$I_1 = \lambda_1^2 + \lambda_2^2 + \lambda_3^2 \tag{3.85}$$

$$I_2 = \lambda_1^2\lambda_2^2 + \lambda_2^2\lambda_3^2 + \lambda_1^2\lambda_3^2 \tag{3.86}$$

Using the incompressibility property of this material ($\lambda_1\lambda_2\lambda_3 = 1$), we can express the principal true stress components in the 1-direction and 2-direction as

$$\sigma_{11} = \sigma_{22} = 2\left(\lambda^2 - \frac{1}{\lambda^4}\right)\left(\frac{\partial W}{\partial I_1} + \lambda^2\frac{\partial W}{\partial I_2}\right) \tag{3.87}$$

where $\lambda_1 = \lambda_2 = \lambda$ for equibiaxial tension. Equation 3.87 is linear in terms of C_{10} and C_{01}, so a linear least squares fit will appropriately provide a means to solve for these two unknowns. In fact, these coefficients are chosen through the least squares regression process to minimize the error in fitting the experimental data points.[25] In Abaqus, the strain energy function is split into the deviatoric and volumetric components. This separation of strain energy function, however, should not affect the values of C_{10} and C_{01} since the material is assumed to be fully incompressible, which allows the total volume ratio to be 1. Table 3.8 summarizes the material parameters for Viton that will be used in the following simulations. The parameter D_1 is associated with the volume ratio, so its value can be set zero.

Table 3.8: Material properties of Viton used in FEA models

Density	C_{10}	C_{01}	D_1
1,180 kg/m³	1,194.6 kPa	163 kPa	0

In this study, the two-parameter Mooney-Rivlin model is used because it is a common first-order strain energy function. In addition, the stretch ratio in the VIS is expected to be small, which matches the anticipated maximum stretch ratio (less than 1.5) for the application in this study. Although the Viton used in our VIS will be purchased from the same supplier, performing actual tests on purchased Viton from McMaster in the future is important to validate the results.

3.4.4 Natural Frequencies of Viton Gaskets

Since the eigenvectors representing mode shapes are mutually orthogonal, in-plane and out-of-plane modes are not related, and they should be analyzed separately. Specifically, annular structures with rectangular cross-sections have both in-plane and out-of-plane deformations since there is no common degree-of-freedom between the in-plane and out-of-plane motions,[43] so the natural frequencies and mode shapes of Viton gaskets are simulated for both cases.

For the out-of-plane modes, Viton gaskets are modeled with quadratic quadrilateral shell elements, and two thicknesses are assigned accordingly. The through holes for #4-40 vented screws are fixed as the boundary conditions for the simulation process. Figure 3.21 illustrates the mode shapes for the $1/8''$ Viton, and Table 3.9 shows the corresponding natural frequencies. The mode shapes for $1/16''$ are very similar to those of $1/8''$, and they can be found in Appendix D. Overall, thicker Viton gasket has higher natural frequencies for each mode, and with 12 fixed through holes, the lowest natural frequency is above $100\,\mathrm{Hz}$. This suggests that there should be at least 12 screws to be used between the Al caps and Al tube to maintain a uniform contact between the surfaces.

Table 3.9: First 4 out-of-plane natural frequencies of 2 Viton gaskets

Thickness	Mode 1 (Hz)	Mode 2 (Hz)	Mode 3 (Hz)	Mode 4 (Hz)
$1/16''$	73.94	74.17	74.20	74.82
$1/8''$	133.81	134.54	134.54	136.57

(a) Mode 1

(b) Mode 2

(c) Mode 3

(d) Mode 4
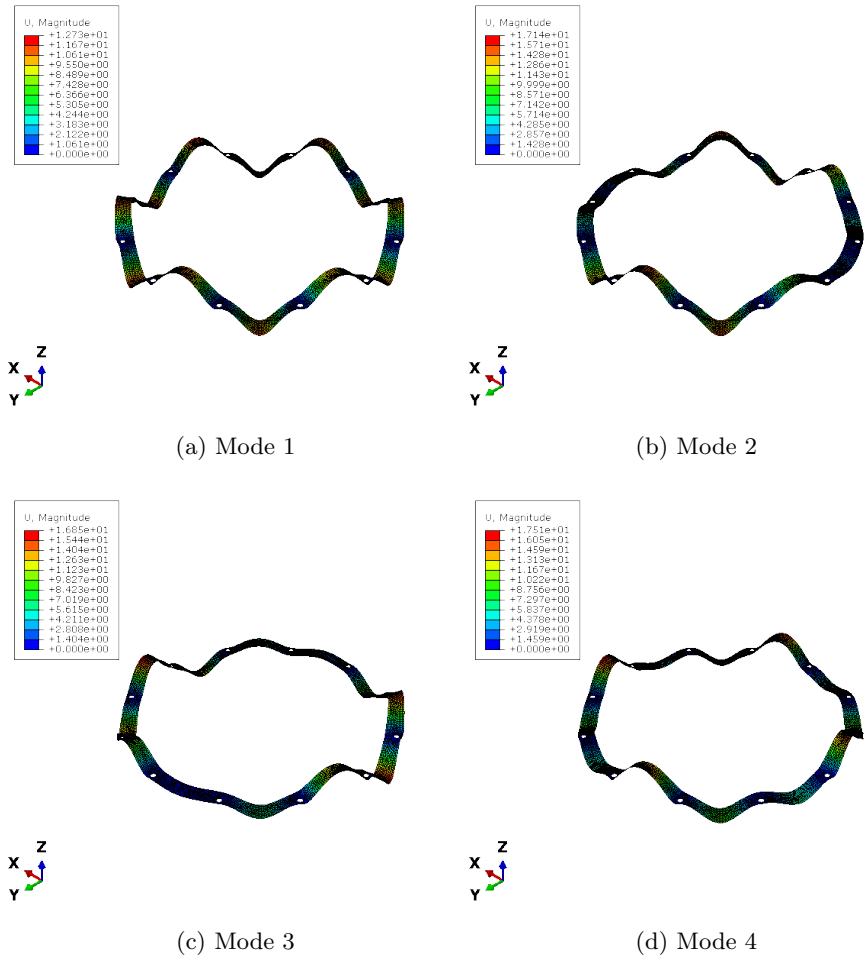
Figure 3.21: First 4 out-of-plane mode shapes of the 1/8-inch Viton gasket

For the in-plane modes, Viton gaskets are modeled as plane strain since each sandwiched gasket is constrained between two surfaces and there is no strain along the thickness direction. Hybrid quadratic elements are used, and the gaskets are also fixed at the through holes. It turns out that the thickness does not affect the eigenvalues for in-plane modes, and both gasket versions have the same natural frequencies. Table 3.10 shows the natural frequencies of both thicknesses, and Figure 3.22 illustrates the corresponding in-plane mode shapes.

Table 3.10: First 4 in-plane natural frequencies of 2 Viton gaskets

Thickness	Mode 1 (Hz)	Mode 2 (Hz)	Mode 3 (Hz)	Mode 4 (Hz)
1/16″ & 1/8″	165.97	175.42	175.42	199.69

(a) Mode 1

(b) Mode 2

(c) Mode 3

(d) Mode 4
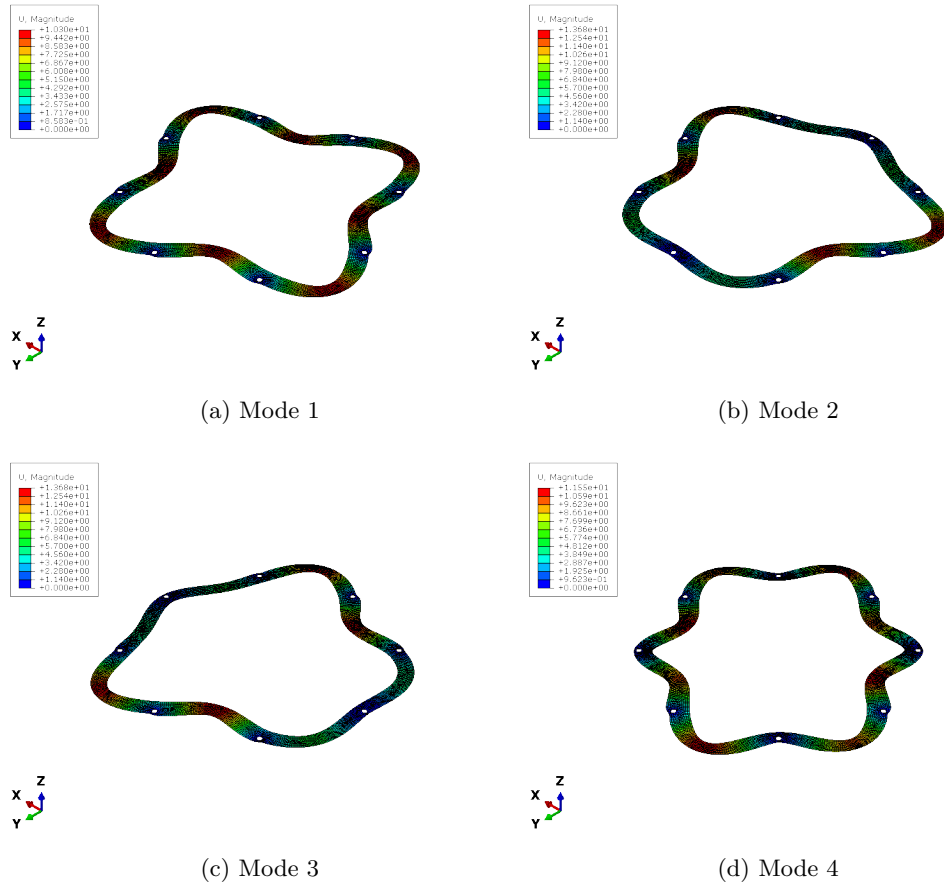
Figure 3.22: First 4 in-plane mode shapes of Viton gaskets

Similar to the shell elements used for Al hollow tube, the quadrilateral shell formulation allows convergence to occur relatively fast for Viton gasket study, which can be seen in Figure 3.23. Both in-plane and out-of-plane modes for Viton gaskets suggest that in the real structure, we should expect some resonances with small amplitude above 100 Hz in the VIS's frequency response due to the Viton gaskets before seeing a larger peak of the VIS's first natural frequency due to the Al hollow tube. The boundary conditions for plane strain study also suggest that we should not overcompress the Viton gaskets; otherwise, the plane strain will become a plane stress study.
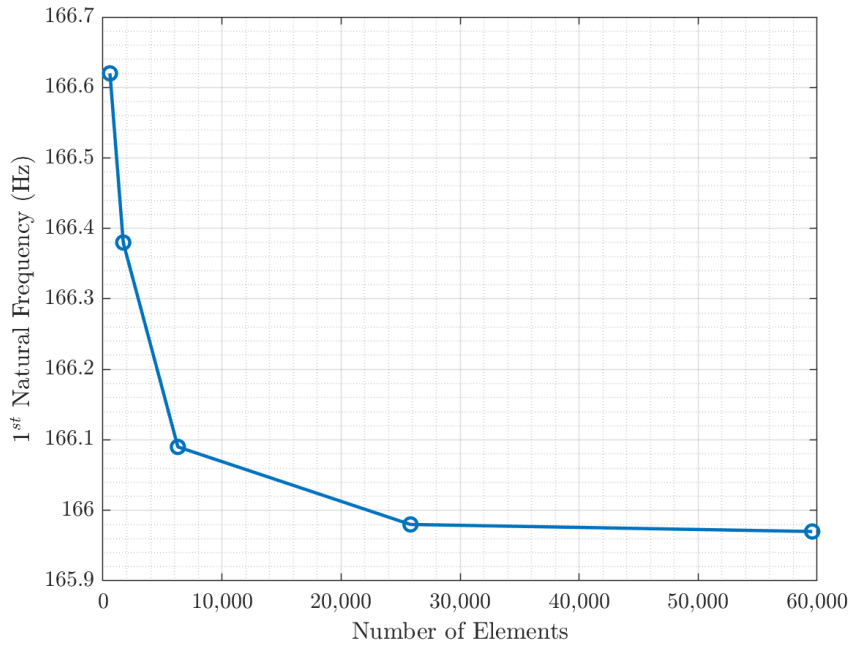
Figure 3.23: Convergence study for the 1$^{\text{st}}$ natural frequency of Viton gasket

3.4.5 TRANSIENT MODAL DYNAMICS OF VITON GASKETS IN ABAQUS

Once the natural frequencies are investigated, we can illustrate the effect of Viton's thickness on damping with the transient modal dynamics in Abaqus. This analysis allows us to construct an impulse force applied to a node and observe the time-domain free response at another neighboring node. Figure 3.24 pictures the applied point load on the Viton gasket in the negative z-direction, and Table 3.11 shows how the load is constructed. The impulse force is defined by an amplitude curve such that the total area under the curve adds up to approximately 1 N. The time period is 0.15 s, and the time increment is set to 0.1 ms, which will result in 1,500 frames per time period.

Table 3.11: Tabular amplitudes for impulse loading

Time (s)	Amplitude (N/s)
0	0
0.001	333
0.003	333
0.004	0

77
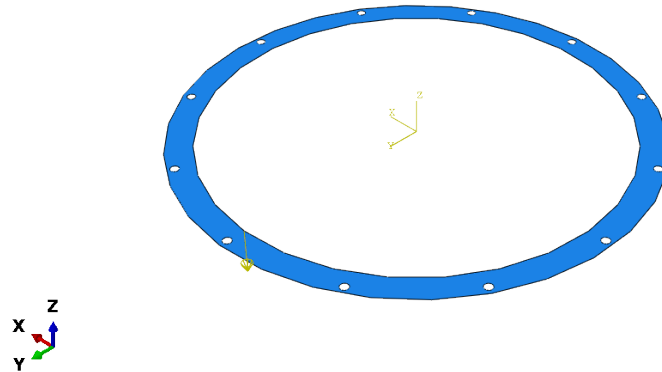
Figure 3.24: Point load applied to Viton gaskets in transient modal dynamics

The structure's response is based on a subset of the number of modes, so this step must be inserted after the eigenvalue extraction step. In this study, the first 10 modes are requested. Figure 3.25 shows the transient responses of two Viton gaskets under the same impulse force recorded at node 215. The excitation in the thicker Viton $(0.125'')$ is attenuated much faster than the thinner one $(0.0625'')$, and the amplitude of the excitation is reduced significantly as well—almost 9 times.
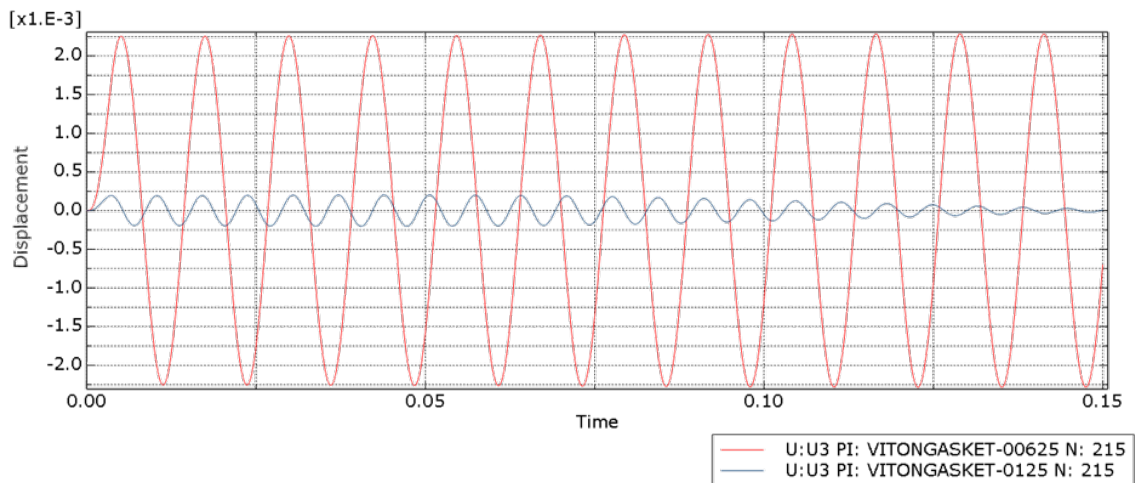
Figure 3.25: Modal dynamic transient responses of 2 Viton gaskets

Usually, to demonstrate the material damping, the Rayleigh damping method is assumed, and user-defined coefficients α and β are used to define the damping coefficient matrix $\mathbf{C}$

78

such that

$$\mathbf{C} = \alpha\mathbf{M} + \beta\mathbf{K} \tag{3.88}$$

where $\mathbf{M}$ is the mass matrix, and $\mathbf{K}$ is the stiffness matrix as usual. For a given mode i, the damping ratio ζ_i can be defined in terms of the natural frequency at each mode as

$$\zeta_i = \frac{\alpha}{2\omega_i} + \frac{\beta\omega_i}{2} \tag{3.89}$$

The parameters α and β can be chosen based on previous experience or to match experimental data. Hence, future studies should revisit this section to propose the guesses for these parameters. In the meantime, this modal dynamic analysis step aims to produce a certain mode shape in the gasket, and the responses shown in Figure 3.25 are to help visualize the responses of two gasket samples to an impulse load. The responses do *not* demonstrate the material damping through the definition of Rayleigh damping as a linear combination of the mass and stiffness matrix. Rather, the illustration gives a sense of how the thickness affects the responses of the gaskets, as we already discuss that the thicker the Viton gasket is, the more damping there will be for the housing tube.

Chapter 4

MAGNETIC DAMPING ANALYSIS

4.1 Background

In Chapter 2, the natural frequencies of the mass-spring system for vertical mode and yaw mode are discussed, and the effectiveness of damping ratio in the vibration isolation region is demonstrated through the displacement transmissibility plot. Ideally, the damping ratio for the mass-spring system should be less than 0.2 for each DOF to provide the right amount of damping in the vibration isolation region; otherwise, the amplitude of the random noises and floor vibrations will be enhanced, and the overall effectiveness of the VIS will be reduced.

Because of the high compatibility of magnetic damping in UHV environment, this will be the main damping mechanism for the mass-spring system. Magnetic damping due to eddy currents generated in the conducting material by permanent magnets, although easy to demonstrate, is notoriously difficult to calculate,[14] analyze, and simulate. In this chapter, the fundamental theories of electromagnetism will be reviewed before we discuss a previous study using magnetic damping on a cantilever beam. The same concepts will be then applied to two vibration modes of the mass-spring system: vertical and yaw modes.

4.2 Electromagnetism Concepts

Just like the mechanical world, the electromagnetism world can be separated into two realms: statics and dynamics. The fundamental equations for electrostatics and magnetostatics, as well as the constitutive relations for linear and isotropic media are summarized in Table 4.1 where $\mathbf{E}$ is the electric field (V/m), $\mathbf{D}$ is electric flux density (C/m^2), $\mathbf{H}$ is the magnetic field intensity (A/m), $\mathbf{B}$ is the magnetic flux density (T or Wb/m^2), and $\mathbf{J}$

is the volume current density (A/m^2). The constant μ represents permeability (H/m), ρ represents electric volume charge density (C/m^3), and ϵ represents permittivity (F/m). All units are standard SI units.

Table 4.1: Fundamental relations for electrostatic and magnetostatic models[5]

	Electrostatic model	Magnetostatic model
Governing equations	$\nabla \times \mathbf{E} = 0$ $\nabla \cdot \mathbf{D} = \rho$	$\nabla \cdot \mathbf{B} = 0$ $\nabla \times \mathbf{H} = \mathbf{J}$
Constitutive relations	$\mathbf{D} = \epsilon \mathbf{E}$	$\mathbf{H} = \dfrac{1}{\mu}\mathbf{B}$

The magnetic flux density $\mathbf{B}$ is an indisputably fundamental quantity[14] and deserves the name magnetic field. Many textbooks, however, refer to both $\mathbf{B}$ and $\mathbf{H}$ as magnetic field, so each of them will be called alongside with its symbol in this thesis to avoid any confusion, even though this sounds extremely repetitive to the audience and especially the author! Hence, $\mathbf{B}$ is often referred to as magnetic flux density in this thesis to allow for variations in the language but not in the physical meaning.

Electrodynamics forms the foundation for the interrelationship between electric fields and magnetic fields: a changing magnetic field will give rise to an electric field, and vice versa. The Maxwell's equations encapsulate these ideas and explain electromagnetic phenomena under time-varying conditions.[5] The Maxwell's equations, Lorentz force law, and the electromagnetism continuity equations explain and predict *all* macroscopic electromagnetic phenomena. One of the Maxwell's equations—Faraday's law—will be explained below since this law is directly applicable to the formation of magnetic damping concepts.

4.2.1 Faraday's Law & Lorentz Force Law

In 1831, Michael Faraday reported a series of experiments, including three that can be summarized below:

- Experiment 1. A loop of wire was moved into and out of a constant magnetic field generated by a fixed magnet. A flow of current was detected in the loop.

- Experiment 2. A magnet was moved into and out of a loop of wire that was held still. A flow of current was also detected in the loop.

- Experiment 3. Both an electromagnet and a loop of wire were fixed. A time-varying magnetic field from the electromagnet caused a flow of current in the loop.

In all three experiments, Faraday discovered that an electric field was induced by a changing magnetic field. This discovery is an experimental postulate that can be expressed by a mathematical equation

$$\mathcal{E} = -\frac{d\Phi}{dt} \tag{4.1}$$

where $\mathcal{E}$ is the electromotive force (V), or emf, and Φ is the flux (Wb) of magnetic field $\mathbf{B}$ crossing a surface. The negative sign indicates that the induced emf will cause a current to flow in the closed loop in such a direction that it opposes the change in the magnetic flux Φ. This is also known as Lenz's law. Equation 4.1 describes all three experiments, and sometimes it is referred to as the Faraday's law. However, describing the Faraday's law this way conceals the underlying reasons for each case. In the first experiment, the emf is induced by the moving conductor, and Lorentz force helps explain how the charges move across the conductor. The emf is magnetic[14] and frequently referred to as the *motional* emf. In the second and the third experiments, the time-varying magnetic field induces the electric field, which in turn explains the emf. This emf is commonly known as the *transformer* emf. Before going into detail about each emf, we will discuss the Lorentz force law first as this is related to the motional emf.

In the present of both electric field $\mathbf{E}$ and magnetic field $\mathbf{B}$, an electric charge q moving with velocity $\boldsymbol{v}$ experiences a force that can be described as

$$\mathbf{F} = q\left(\mathbf{E} + \boldsymbol{v} \times \mathbf{B}\right) \tag{4.2}$$

This is known as the general Lorentz force law, and it can be considered a fundamental postulate of electromagnetic model because it cannot be derived from other postulates.[5] In Faraday's first experiment, when a conductor moves with a velocity $\boldsymbol{v}$ in a static (non-time-varying) magnetic field $\mathbf{B}$, this force will cause the freely movable electrons in the conductor to drift toward one end and leave the other end positively charged.[5] Because the magnetic field $\mathbf{B}$ does not vary, there is no induced electric field $\mathbf{E}$ in the conductor nor the surroundings. Moreover, since there is no applied electric field $\mathbf{E}$, the Lorentz force law can be reduced to

$$\mathbf{F} = q\left(\boldsymbol{v} \times \mathbf{B}\right) \tag{4.3}$$

This force, however, can shift the electric charges and generate an electric field independent from other sources. From the definition for the relationship between force and electric field $\mathbf{F} = q\mathbf{E}$, the electric field generated by Lorentz force can be defined as

$$\mathbf{E} = \boldsymbol{v} \times \mathbf{B} \tag{4.4}$$

Using the definition of emf such that

$$\mathcal{E} = \oint_C \mathbf{E} \cdot dl \tag{4.5}$$

we can describe the motional emf in terms of velocity $\boldsymbol{v}$ and magnetic field $\mathbf{B}$ as

$$\mathcal{E}_{\mathrm{motional}} = \oint_C \left(\boldsymbol{v} \times \mathbf{B}\right) \cdot dl \tag{4.6}$$

In Faraday's second experiment, the magnetic field $\mathbf{B}$ varies because of the moving magnet, and this will induce an electric field $\mathbf{E}$. In the third experiment, time-varying magnetic field caused by the electromagnet also induces an electric field $\mathbf{E}$. The differential form of the well-known Faraday's law stated in the Maxwell's equations allows us to describe

these phenomena as follows

$$\mathbf{\nabla} \times \mathbf{E} = -\frac{\partial \mathbf{B}}{\partial t} \tag{4.7}$$

Taking the surface integral of Equation 4.7 and using Stokes' theorem, we have

$$\int_S (\mathbf{\nabla} \times \mathbf{E}) \cdot ds = \int_S \left(-\frac{\partial \mathbf{B}}{\partial t} \right) \cdot ds \tag{4.8}$$

$$\oint_C \mathbf{E} \cdot dl = -\frac{d}{dt} \int_S \mathbf{B} \cdot ds \tag{4.9}$$

$$\mathcal{E}_{\text{transformer}} = -\frac{d}{dt} \int_S \mathbf{B} \cdot ds \tag{4.10}$$

If we use the definition of magnetic flux Φ such that

$$\Phi = \int_S \mathbf{B} \cdot ds \tag{4.11}$$

we can achieve exactly the experimental postulate shown in Equation 4.1. Therefore, the Faraday's law stated in the Maxwell's equations describes a more specific case of the so-called Faraday's law shown in Equation 4.1 that is somewhat too generic.

To incorporate both the motional emf and transformer emf, we can write the general Faraday's law in the integral form as

$$\oint_C \mathbf{E} \cdot dl = \int_S \left(-\frac{\partial \mathbf{B}}{\partial t} \right) \cdot ds + \oint_C (\boldsymbol{v} \times \mathbf{B}) \cdot dl \tag{4.12}$$

$$\mathcal{E} = \mathcal{E}_{\text{transformer}} + \mathcal{E}_{\text{motional}} \tag{4.13}$$

Equation 4.12 can be used to described a moving circuit or a moving conductor in a time-varying magnetic field. The line integral on the left-hand side of Equation 4.12 is the emf induced in the moving frame, and the division of the induced emf between the transformer and the motional parts depends on the chosen frame of reference.[5]

4.2.2 Eddy Currents & Motional Damping Force

Once the induced emf is generated in the medium, it will produce local currents in the conducting material normal to the magnetic flux Φ. These currents, which are called *eddy currents*, create the magnetic fields to oppose the changes of the magnetic flux permeating the conductor. The strength of eddy currents can be expressed by the microscopic form of Ohm's law similar to other types of currents

$$\mathbf{J} = \sigma \mathbf{E} \tag{4.14}$$

where σ is the electric conductivity of a medium (S/m). Using the local electric field that is generated by the Lorentz force highlighted in Equation 4.4, we can derive the following relationship for eddy current density

$$\mathbf{J} = \sigma \left(\boldsymbol{v} \times \mathbf{B} \right) \tag{4.15}$$

Since the free electric charges reside in a conductor which moves at a uniform speed, Equation 4.15 can be used to describe the overall eddy current density in the moving conductor immersed in a magnetic field $\mathbf{B}$.

On the microscopic level, the electric charges constituting the eddy currents will form a different Lorentz force to oppose the changes in magnetic flux Φ. Using the definition of Lorentz force law once again, we can derive the motional damping force in terms of eddy current density $\mathbf{J}$ as follows

$$\mathbf{F} = q \left(\mathbf{E} + \mathbf{v} \times \mathbf{B} \right) \tag{4.16}$$

$$\frac{d\mathbf{F}}{dV} = \frac{dq}{dV} \left(\mathbf{v} \times \mathbf{B} \right) \tag{4.17}$$

$$\int_V d\mathbf{F} = \int_V \rho \left(\mathbf{v} \times \mathbf{B} \right) dV \tag{4.18}$$

$$\mathbf{F} = \int_V \left(\mathbf{J} \times \mathbf{B} \right) dV \tag{4.19}$$

85

The applied electric field does not exist, so it can be removed. The volume charge density ρ is defined in terms of the infinitesimal electric charge dq over a volume element dV, and another definition of current density $(\mathbf{J} = \rho\mathbf{v})$ is used. This definition allows us to find the motional damping force through the cross product of eddy current density $\mathbf{J}$ and magnetic flux density $\mathbf{B}$ instead of quantifying the charge density ρ. Moreover, it is important to note that Equation 4.18 and Equation 4.19 are equivalent: no motional damping force is generated if the velocity of the conductor $\mathbf{v}$ is parallel to the magnetic flux density $\mathbf{B}$ since their cross product is zero. The cross product of $\mathbf{J} \times \mathbf{B}$ also disappears in that case because there is no eddy current density generated in the conductor; hence, the force must be zero as well. This agrees with the Lorentz force law for a charge particle moving parallel to the magnetic field $\mathbf{B}$ in an absence of electric field $\mathbf{E}$ such that it experiences no force.

4.3   Magnetic Flux Density B

The magnetic flux density $\mathbf{B}$ for a wire carrying a constant current can be readily shown by using the Biot-Savart law. For a permanent magnet, it is not as straightforward, and other theories must be used to find an equivalence for the magnet depending on its type, shape, and strength. There are two main models: the current model and the charge model. In the current model, the magnet is reduced to a distribution of an equivalent current, which is then input into the magnetostatic field equations in Table 4.1 to obtain the magnetic field $\mathbf{B}$.[13] In the charge model, the permanent magnet is reduced to a distribution of equivalent magnetic charge instead. Since the derivation is relatively complicated, only the equations describing the magnetic field $\mathbf{B}$ using the current model are shown below. Specifically, these equations are derived in Craik's textbook.[8] The radial and vertical components at position (r, z) above the top surface of a cylindrical magnet are

$$B_r = \frac{\mu_0 I}{2\pi L} \int_{-L/2}^{L/2} \frac{z - z'}{r\sqrt{(R+r)^2 + (z-z')^2}} \left[-K(k) + E(k)\frac{R^2 + r^2 + (z-z')^2}{(R-r)^2 + (z-z')^2} \right] dz' \quad (4.20)$$

$$B_z = \frac{\mu_0 I}{2\pi L} \int_{-L/2}^{L/2} \frac{1}{r\sqrt{(R+r)^2 + (z-z')^2}} \left[K(k) + E(k)\frac{R^2 - r^2 - (z-z')^2}{(R-r)^2 + (z-z')^2} \right] dz' \quad (4.21)$$

where $\mu_0 = 4\pi \times 10^{-7}$ is the permeability of free space (Tm/A or H/m), I is the equivalent current (A), L is the magnet's length (m), R is the magnet's radius (m), and z' is the variable of integration. For a magnet that is magnetized along the length direction, the equivalent current can be determined as

$$I = M_0 L \tag{4.22}$$

where M_0 is the magnetization of a magnet (A/m). The value of M_0 can be obtained through the remanent flux density† $\mathcal{B}_r$, which is defined as the amount of magnetization left in the ferromagnetic material after the external magnetic field is removed. In the neodymium magnets, the material is NdFeB while common electromagnets use iron cores instead. Table 4.2 shows typical values of remanence $\mathcal{B}_r$ for each magnet grade.

Table 4.2: **Typical values of remanence $\mathcal{B}_r$ for different grades of neodymium magnets**[12]

Magnet grades	$\mathcal{B}_r$ (G)
N35	11,700–12,200
N38	12,200–12,500
N40	12,500–12,800
N42	12,800–13,200
N45	13,200–13,800
N48	13,800–14,200
N50	14,000–14,500
N52	14,300–14,800

The unit for $\mathcal{B}_r$ from most magnet manufacturers is Gauss (G), which can be converted to magnetization M_0 by the following equation

$$M_0 = \frac{\mathcal{B}_r}{\mu_0} \tag{4.23}$$

To simulate the magnetic flux density **B**, the magnet parameters should be obtained from the supplier. Table 4.3 shows the parameters of the chosen magnet for this thesis from McMaster. To perform the integration in Equation 4.20 and Equation 4.21,

†Other names are remanence, remanent magnetization, or residual magnetism.

a MATLAB® function is written, which is attached in Appendix F for reference, and the numerical integration technique highlighted in Table 3.1 can be used. The results are then plotted in 2D and 3D with the shape of the magnet, which are illustrated in Figure 4.1.

Table 4.3: Magnet parameters for a neodymium magnet from McMaster

Grade	Length	Outer dia.	Remanence $\mathcal{B}_r$
N42	$3/16''$	$1''$	$13{,}000\,\text{G}$

(a) 2D

(b) 3D
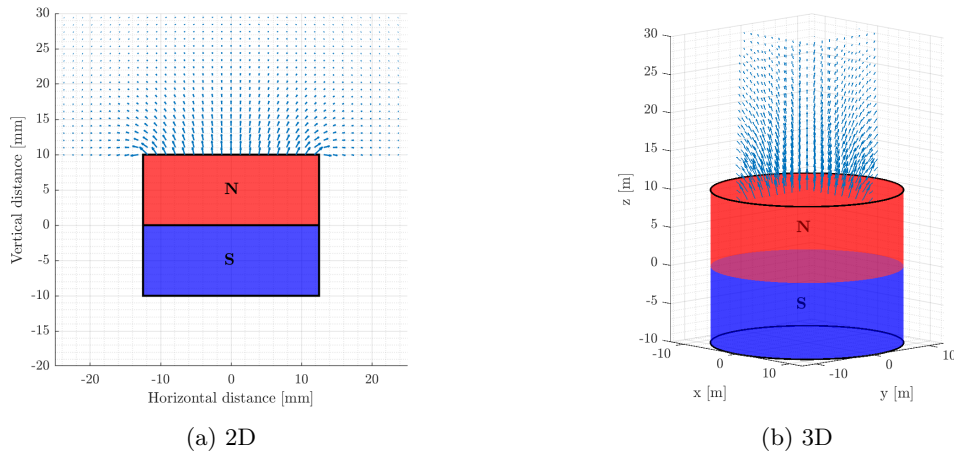
Figure 4.1: Visualization of magnetic flux density B using MATLAB®

In order to verify the magnetic flux density $\mathbf{B}$ produced by the MATLAB® script, we will first compare the results at the magnet's center line from our code with an equation specifically derived to find magnetic field $\mathbf{B}$ at the center line from a different textbook by David Cheng.[5] The equation is shown below:

$$\mathbf{B} = \frac{\mu_0 M_0}{2} \left[\frac{z}{\sqrt{z^2 + b^2}} - \frac{z - L}{\sqrt{(z - L)^2 + b^2}} \right] \hat{\boldsymbol{k}} \tag{4.24}$$

Equation 4.24 is obviously much easier to compute, and the results are overlaid with those from Craik's equations in Figure 4.2. Although the results from each author's equation match nicely, further investigation is necessary. Essentially, Equation 4.24 can only predict the vertical component at the center line. The radial component is not taken into account, and it cannot be verified. This requires us to use another software called FEMM to find the magnetic flux density $\mathbf{B}$.
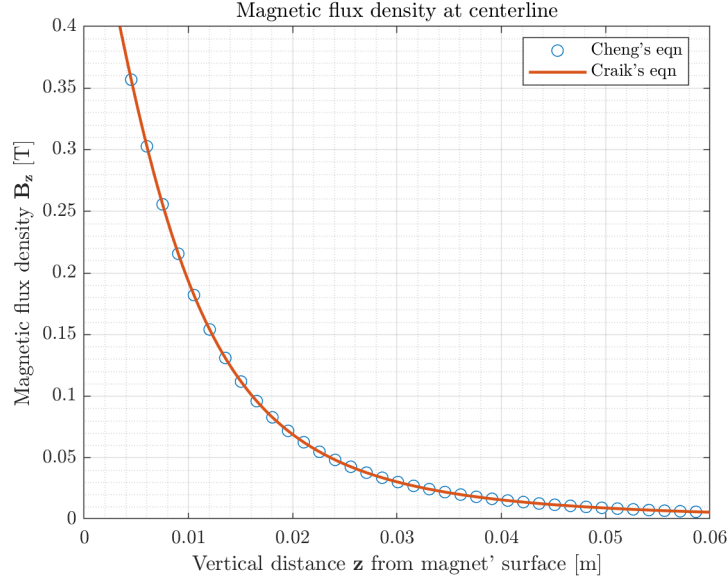
Figure 4.2: Magnetic field along the center line from 2 authors

This FEA software allows us to plot the magnet, input material parameters, discretize the space outside of the magnet, and calculate the magnetic field **B**. Figure 4.3a illustrates the discretization scheme of FEMM using triangular elements. Since the cylindrical magnet is symmetrical about its center axis, only half of the magnet is plotted and simulated. Moreover, the circular boundary region of air around the magnet must be included to make the simulation act as if the analysis is performed on an unbounded domain,[26] even though the finite region of the surrounding space is modeled. Figure 4.3b shows the magnetic flux density **B** results in FEMM. The normal and tangential data are collected at the surface of the magnet and at 15 mm above the surface, which are then overlaid with the respective numerical results of the magnetic flux density **B** from the previous MATLAB® function using Craik's equations. With a numerical integration function written separately, we can attempt several trials for the number of integration points since the formula shown in Equation 3.52 only applies to polynomials and simple fractions. For the complicated ratios of functions in Equation 4.20 and Equation 4.21, although the Gauss-Legendre quadrature rules can still be applied, it turns out that we need more integration points than what is predicted by Equation 3.52. Seven integration points seem to be sufficient and allow the results between each method to match, which can be seen in Figure 4.4.

(a) Spacial discretization using triangular elements

(b) FEA results for magnetic flux density B
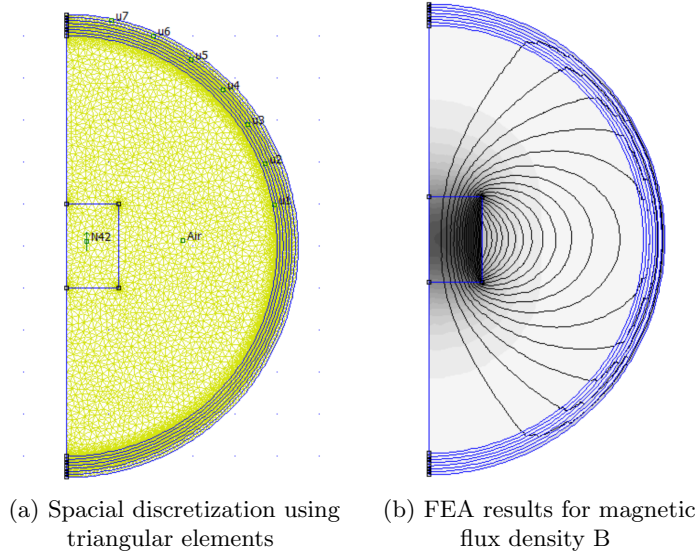
Figure 4.3: Magnetic flux density B generated by FEMM

(a) B_r at surface

(b) B_z at surface

(c) B_r 15mm above surface

(d) B_z 15mm above surface
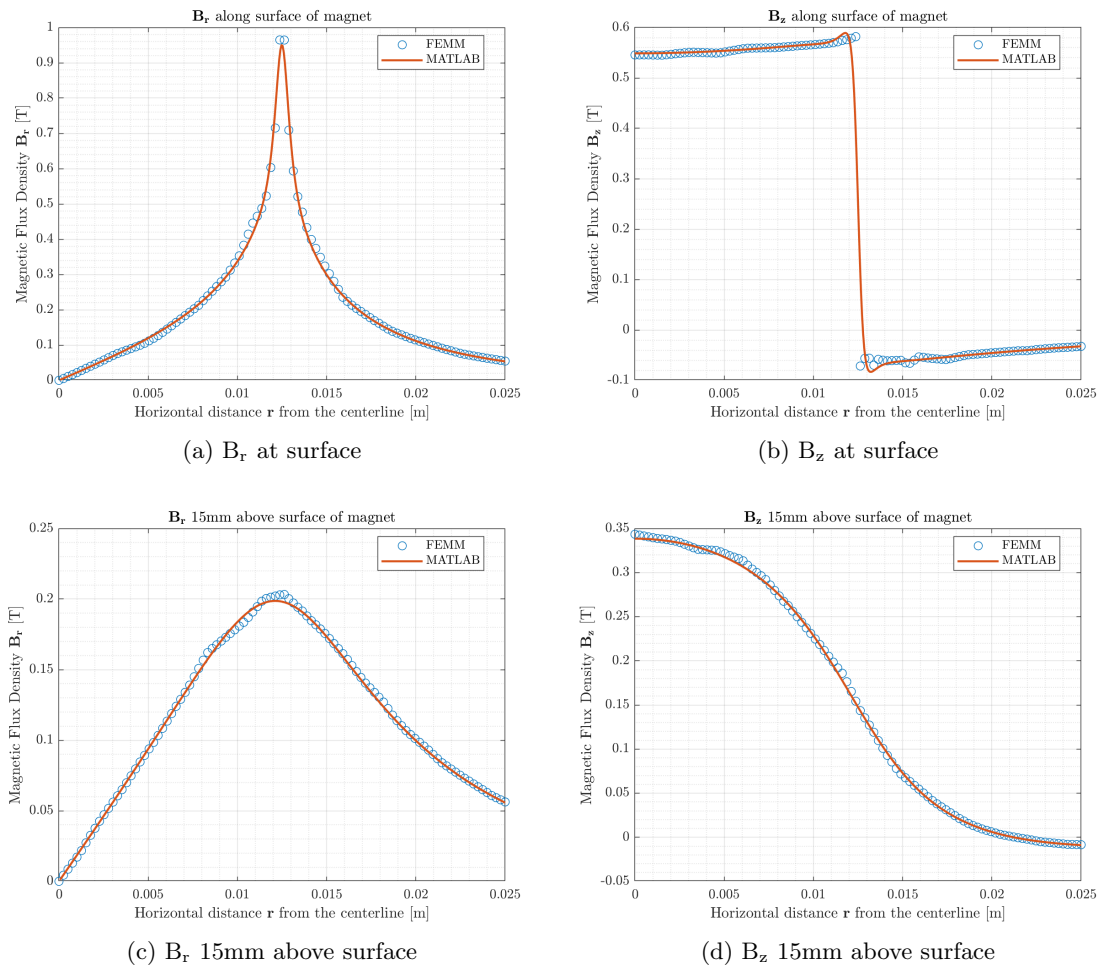
Figure 4.4: Magnetic flux density B comparison between MATLAB® and FEMM

4.4 Magnetic Damping for a Cantilever Beam

Before discussing the analyses for the VIS magnetic damping, we must first assure the audience that the journey we are embarking on up until this point is trustworthy and fruitful. After all, these simulations rely heavily on numerical methods, and without experimental data, they are merely colorful cartoons rather than correct illustrations of physical phenomena that we absolutely intend them to be. Fortunately, several previous studies for magnetic damping are done and proved to be reliable. For this thesis, we will compare the results from a series of experiments by Henry Sodano[41] to our calculations in terms of magnetic damping for a cantilever beam. Figure 4.5 shows the setup of the experiment as well as the measured natural frequencies of the beam, and Table 4.4 lists the magnet parameters used in the study.

Table 4.4: Magnet parameters for Sodano's experiment

Grade	Length	Outer dia.	Remanence $\mathcal{B}_r$
N35	12.7 mm	6.35 mm	12,100 G
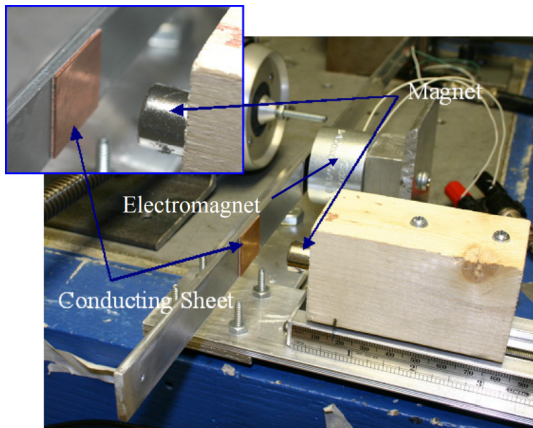
(a) Experiment setup of the Al beam and eddy current damper
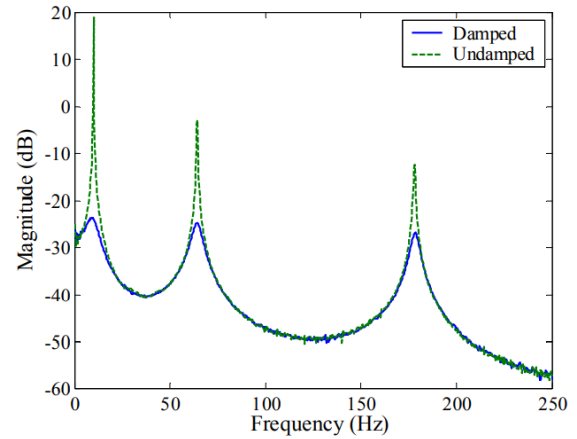
(b) Experimental measurement of damped and undamped frequency responses

Figure 4.5: Experiment setup and measured frequencies in Sodano's experiment[41]

The natural frequencies observed in Figure 4.5b are approximately 9 Hz for the first mode and 65 Hz for the second mode. We use the same MATLAB® functions as above to numerically calculate magnetic flux density $\mathbf{B}$ as well as the damping ratios for each mode.

The results are shown in Figure 4.6 along with the original data and calculations from Sodano's study. As we can observe, the damping ratios with edge effects predicted by our code match very closely with the calculations in Sodano's study for finite conductor with edge effects. In calculating damping ratios, because we are only interested in a quick check against Sodano's study, we assume the effective conducting sheet that the magnet interacts with is all Cu instead of having an Al beam element sandwiched between 2 pieces of Cu as shown in Figure 4.5a. Even though we incorporate the edge effects for finite conductor in our codes, assuming 100% Cu should give us an overestimate of damping ratios since Cu has a higher conductivity than Al and leads to higher eddy current density. However, as we see in Figure 4.6, the margins are very small.
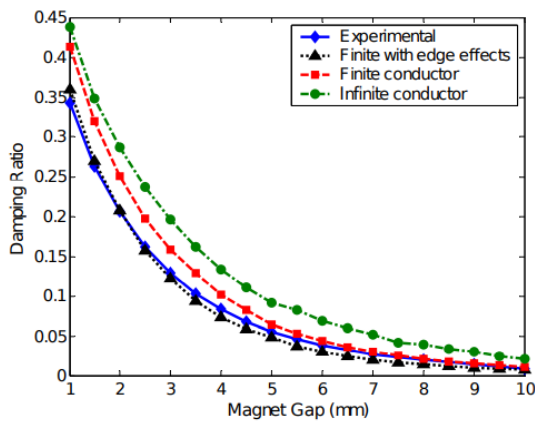
(a) Experimental data & predictions for damping ratio of the 1st mode in Sodano's study[41]
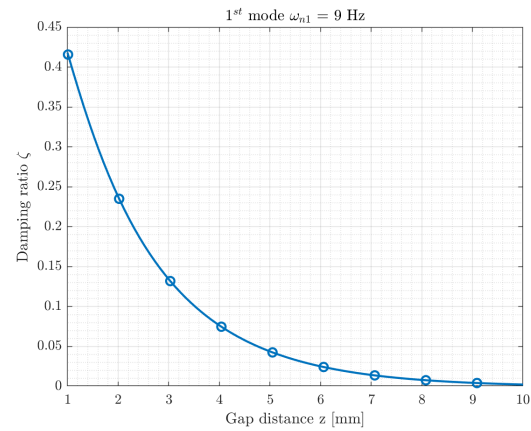
(b) Damping ratio of 1st mode predicted by our MATLAB® scripts
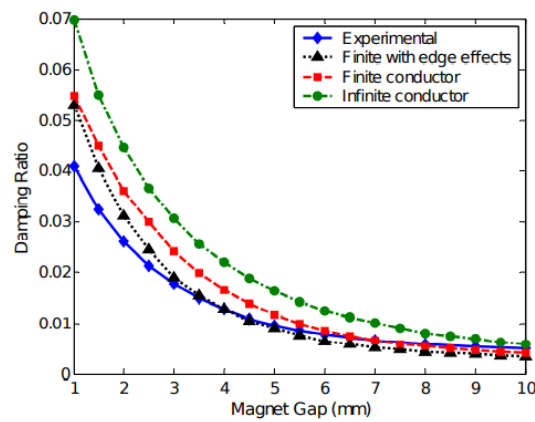
(c) Experimental data & predictions for damping ratio of the 2nd mode in Sodano's study[41]
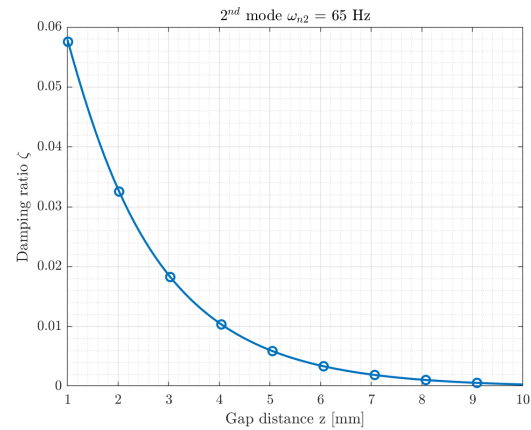
(d) Damping ratio of 2nd mode predicted by our MATLAB® scripts

Figure 4.6: Damping ratio comparison with Sodano's study

4.5 Magnetic Damping for VIS

In the previous section, the eddy current density is calculated but not shown since we are more interested in demonstrating the similarity of results between our code and Sodano's study. In this section, we will explain the mathematical procedures in calculating the eddy current density as well as the damping ratios for the VIS. Figure 4.7 shows the latest configuration with two magnets attached to the bottom cap on either side as an example. Since the magnets are fixed at the bottom of the VIS, only the motional emf is generated in the Cu stage. The derived EOMs for vertical and yaw modes in Chapter 2 will be used to form the complete 2$^{\text{nd}}$-order ODEs, which will be solved in MATLAB® using `ode45` function to find the time domain response for each mode.
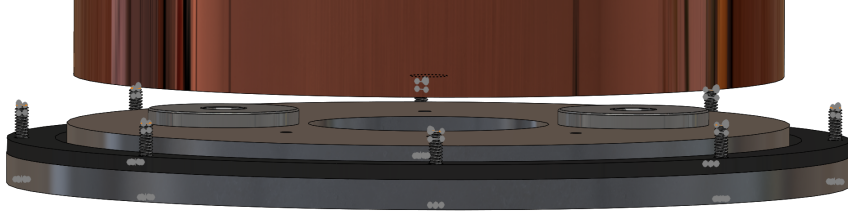
Figure 4.7: Current configuration of magnets under the Cu stage

4.5.1 Eddy Current Density

Because we only consider two modes for the mass-spring system, the velocity vector for an off-center piece of Cu conductor directly above the magnet can be expressed in the cylindrical coordinate system as

$$\boldsymbol{v} = v_\theta \hat{\boldsymbol{\theta}} + v_z \hat{\boldsymbol{z}} \tag{4.25}$$

where v_θ and v_z are the transverse and vertical components respectively, and the coordinate system is fixed at the center of the bottom cap. The magnetic flux density $\mathbf{B}$ with radial

and vertical components can then be written in this coordinate system as

$$\mathbf{B} = B_r \hat{\boldsymbol{r}} + B_z \hat{\boldsymbol{z}} \tag{4.26}$$

Notice that the magnetic flux density $\mathbf{B}$ is already numerically calculated in MATLAB®, so every point in the discretized space above the magnet contains only the values of (B_r, B_z) without the direction for each component in the magnet's coordinate system. This will allow us to conveniently assign the components of $\mathbf{B}$ into a different coordinate system in Equation 4.26 to assist with the calculations of motional damping forces. With this new assignment, the direction of each component of $\mathbf{B}$ will make the motional damping forces to be opposite of the velocity vector. In the following calculations, audience is encouraged to use the right-hand rule to verify the cross products and directions of forces.

We can then calculate the total eddy current density for an *infinite* conducting stage by using Equation 4.15 such that

$$\mathbf{J} = \sigma \begin{vmatrix} \hat{\boldsymbol{r}} & \hat{\boldsymbol{\theta}} & \hat{\boldsymbol{z}} \\ 0 & v_\theta & v_z \\ B_r & 0 & B_z \end{vmatrix} \tag{4.27}$$

$$\mathbf{J} = \sigma \left(B_z v_\theta \hat{\boldsymbol{r}} + B_r v_z \hat{\boldsymbol{\theta}} - B_r v_\theta \hat{\boldsymbol{z}} \right) \tag{4.28}$$

Each mode can be considered separately because they are mutually orthogonal, so the eddy current density for the vertical mode where $v_\theta = 0$ is

$$\mathbf{J}_v = \sigma B_r v_z \hat{\boldsymbol{\theta}} \tag{4.29}$$

The eddy current density for the yaw mode where $v_z = 0$ is

$$\mathbf{J}_y = \sigma B_z v_\theta \hat{\boldsymbol{r}} - \sigma B_r v_\theta \hat{\boldsymbol{z}} \tag{4.30}$$

94

Since the eddy current density for the yaw mode contains both $\hat{r}$ and $\hat{z}$ components, the magnitude of $\mathbf{J}_y$ is treated as the magnitude of a vector: square root of the sum of each component squared.

In order to quantify the numerical values of eddy current density, we need to estimate the velocity value for each mode. If we assume the amplitude of the vertical mode is 1 mm per cycle and the natural frequency for the vertical mode is 1.38 Hz as shown at the end of Chapter 2, we can estimate the vertical velocity as

$$v_z = \left(\frac{1.38 \, \text{cycles}}{\text{s}} \right) \times \left(\frac{1 \, \text{mm}}{\text{cycle}} \right) \tag{4.31}$$

$$v_z = 1.38 \, \text{mm/s} \tag{4.32}$$

For the yaw mode, we also must maintain the standard SI unit for the eddy current density to be A/m^2. If the amplitude of rotation is 1 mm per cycle and the natural frequency for yaw mode is 0.48 Hz that is shown at the end of Chapter 2, we can estimate the transverse velocity for the yaw mode as

$$v_\theta = \left(\frac{0.48 \, \text{cycles}}{\text{s}} \right) \times \left(\frac{1 \, \text{mm}}{\text{cycle}} \right) \tag{4.33}$$

$$v_\theta = 0.48 \, \text{mm/s} \tag{4.34}$$

The infinite eddy current density model neglects the edge effects, so it is only accurate for an infinite large conducting stage above a magnet. However, since the eddy current is required to be zero at the edges so that the damping force is not overestimated,[41] we need to calculate the *finite* eddy current density using the image method. This technique consists of two steps: calculating the regular eddy current density as before and then generating a mirror, or imaginary, image of eddy current density about the conductor's edge. The difference between the infinite and imaginary components ensures zero eddy current density at the boundaries of the conductor. The finite eddy current density for vertical

mode $\mathbf{J}_v^{\text{fit}}$ can be expressed as

$$\mathbf{J}_v^{\text{fit}} = \mathbf{J}_v^{\text{inf}} - \mathbf{J}_v^{\text{img}} \tag{4.35}$$

$$\mathbf{J}_v^{\text{fit}} = \sigma v_z \big[B_r(r,z) - B_r(2r_{\text{out}} - r, z) \big] \hat{\boldsymbol{\theta}} \tag{4.36}$$

where r_{out} is the outer radius of the effective conducting area. Similarly, the finite eddy current density for yaw mode $\mathbf{J}_y^{\text{fit}}$ can be calculated as

$$\mathbf{J}_y^{\text{fit}} = \mathbf{J}_y^{\text{inf}} - \mathbf{J}_y^{\text{img}} \tag{4.37}$$

$$\begin{aligned} \mathbf{J}_y^{\text{fit}} = \sigma v_\theta \big[B_z(r,z)\hat{\boldsymbol{r}} - B_r(r,z)\hat{\boldsymbol{z}} \big] \\ - \sigma v_\theta \big[B_z(2r_{\text{out}} - r, z)\hat{\boldsymbol{r}} - B_r(2r_{\text{out}} - r, z)\hat{\boldsymbol{z}} \big] \end{aligned} \tag{4.38}$$

Figure 4.8 pictures the regular, imaginary, and finite eddy current density for each mode to illustrate the concept of image method. The calculation of eddy current density becomes unstable as the radius of magnet approaching the radius of the conductor, so we recommend that the projected radius of the conductor is twice as large as the radius of the magnet. Appendix G details the MATLAB® code that is used to calculate and display the eddy current density.

(a) Vertical mode   (b) Yaw mode
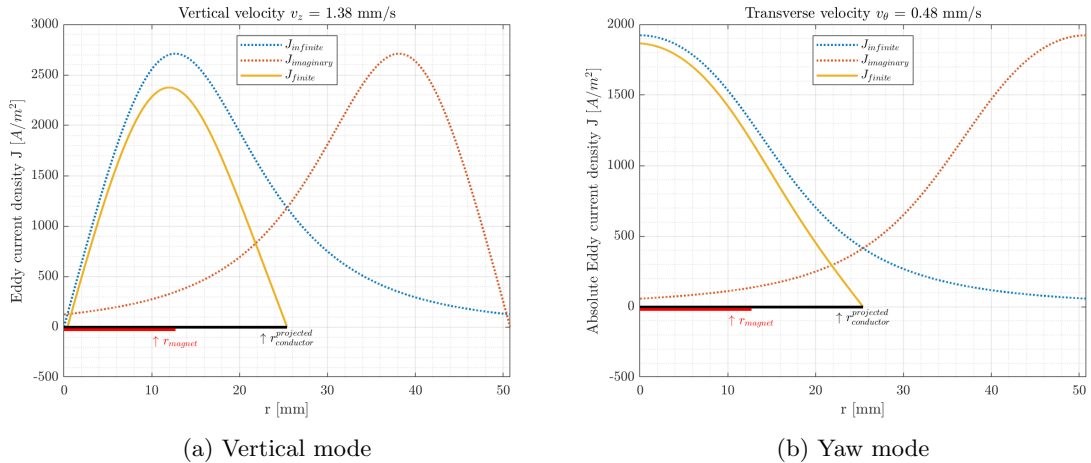
Figure 4.8: Visualization of eddy current density

As we have discussed, the transformer emf is absent since the magnets are fixed and the magnetic flux density **B** does not change with time. Applying Equation 4.19, we can find the form of motional damping force for the vertical mode as

$$\mathbf{F}_v = \int_V (\mathbf{J}_v \times \mathbf{B})\, dV \tag{4.39}$$

$$\mathbf{F}_v = \int_V \left[\left(\sigma v_z B_r \hat{\boldsymbol{\theta}} \right) \times \left(B_r \hat{\boldsymbol{r}} + B_z \hat{\boldsymbol{z}} \right) \right] dV \tag{4.40}$$

It appears that the cross product should be carried out normally. However, it is important to realize that the eddy current density for vertical mode $\mathbf{J}_v$ only exists because of the vertical velocity v_z and the radial component B_r of magnetic flux density **B**. The vertical component B_z does not contribute to the generation of the eddy current density $\mathbf{J}_v$. This is a crucial physical concept. In addition, from Equation 4.18, it can be observed that the magnetic flux density component B_z does not contribute to the damping force[41] because it is parallel to the vertical velocity v_z of the Cu conducting stage. Removing the B_z component and assigning δ as the thickness of the Cu stage, we can calculate the motional damping force $\mathbf{F}_v$ for the vertical mode as

$$\mathbf{F}_v = \int_V \left[\left(\sigma v_z B_r \hat{\boldsymbol{\theta}} \right) \times \left(B_r \hat{\boldsymbol{r}} \right) \right] dV \tag{4.41}$$

$$\mathbf{F}_v = - \int_V \sigma v_z B_r^2 \, dV \, \hat{\boldsymbol{z}} \tag{4.42}$$

$$\mathbf{F}_v = -\sigma v_z \delta \int_0^{2\pi} \int_{r_{\mathrm{in}}}^{r_{\mathrm{out}}} B_r^2 \, r \, dr \, d\theta \, \hat{\boldsymbol{z}} \tag{4.43}$$

$$\mathbf{F}_v = -\sigma v_z \delta 2\pi \int_{r_{\mathrm{in}}}^{r_{\mathrm{out}}} r B_r^2 \, dr \, \hat{\boldsymbol{z}} \tag{4.44}$$

where r_{in} and r_{out} are the inner and outer radius of the effective conducting area respectively. For a non-annular shaped conductor, r_{in} is zero. The motional damping force is proportional to the vertical velocity v_z, so the magnetic damping can be categorized as a form of viscous damping. The negative sign indicates that this damping force opposes the motion of the stage. Using the definition of viscous damping, we can isolate the motional

damping coefficient term as follows

$$C_v = \frac{|\mathbf{F}_v|}{v_z} \tag{4.45}$$

$$C_v = \sigma 2\pi\delta \int_{r_{\text{in}}}^{r_{\text{out}}} rB_r^2 \, dr \tag{4.46}$$

A MATLAB® function is written to calculate C_v, which is shown in Appendix H. The results for motional damping coefficient are output in a column array where each value of C_v corresponds to a specific height of the Cu stage from the magnet's surface. These values of C_v can then be used to calculate the damping ratio ζ_v as

$$\zeta_v = \frac{C_v}{C_v^{\text{crit}}} \tag{4.47}$$

where C_v^{crit} is the critical damping for vertical mode, which is defined similarly to that in Chapter 2: $C_v^{\text{crit}} = 2\sqrt{MK_v} = 2M\omega_{n,v}$. With the stage's mass of $3.95\,\text{kg}$ and the vertical natural frequency estimate of $1.38\,\text{Hz}$, we can calculate the critical damping for the vertical mode as $C_v^{\text{crit}} = 68.499\,\text{kg/s}$. Figure 4.9a illustrates the relationship between the damping ratio and the gap distance between the magnet's surface and the Cu conductor. Since one magnet does not seem to provide sufficient damping, damping by multiple magnets are simulated by multiplying the damping ratio ζ_v with the corresponding number of magnets as we assume there is a linear relationship between the number of magnets and the amount of damping.

Similarly, the motional damping force for the yaw mode can be shown by taking the cross product between the eddy current density for yaw mode $\mathbf{J}_y$ and the magnetic flux density $\mathbf{B}$

$$\mathbf{F}_y = \int_V (\mathbf{J}_y \times \mathbf{B}) \, dV \tag{4.48}$$

$$\mathbf{F}_y = \int_V \left[\left(\sigma B_z v_\theta \hat{\boldsymbol{r}} - \sigma B_r v_\theta \hat{\boldsymbol{z}} \right) \times \left(B_r \hat{\boldsymbol{r}} + B_z \hat{\boldsymbol{z}} \right) \right] dV \tag{4.49}$$

$$\mathbf{F}_y = -\int_V \sigma v_\theta \left(B_z^2 + B_r^2 \right) dV \, \hat{\boldsymbol{\theta}} \tag{4.50}$$

Figure 4.9: Damping ratios for multiple magnet configurations

Since both components of magnetic flux density $\mathbf{B}$ contribute to the eddy current density $\mathbf{J}_y$, the cross product is carried normally. With δ being the thickness of the Cu stage as before, we can calculate the motional damping force $\mathbf{F}_y$ for the yaw mode as

$$\mathbf{F}_y = -\sigma v_\theta \delta \int_0^{2\pi} \int_{r_{\text{in}}}^{r_{\text{out}}} \left(B_z^2 + B_r^2 \right) r \, dr \, d\theta \, \hat{\boldsymbol{\theta}} \tag{4.51}$$

$$\mathbf{F}_y = -\sigma v_\theta \delta 2\pi \int_{r_{\text{in}}}^{r_{\text{out}}} r \left(B_z^2 + B_r^2 \right) dr \, \hat{\boldsymbol{\theta}} \tag{4.52}$$

Since the motional damping force is proportional to the transverse velocity v_θ, the magnetic damping for yaw mode is also a type of viscous damping, and its damping coefficient can be defined as

$$C_y = \frac{|\mathbf{F}_y|}{v_\theta} \tag{4.53}$$

$$C_y = \sigma \delta 2\pi \int_{r_{\text{in}}}^{r_{\text{out}}} r \left(B_z^2 + B_r^2 \right) dr \tag{4.54}$$

The same MATLAB® function in Appendix H is used to calculate this damping coefficient. The output is also an array with each element being the damping coefficient for yaw mode at each discretized height above the magnet's surface. These values of C_y can then be used

to calculate the damping ratio ζ_y by the relationship
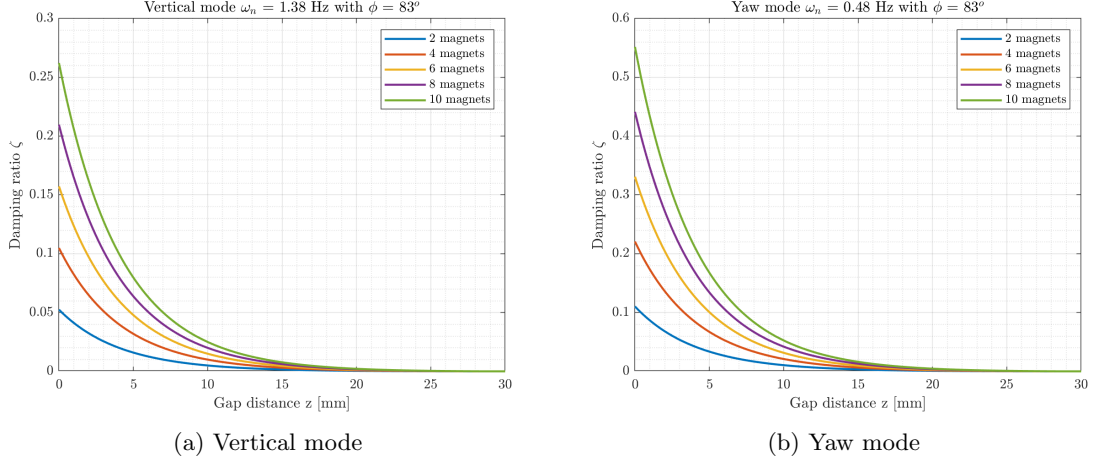
$$\zeta_y = \frac{C_y}{C_y^{\text{crit}}} \tag{4.55}$$

where C_y^{crit} is the critical damping for yaw mode whose derivation is shown in Equation 2.51. With the average distance from the Cu stage's centroid to the center of magnet to be 1.7 in, we can calculate the critical damping for yaw mode as $C_y^{\text{crit}} = 32.553\,\text{kg/s}$. Figure 4.9b shows the relationship between the damping ratio for yaw mode and the gap distance from the magnet's top surface. In addition, multiple magnets can be used, and the damping ratio is multiplied by the corresponding number of magnets for which the linear relationship between them is also assumed.

4.5.3 Time Domain Responses

Once the damping ratios are calculated and plotted against the gap distance, we can decide the right amount of damping needed for the VIS. In turn, this decision dictates the nominal gap as well as the number of magnets for the overall design. With 8 magnets at 3-4 mm under the Cu stage, the damping ratio is approximately 0.1 for the vertical mode and 0.2 for the yaw mode, which seems appropriate by earlier discussion at the beginning of this chapter. Using these parameters and the ODE derived in Chapter 2 for each mode, we can rewrite the ODEs for time domain simulations.

Using Equation 2.4 for the ODE form of the vertical mode, replacing the damping coefficient C_v by the damping ratio ζ_v and the critical damping C_v^{crit}, and using the vertical stiffness K_v of the angled spring configuration highlighted in Equation 2.25, we have

$$M\ddot{z} + C_v\dot{z} + K_v z = 0 \tag{4.56}$$

$$M\ddot{z} + 2\zeta_v\sqrt{K_v M}\dot{z} + K_v z = 0 \tag{4.57}$$

$$M\ddot{z} + \left(2\zeta_v\sqrt{nk\sin\phi M}\right)\dot{z} + (nk\sin\phi)\,z = 0 \tag{4.58}$$

Defining the state vector as

$$\mathbf{x}_v = \begin{bmatrix} \dot{z} \\ z \end{bmatrix} \tag{4.59}$$

we can solve Equation 4.58 in the time domain with a displacement initial condition of $2\,\mathrm{mm}$ by a simple script in MATLAB® using `ode45`. Figure 4.10a shows the normalized displacement response versus time. It takes the stage approximately 5-6 s to settle with an overshoot of about 70%.

(a) Vertical mode
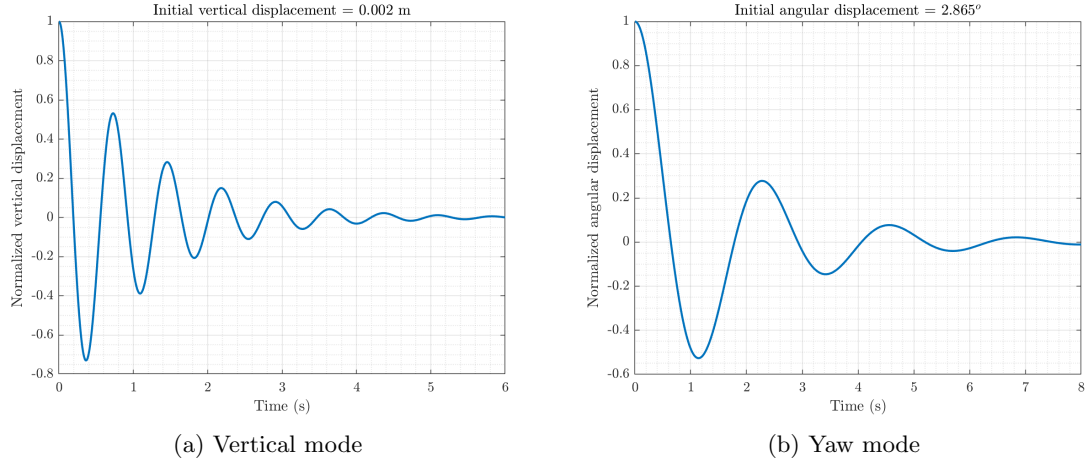
(b) Yaw mode

Figure 4.10: Responses in time domain

Similarly, using Equation 2.43 for the ODE form of the yaw mode as well as replacing the damping coefficient C_y by the damping ratio ζ_y and the critical damping C_y^{crit}, we have

$$\bar{I}_z \ddot{\theta} + \zeta_y C_y^{\mathrm{crit}} \bar{R}^2 \dot{\theta} + \left(\frac{n}{2} k R_s^2 \cos \phi \right) \theta = 0 \tag{4.60}$$

$$\bar{I}_z \ddot{\theta} + \left(2 \zeta_y \sqrt{\bar{I}_z \kappa} \right) \dot{\theta} + \left(\frac{n}{2} k R_s^2 \cos \phi \right) \theta = 0 \tag{4.61}$$

$$\left(\frac{1}{2} M R_s^2 \right) \ddot{\theta} + \left[2 \zeta_y \sqrt{\left(\frac{1}{2} M R_s^2 \right) \left(\frac{n}{2} k R_s^2 \cos \phi \right)} \right] \dot{\theta} + \left(\frac{n}{2} k R_s^2 \cos \phi \right) \theta = 0 \tag{4.62}$$

Defining the state vector as

$$\mathbf{x}_y = \begin{bmatrix} \dot{\theta} \\ \theta \end{bmatrix} \tag{4.63}$$

we can solve Equation 4.62 in the time domain with an angular displacement initial condition of 0.05 rad (or 2.865°) by a simple script in MATLAB® using `ode45`. Figure 4.10b shows the normalized angular displacement response versus time. It takes the stage approximately 7-8 s to settle with an overshoot of about 55%.

The simulations in the time domain are not fully captured on paper because we can use MATLAB® to make an animation for each mode to visualize how the Cu stage responses under each initial condition. Appendix I provides a snippet of the animation script, including the GIF generation code, used to produce such animation.

Chapter 5

CONCLUSION

5.1 Summary

That was quite a journey to get through many different topics! Building a vibration isolation system for sensitive instruments, such as the STM, is a daunting task. Many issues and analyses must be covered to establish the necessary framework because this process will control the designs and material selection. Furthermore, it is important for the designers as well as the end users of the VIS to understand the dynamic concepts and capability of the system so that further improvements in the future can be easily integrated.

In Chapter 1, several designs of VIS and STM are discussed. An effective STM such that both the scanning tip and the material holder stay on the same rigid platform can reduce the complexity of the VIS because the system will less likely suffer from thermal noises due to thermal expansion from different materials. Moreover, a rigid platform allows a better control of where resonances occur so that the system can be tuning to reduce the effects from identifiable vibration sources. A UHV environment provides another layer of vibration isolation since it reduces debris particles, contamination, and vibrations transmitted through air. The Lyding STM by itself is a robust microscope such that it is functional at room temperature with constant height mode (CHM) operation, which is a significant development compared to the first STM developed in the 1980s. However, CHM can easily crash the tip of the microscope if the material's surface is not flat—on the nanoscale, so a functional and effective VIS is still a must for sophisticated operations. For this type of STM, the mass-spring VIS system is chosen to provide a platform for the STM because it is one of the most cost-effective systems to put in a vacuum chamber, especially when the inside of the vacuum chamber is very compact: $14''$ height by $7.5''$ inner diameter. A mass-spring system can also be readily analyzed with fundamental dynamic and vibra-

tion equations from undergraduate-level mechanical engineering classes. This will make the analyses and experiment setups somewhat easier and more straightforward.

In Chapter 2, even though the stage can have up to 6 DOF, only the vertical and yaw modes are chosen for detailed analyses because these are two of the primary mode shapes for systems with long springs and a heavy stage. Moreover, these two modes are mutually exclusive: the eigenvectors representing these modes are mutually orthogonal, which allows us to analyze them separately. The pitch/roll mode is also a primary mode, and they can be analyzed similarly to the vertical mode. A single DOF model for the vertical mode of the mass-spring system is proposed and analyzed to find the relationship between the spring stiffness and the required stage's mass to achieve vibration isolation. This model allows us to derive the displacement transmissibility ratio whose plot then serves as a guidance on choosing the right amount of damping for the vertical mode. The right damping for yaw mode can be found by the same plot and equation because of the similarity in the mathematical derivation. A damping ratio of 0.2 is ideal for both modes. The input frequencies between 1-100 Hz are commonly found in laboratory environment, so the natural frequency for each mode should be designed to be as low as possible. This will allow the crossover—or vibration isolation—to occur early, and low frequency noises can be effectively isolated. Once the suitable spring is selected among thousands of springs from two suppliers, a wooden stage is used to validate the theoretical equations, which confirms that as the stage gets heavier, the lower its natural frequency will be. Since stainless steel outgases much less than music wire, it is the preferred spring material. Commercial springs can suffer from imperfections, such as tolerances in manufacturing wires, which will negatively affect the accuracy of spring stiffness. This leads to the difference in spring stiffness from supplier's data and from our calculations using given spring's dimensions. Consequently, we need to recalculate spring stiffness after purchasing by using the measurement of extended length, which might reflect a more reliable estimate for spring stiffness.

In Chapter 3, FEA is used to investigate the housing for the mass-spring system because 1-DOF analysis is not applicable for such multi-DOF body. Multiple preliminary studies for different concepts are done before the hollow tube is chosen for further FEA

studies. The hollow tube provides exceptional stiffness such that the 1st natural frequency is approximately $540\,\mathrm{Hz}$. This allows the housing to suppress input frequencies of 1-100 Hz from the laboratory environment. In addition, such solid structure separates the natural frequency peaks from each other. More distinctive peaks of the subsequent natural frequencies mean that we can avoid having two adjacent resonance peaks, which can easily amplify noises in the nearby regions of those peaks. The formulation of the finite element method is introduced by using an axial beam, but the process is totally applicable for transverse beam vibration as well. The discussion allows us to justify the choices of element type and the order of shape functions used in the commercial FEA software with GUI like Abaqus. Overall, there are a few residual methods besides the weighted-residual method, and the Galerkin method specifically provides a fairly general framework for the numerical solution of differential equations within the context of the weighted-residual formalization.[30] The finite element method is also used to study Viton, which is a visco-hyperelastic material. A previous study characterizing Viton as a hyperelastic material with Mooney-Rivlin model is used to input material parameters into Abaqus for the natural frequency study. Both in-plane and out-of-plane modes are investigated, and the thicker Viton gasket is preferable since it has higher natural frequencies for out-of-plane modes. This will help us avoid the interference between the low natural frequencies of the thin gasket and the input noises of laboratory environment. Transient modal dynamics in Abaqus is also used to investigate the material response under an impulse load applied to a node. Thicker Viton demonstrates higher damping capability, which can be seen by lower amplitude of sinusoidal response and by faster recovery to equilibrium.

Finally, in Chapter 4, Faraday's law and Lorentz force law are introduced, and they are used as a basis to establish the fundamentals of eddy current and motional damping coefficients. The magnetic flux density $\mathbf{B}$ derived from the current sheet model is numerically calculated in MATLAB®, and the results are then compared to those from an FEA software called FEMM. Once the results for magnetic flux density $\mathbf{B}$ are confirmed, the eddy current density and damping ratio for the transverse vibration of a cantilever beam are calculated to compare with a previously published study. Although several assumptions are used to

simplify the comparative study, the margin of error is very small, which gives us confidence that the codes and calculations work well. For the VIS, an effective area of conductor above the magnet is used to calculate the motional damping coefficients for both vertical and yaw modes. It is recommended that the radius of the conductor's effective area should be twice as large as the radius of magnet. An important observation is that the vertical component of $\mathbf{B}$ does not contribute to the generation of eddy current density for vertical mode, so it is removed from subsequent calculations. This also agrees with the previous study for magnetic damping of the cantilever beam. The damping coefficient is proportional to the velocity for each mode, so magnetic damping can be categorized as viscous damping. Each mode's damping coefficient is then inserted into the corresponding equation of motion to simulate the time domain responses. All equations and formulas derived in this chapter are verified through dimensional analysis for standard SI units, and audience is encouraged to verify them as well.

5.2 FUTURE WORK

Unfortunately, due to COVID-19, a portion of the manufacturing, experiments, and validation work cannot be completed within the time frame allowable for the thesis. However, because most of the important and fundamental studies have been done, we are confident that the system should behave as closely as expected to the analyses. To continue the development of the VIS, the following areas should be addressed to verify the analyses as well as to open new possible research opportunities. Any new fundamental changes must be accompanied by thorough analyses similar to this thesis to avoid any misconceptions.

The mass-spring system, which is the core of the VIS, has been already thoroughly analyzed and designed to meet the criteria for vibration isolation, allowable load for the springs, and spacial tolerances in the vacuum chamber. Further experiments for the 6-spring configuration on the vertical shaker with input frequencies from 1-100 Hz are necessary to confirm the natural frequencies of vertical and yaw modes as well as the crossover frequency. Pitch/roll mode should also be modeled and tested as this is one of the primary modes. In

addition, floor vibration within the Chemistry Lab should be recorded to confirm the input excitation frequencies to the system.

Before manufacturing, the Al hollow tube should be tested, and the frequency response data can be used to compare against the natural frequencies from the FEA model. This allows us to validate material constants, confirm the choices in constructing the FEA model, and fine-tune the desirable sizes and locations of the openings in the tube. Once the Al tube is machined, Viton gaskets should be added one layer at a time to investigate how much damping each layer will contribute to the overall system, and whether thicker Viton positively affects the responses of the VIS in the range of 1-100 Hz. As we discussed, O-rings will be used between all metal-to-metal contacts, so an empirical or FEA study must be done for these sandwiched O-rings as well. In order to characterize the transient response of Viton, we will need to test the material samples separately with the DMTA method and use the test data to extract the material parameters by the curve fitting process with the `fmincon` function in MATLAB®. Alternatively, Abaqus has a built-in table to insert the raw data for the FEA study of visco-hyperelastic materials.

Since we are using the Gauss-Legendre quadrature rules to perform numerical integration for magnetic damping, an additional study is necessary to investigate how many integration points are minimum. A plot highlighting the percentage error and the convergence of results versus the number of Gauss points being used is extremely helpful. To validate the modeling methods, we can purchase the neodymium magnets with a strict control of magnetic strength and measure their remanence by a Gauss meter or a magnetometer. These measurements are critical. This will allow us to verify the calculated magnetic flux density $\mathbf{B}$ from the current sheet model and from the FEMM's FEA model. Similar to the FEA study for the hollow tube that depends largely on the accuracy of Young's modulus of Al, the magnetic damping will be easier to verify once the magnets' strength is confirmed through measurements. Future studies emphasizing on discretizing the conductor domain is imperative to validate the magnetic damping calculations highlighted in this thesis because such thick Cu plate has not been analyzed or experimented before.

BIBLIOGRAPHY

[1] A. M. Baz. *Active and Passive Vibration Damping.* Wiley, 2019.

[2] G. Binnig and H. Rohrer. Scanning Tunneling Microscopy—From Birth to Adolescence. https://www.nobelprize.org/uploads/2018/06/binnig-lecture.pdf, 1986.

[3] G. Binnig, H. Rohrer, C. Gerber, and E. Weibel. Surface Studies by Scanning Tunneling Microscopy. *The American Physical Society*, 1982.

[4] R. G. Budynas and J. K. Nisbett. *Shigley's Mechanical Engineering Design.* McGraw-Hill, 9th edition, 2011.

[5] D. K. Cheng. *Field and Wave Electromagnetics.* Pearson, 2nd edition, 1989.

[6] S. Chikkamaranahalli, R. Vallance, B. Damazo, and R. Silver. Damping Mechanisms for Precision Applications in UHV Environment. *American Society for Precision Engineering*, 2006.

[7] D. Coyne. *LIGO Vacuum Compatible Materials List.* Laser Interferometer Gravitational-Wave Observatory.

[8] D. J. Craik. *Magnetism: Principles and Applications.* Wiley, 1st edition, 1995.

[9] B. Ebrahimi, M. B. Khamesee, and M. F. Golnaraghi. Design and Modeling of a Magnetic Shock Absorber Based on Eddy Current Damping Effect. *Journal of Sound and Vibration*, 2008.

[10] G. Fantner. *Atomic Force Microscopy.* Advanced Bioengineering Methods Laboratory.

[11] Screw Thread Design. https://www.fastenal.com/en/78/screw-thread-design.

[12] Neodymium Magnet Grades.
https://www.first4magnets.com/tech-centre-i61/information-and-articles-i70/neodymium-magnet-information-i82/grades-of-neodymium-magnets-i92.

[13] E. P. Furlani. *Permanent Magnet and Electromechanical Devices: Materials, Analysis, and Applications.* Academic Press, 1st edition, 2001.

[14] D. J. Griffiths. *Introduction to Electrodynamics.* Pearson, 4th edition, 2013.

[15] T. J. R. Hughes. *The Finite Element Method: Linear Static and Dynamic Finite Element Analysis.* Prentice-Hall Inc., 1st edition, 1987.

[16] D. J. Inman. *Engineering Vibration.* Pearson, 4th edition, 2014.

[17] Instron. Dynamic Mechanical Analysis (DMA). https://www.instron.us/en-us/our-company/library/glossary/d/dma-dynamic-mechanical-analysis.

[18] R. Jakel. Analysis of Hyperelastic Materials with MECHANICA—Theory and Application Examples, 2010.

[19] J. Janninck. Digital Signal Processor Based Control of a Scanning Tunneling Microscope. Master's thesis, University of Illinois at Urbana-Champaign, 1992.

[20] M. Kamermans. Gaussian Quadrature Weights and Abscissae. https://pomax.github.io/bezierinfo/legendre-gauss.html, 2011.

[21] E. P. Kasper and G. J. Hall. *Introduction to the Finite Element Method.* California Polytechnic State University, San Luis Obispo, 2020.

[22] P. Krapf, J. P. Laine, Y. Robach, and L. Porte. Connection of a Scanning Tunneling Microscope with a Molecular Beam Epitaxy Chamber and Analysis of the Vibration Isolation System. *Journal de Physique III*, 1995.

[23] D. Logan. *A First Course in the Finite Element Method.* Thomson, 4th edition, 2007.

[24] J. W. Lyding, S. Skala, J. S. Hubacek, R. Brockenbrough, and G. Gammie. Variable-temperature Scanning Tunneling Microscope. *American Insitute of Physics*, 1988.

[25] A. Makino, W. R. Hamburgen, and J. S. Fitch. Fluoroelastomer Pressure Pad Design for Microelectronic Applications. Technical report, Western Research Laboratory, 1993.

[26] D. Meeker. Finite Element Method Magnetics User's Manual.
https://www.femm.info/Archives/doc/manual42.pdf.

[27] R. Nix. Scanning Probe Microscopy—STM and AFM.
https://chem.libretexts.org/link?25396.

[28] STM Techniques.
https://www.ntmdt-si.com/resources/spm-principles/stm-techniques.

[29] M. Okano, K. Kajimura, S. Wakiyama, F. Sakai, W. Mizutani, and M. Ono.
Vibration Isolation for Scanning Tunneling Microscopy. *Journal of Vacuum Science and Technology A*, 1987.

[30] P. Papadopoulos. *Introduction to the Finite Element Method.* University of California, Berkeley, 2015.

[31] E. Pearse. *Linear Analysis I Lecture Notes.* California Polytechnic State University, San Luis Obispo, 2015.

[32] D. W. Pohl. Some Design Criteria in Scanning Tunneling Microscopy. *IBM Journal of Research and Development*, 1986.

[33] H. Porumamilla. *ME 517 Advanced Vibrations Lecture Notes.* California Polytechnic State University, San Luis Obispo, 2018.

[34] C. Refvem. *Handbook and Reference for the ME 326 Activity.* California Polytechnic State University, San Luis Obispo, 2020.

[35] M. Rijnen. A Numerical and Experimental Study on Passive Damping of a 3D Structure Using Viscoelastic Materials. Master's thesis, Eindhoven University of Technology, 2014.

[36] P. Rivera. Dynamic Response Validation of CubeSats through Testing and Finite Element Analysis. Master's thesis, California Polytechnic State University, San Luis Obispo, 2019.

[37] R. S. Rivlin and D. W. Saunders. Large Elastic Deformations of Isotropic Materials: VII. Experiments on the Deformation of Rubber. *Philosophical Transactions of the Royal Society of London. Series A, Mathematical and Physical Sciences 243.865*, 1951.

[38] M. Sasso, G. Palmieri, G. Chiappini, and D. Amodio. Characterization of Hyperelastic Rubber-like Materials by Biaxial and Uniaxial Stretching Tests Based on Optical Methods. *Polymer Testing*, 2008.

[39] G. Scott. Terrace Ledge Kink Model. https://en.wikipedia.org/wiki/Terrace_ledge_kink_model.

[40] M. Smith. *ABAQUS/Standard User's Manual, Version 6.9.* Dassault Systèmes Simulia Corp, 2009.

[41] H. A. Sodano. *Development of Novel Eddy Current Dampers for the Suppression of Structural Vibrations.* PhD thesis, Virginia Polytechnic Institute and State University, 2005.

[42] TA Instruments. Q8 Dynamic Mechanical Thermal Analyzer Specifications. http://www.tainstruments.com/pdf/brochure/dma.pdf.

[43] R. Turnbull, R. Rahmani, and H. Rahnejat. In-Plane and Out-of-Plane Elastodynamics of Thin Rings and Seals. *Journal of Computational and Nonlinear Dynamics*, 2019.

[44] C. M. A. Vasques, R. A. S. Moreira, and J. D. Rodrigues. Experimental Identification of GHM and ADF Parameters for Viscoelastic Damping Modeling. *European Conference on Computational Mechanics*, 2006.

[45] Y. Yuk and P. Silverman. Scanning Tunneling Microscope Instrumentation. *Review of Scientific Instruments*, 1989.
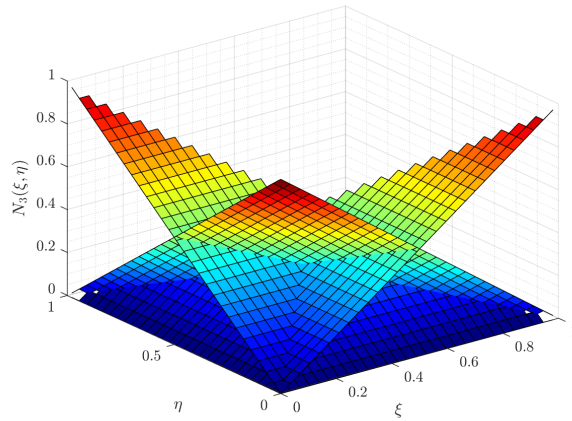
Appendix A

LENGTH AND STIFFNESS CALCULATION FOR SPRINGS

```matlab
function output = spring_length(Load_lbf,Fi_lbf,Lo_in,OD_in,d_in,
    theta_degree,SS)
% Function takes 7 inputs
    % Load_lbf = load per spring [lbf]
    % Fi_lbf = initial tension [lbf]
    % Lo_in = initial length [in]
    % OD_in = outer diameter [in]
    % d_in = wire diameter [in]
    % theta_degree = angle of spring wrt main stage [degree]
    % SS = 1 if spring is stainless steel, 0 if spring is music wire
% Function returns the length of spring in the axial, vetical direction &
    the calculated spring stiffness as output = [axial_length,
    vertical_length, k]

if SS == 1
    % Shigley pg.526. Stainless Steel 302, 304
    G = 10; % [Mpsi]
    E = 28; % [Mpsi]
elseif SS == 0
    if d_in <= 0.032
        % Shigley pg.526. Music Wire A228
        G = 12; % [Mpsi]
        E = 29.5; % [Mpsi]
    elseif d_in  > 0.032 && d_in <= 0.063
        G = 11.85; % [Mpsi]
        E = 29; % [Mpsi]
    elseif d_in > 0.063 && d_in <= 0.125
        G = 11.75; % [Mpsi]
        E = 28.5; % [Mpsi]
    elseif d_in > 0.125
        G = 11.6; % [Mpsi]
        E = 28; % [Mpsi]
    end
end

D = OD_in - d_in;
C = D/d_in; % Spring index
KB = (4*C+2)/(4*C-3); % Max allowable stress
Nb = Lo_in/d_in - 2*C + 1; % # body coils
Na = Nb + G/E; % # active coils
k = ((d_in^4)*G*10^6)/(8*(D^3)*Na); % G in [psi]
y = (Load_lbf - Fi_lbf)/k;
L = Lo_in + y;
axial_length = L;
vertical_length = L*sind(theta_degree);
output = [axial_length, vertical_length, k];

end
```

Appendix B

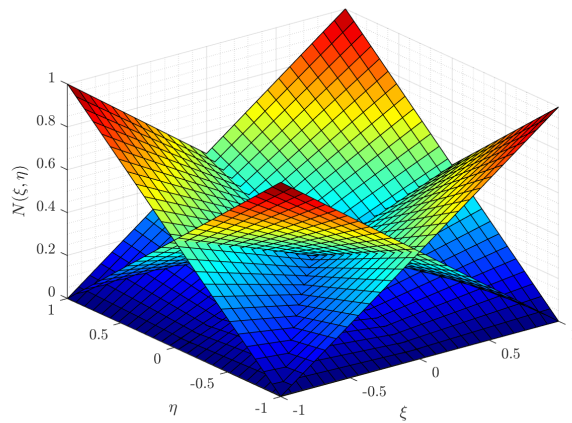## SHAPE FUNCTIONS

```matlab
% Initialize
clearvars; clc; close all;

% Mesh for xi and eta
[xi,eta] = meshgrid(-1:0.08:1);

% Colormap
colormap(jet);

% N1
N1 = 0.25*(1 - xi).*(1 - eta);
figure(1);
subplot(2,2,3);
surf(xi,eta,N1);
grid on; grid minor;
xlabel('$\xi$','interpreter','latex');
ylabel('$\eta$','interpreter','latex');
zlabel('$N_1(\xi,\eta)$','interpreter','latex');
set(gca,'ticklabelinterpreter','latex');

% N2
N2 = 0.25*(1 + xi).*(1 - eta);
subplot(2,2,4);
surf(xi,eta,N2);
grid on; grid minor;
xlabel('$\xi$','interpreter','latex');
ylabel('$\eta$','interpreter','latex');
zlabel('$N_2(\xi,\eta)$','interpreter','latex');
set(gca,'ticklabelinterpreter','latex');

% N3
N3 = 0.25*(1 + xi).*(1 + eta);
subplot(2,2,2);
surf(xi,eta,N3);
grid on; grid minor;
xlabel('$\xi$','interpreter','latex');
ylabel('$\eta$','interpreter','latex');
zlabel('$N_3(\xi,\eta)$','interpreter','latex');
set(gca,'ticklabelinterpreter','latex');

% N4
N4 = 0.25*(1 - xi).*(1 + eta);
subplot(2,2,1);
surf(xi,eta,N4);
grid on; grid minor;
xlabel('$\xi$','interpreter','latex');
ylabel('$\eta$','interpreter','latex');
zlabel('$N_4(\xi,\eta)$','interpreter','latex');
set(gca,'ticklabelinterpreter','latex');

% Combine all shape functions
figure(2);
surf(xi,eta,N1);
hold on;
surf(xi,eta,N2);
surf(xi,eta,N3);
surf(xi,eta,N4);
grid on; grid minor;
colormap(jet);
xlabel('$\xi$','interpreter','latex');
ylabel('$\eta$','interpreter','latex');
zlabel('$N(\xi,\eta)$','interpreter','latex');
set(gca,'ticklabelinterpreter','latex');
```
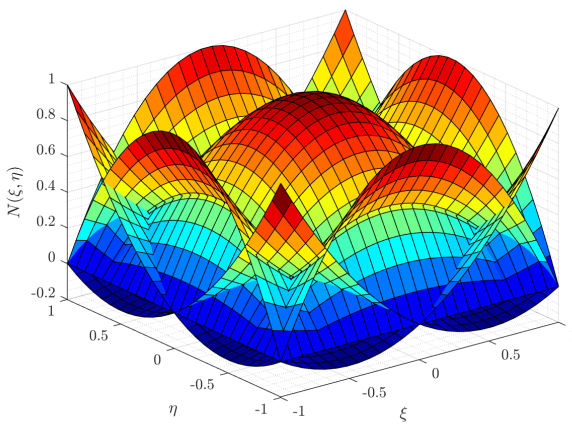
(a) Four linear shape functions for a 4 node element

(b) Four linear shape functions for a 4 node element

(c) Nine quadratic shape functions for a 9 node element

Figure B.1: Combined 2D shape functions

Appendix C

GAUSS-LEGENDRE QUADRATURE RULES

C.1 Derivation of 3-point Gaussian Quadrature Formula

In order to accurately evaluate the integral of a 5th-order polynomial, a Gaussian formula with 3 sampling points must be used. Equation 3.49 is reproduced below

$$\int_{-1}^{1} g(\xi)\, d\xi = \sum_{k=1}^{n_p} g(\xi_k) w_k$$

$$= g(\xi_1)w_1 + g(\xi_2)w_2 + g(\xi_3)w_3 \tag{C.1}$$

where $g(\xi)$ has the form

$$g(\xi) = a_1 + a_2\xi + a_3\xi^2 + a_4\xi^3 + a_5\xi^4 + a_6\xi^5 \tag{C.2}$$

Evaluating the integral on the left-hand side gives

$$\int_{-1}^{1} g(\xi)\, d\xi = a_1\xi\Big|_{-1}^{1} + a_2\frac{\xi^2}{2}\Big|_{-1}^{1} + a_2\frac{\xi^3}{3}\Big|_{-1}^{1} + a_2\frac{\xi^4}{4}\Big|_{-1}^{1} + a_2\frac{\xi^5}{5}\Big|_{-1}^{1} + a_2\frac{\xi^6}{6}\Big|_{-1}^{1} \tag{C.3}$$

$$= 2a_1 + \frac{2}{3}a_3 + \frac{2}{5}a_5 \tag{C.4}$$

Substituting Equation C.2 to the right-hand side of Equation C.1 as well as substituting Equation C.4 to the left-hand side of Equation C.1, we have

$$2a_1 + \frac{2}{3}a_3 + \frac{2}{5}a_5 = w1\left[a_1 + a_2\xi_1 + a_3\xi_1^2 + a_4\xi_1^3 + a_5\xi_1^4 + a_6\xi_1^5\right] \tag{C.5}$$

$$+ w2\left[a_1 + a_2\xi_2 + a_3\xi_2^2 + a_4\xi_2^3 + a_5\xi_2^4 + a_6\xi_2^5\right] \tag{C.6}$$

$$+ w3\left[a_1 + a_2\xi_3 + a_3\xi_3^2 + a_4\xi_3^3 + a_5\xi_3^4 + a_6\xi_3^5\right] \tag{C.7}$$

Collecting like terms gives a system of equations

$$
\begin{cases}
w_1 + w_2 + w_3 = 2 \\[4pt]
w_1\xi_1 + w_2\xi_2 + w_3\xi_3 = 0 \\[4pt]
w_1\xi_1^2 + w_2\xi_2^2 + w_3\xi_3^2 = \dfrac{2}{3} \\[4pt]
w_1\xi_1^3 + w_2\xi_2^3 + w_3\xi_3^3 = 0 \\[4pt]
w_1\xi_1^4 + w_2\xi_2^4 + w_3\xi_3^4 = \dfrac{2}{5} \\[4pt]
w_1\xi_1^5 + w_2\xi_2^5 + w_3\xi_3^5 = 0
\end{cases}
\tag{C.8}
$$

There are too many unknowns in Equation C.8, so we shall assume that the integration points are equally weighted and symmetrically spaced about the origin such that $w_1 = w_3$, $\xi_2 = 0$, and $\xi_1 = -\xi_3$. A reduced system of equations is as follows

$$
\begin{cases}
2w_1 + w_2 = 2 \\[4pt]
2w_1\xi_1^2 = \dfrac{2}{3} \\[4pt]
2w_1\xi_1^4 = \dfrac{2}{5}
\end{cases}
\tag{C.9}
$$

Dividing the second equation by the third equation to solve for ξ_1 and then solving for w_1 and w_2, we have the following results

$$
\begin{cases}
w_1 = \dfrac{5}{9} \\[6pt]
w_2 = \dfrac{8}{9} \\[6pt]
\xi_1 = \pm\sqrt{\dfrac{3}{5}}
\end{cases}
\tag{C.10}
$$

Repeating the process for other sampling points, we can derive other exact expressions, which are shown in Table C.1. Although these exact fractional expressions are helpful, decimal expressions are preferred in reality, especially when higher numbers of integration points are needed since the derivation by hand is quite cumbersome.

C.2 Exact Expressions for the First 5 Gaussian Quadrature Points

Table C.1: Exact expressions for Gauss-Legendre quadrature rules

# of points (n_p)	Coordinates (ξ_k)	Weighting factors (w_k)
1	$\xi_1 = 0$	$w_1 = 2$
2	$\xi_1 = \dfrac{-1}{\sqrt{3}}$	$w_1 = 1$
	$\xi_2 = \dfrac{1}{\sqrt{3}}$	$w_2 = 1$
3	$\xi_1 = -\sqrt{\dfrac{3}{5}}$	$w_1 = \dfrac{5}{9}$
	$\xi_2 = 0$	$w_2 = \dfrac{8}{9}$
	$\xi_3 = \sqrt{\dfrac{3}{5}}$	$w_3 = \dfrac{5}{9}$
4	$\xi_1 = -\sqrt{\dfrac{3}{7} + \dfrac{2}{7}\sqrt{\dfrac{6}{5}}}$	$w_1 = \dfrac{18 - \sqrt{30}}{36}$
	$\xi_2 = -\sqrt{\dfrac{3}{7} - \dfrac{2}{7}\sqrt{\dfrac{6}{5}}}$	$w_2 = \dfrac{18 + \sqrt{30}}{36}$
	$\xi_3 = \sqrt{\dfrac{3}{7} - \dfrac{2}{7}\sqrt{\dfrac{6}{5}}}$	$w_3 = \dfrac{18 + \sqrt{30}}{36}$
	$\xi_4 = \sqrt{\dfrac{3}{7} + \dfrac{2}{7}\sqrt{\dfrac{6}{5}}}$	$w_4 = \dfrac{18 - \sqrt{30}}{36}$
5	$\xi_1 = -\dfrac{1}{3}\sqrt{5 + 2\sqrt{\dfrac{10}{7}}}$	$w_1 = \dfrac{322 - 13\sqrt{70}}{900}$
	$\xi_2 = -\dfrac{1}{3}\sqrt{5 - 2\sqrt{\dfrac{10}{7}}}$	$w_2 = \dfrac{322 + 13\sqrt{70}}{900}$
	$\xi_3 = 0$	$w_3 = \dfrac{128}{225}$
	$\xi_4 = \dfrac{1}{3}\sqrt{5 - 2\sqrt{\dfrac{10}{7}}}$	$w_4 = \dfrac{322 + 13\sqrt{70}}{900}$
	$\xi_5 = \dfrac{1}{3}\sqrt{5 + 2\sqrt{\dfrac{10}{7}}}$	$w_5 = \dfrac{322 - 13\sqrt{70}}{900}$

Appendix D

MODE SHAPES OF 1/16-INCH VITON GASKET
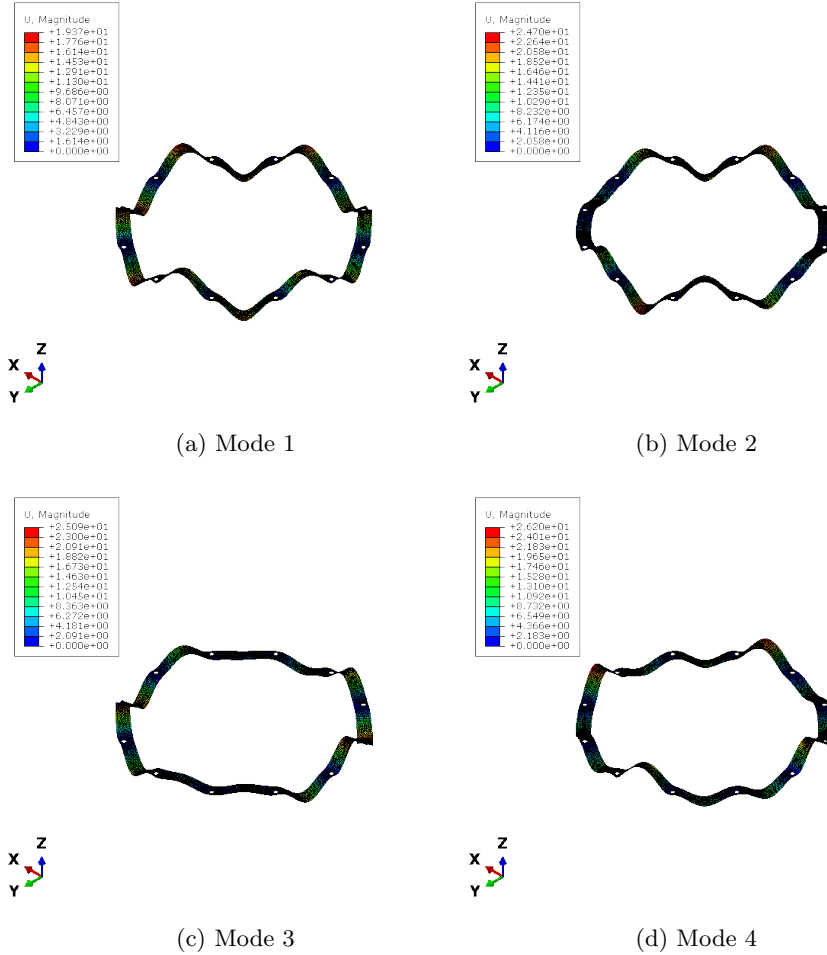

(a) Mode 1

(b) Mode 2

(c) Mode 3

(d) Mode 4

Figure D.1: First 4 out-of-plane mode shapes of the 1/16-inch Viton gasket

Appendix E

FREQUENCY DOMAIN MEASUREMENT TECHNIQUES FOR THE
DYNAMIC PROPERTIES OF VISCOELASTIC MATERIALS

E.1 Dynamic, Mechanical, and Thermal Analyzer (DMTA)

A dynamic mechanical thermal analysis is often used to obtain the Young's modulus of the materials as a function of temperature or frequency.[35] A sample is held in place, and an oscillating force is applied to the sample. The oscillating response is then recorded, and modulus can be calculated from the elastic response whereas damping is calculated from the viscous response.[17] The phase lag will be 0° for purely elastic materials while it will be 90° for purely viscous materials. Viscoelastic materials will exhibit an intermediate phase difference.[42] There are multiple modes of deformation depending on how the materials are used: dual/single cantilever, 3-point bend, shear sandwich, etc. Figure E.1 shows an example of the equipment from TA Instruments.
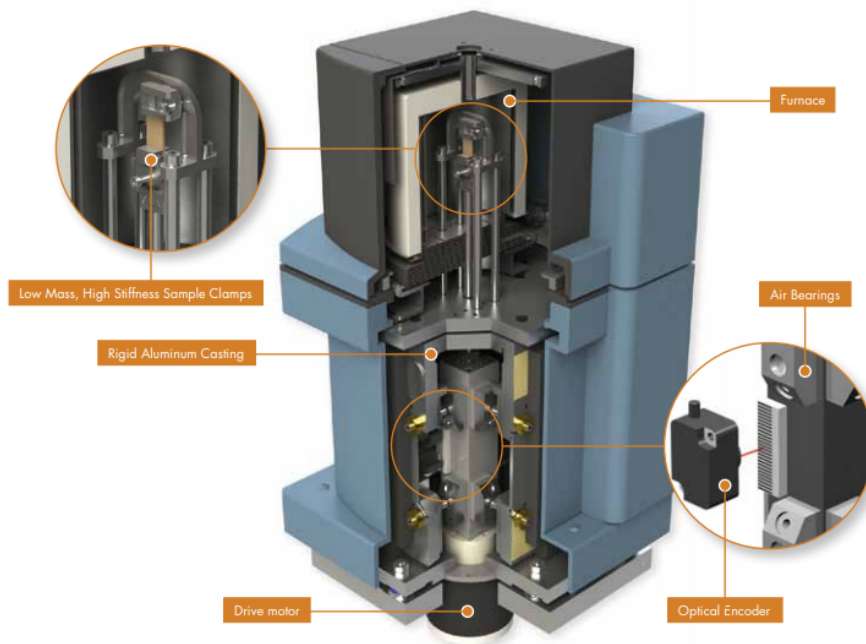

Figure E.1: DMTA measurement system

DMTA differs from other mechanical testing devices in two important ways.[42] First, typical tensile test devices focus only on the elastic component. In many applications, the inelastic, or viscous component, is critical. It is the viscous component that determines properties such as impact resistance. Second, tensile test devices work primarily outside the linear viscoelastic range. DMA works primarily in the linear viscoelastic range and is therefore more sensitive to structure.

E.2 OBERST BEAM

While the DMTA method is classified as a non-resonant technique, the Oberst beam method belongs to the class of resonant methods.[1] In this method, the beam is excited by a non-contact exciter, and the response is monitored by an accelerometer. The excitation can be a swept sinusoidal or random in nature. Depending on how the viscoelastic layers are configured in the beam, the extracted parameter can be either tensile or shear modulus. The method is adopted by The American Society for Testing and Materials as a standard test procedure for quantifying the damping characteristics of viscoelastic materials (ASTM E 756-93). Figure E.2 shows the schematic drawing of the Oberst beam test setup.
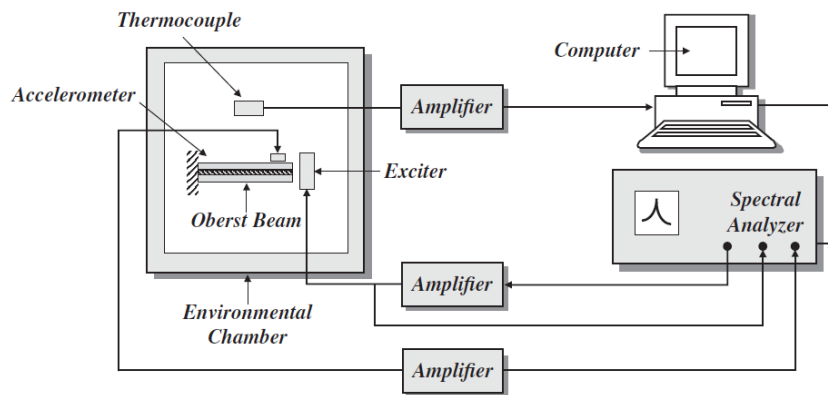

Figure E.2: Oberst beam test setup

Appendix F

CALCULATING MAGNETIC FLUX DENSITY B

```matlab
%% Magnetic Field Density B Calculation
function [B] = magfield_current(para,r,z)

%% Extract parameters
L = para.L; % length of magnet
rmag = para.rmag; % radius of magnet
mu0 = para.mu0;
M0 = para.M0;

%% Equivalent current from magnetization
I = M0*L;

%% Warning for z < L/2
for zi = 1:length(z)
    if z(zi) < L/2
        disp('[WARNING] B field is calculated within magnet.');
        disp('[WARNING] Check space grid for z again.');
        pause;
    end
end

%% Call Gauss function
G = 7;
[wt,m] = gaussquad(G);
zp = (L/2)*m;

%% Calculate Br & Bz
for zi = 1:length(z)
    for ri = 1:length(r)
        for Gi = 1:G
            % Compute elliptic integrals
            k2 = 4*rmag*r(ri)/((rmag + r(ri))^2 + (z(zi) - zp(Gi))^2);
            [K,E] = ellipke(k2);

            % Compute Br
            Br_integrand = ((z(zi) - zp(Gi))/(r(ri)* ...
                sqrt((rmag + r(ri))^2 + (z(zi) - zp(Gi))^2)))* ...
                (-K + E*(rmag^2 + r(ri)^2 + (z(zi) - zp(Gi))^2)/ ...
                ((rmag - r(ri))^2 + (z(zi) - zp(Gi))^2));
            Bri(Gi,1) = (L/2)*(mu0*I/(2*pi*L))*Br_integrand*wt(Gi);

            % Compute Bz
            Bz_integrand = (1/(sqrt((rmag + r(ri))^2 + (z(zi) ...
                - zp(Gi))^2)))*(K + E*(rmag^2 - r(ri)^2 - (z(zi) - ...
                zp(Gi))^2)/((rmag - r(ri))^2 + (z(zi) - zp(Gi))^2));
            Bzi(Gi,1) = (L/2)*(mu0*I/(2*pi*L))*Bz_integrand*wt(Gi);
        end
        % Sum them up
        B.Br(zi,ri) = sum(Bri);
        B.Bz(zi,ri) = sum(Bzi);
    end
end

end
```

CALCULATING & PLOTTING EDDY CURRENT DENSITY

```matlab
%% Find J for vertical mode
rstart = 1e-9;
rend = 2*para.rout;
r = linspace(rstart,rend,rn);
zdot = fn(1)*(0.001);
[Binf] = magfield_current(para,r,zstart);
[Bfit] = magfield_current(para,2*para.rout - r,zstart);
Jinf = para.sigma*Binf.Br*zdot;
Jimg = para.sigma*Bfit.Br*zdot;
for ri = 1:length(r)
    if r(ri) <= para.rout
        rJ(1,ri) = r(ri);
        if Jinf(ri) <= Jimg(ri)
            Jfit(1,ri) = 0;
        else
            Jfit(1,ri) = Jinf(ri) - Jimg(ri);
        end
    end
end

%% Plot J for vertical mode
figure(1);
plot(r*10^3,Jinf,':','linewidth',1.5,'displayname','$J_{infinite}$');
hold on;
plot(r*10^3,Jimg,':','linewidth',1.5,'displayname','$J_{imaginary}$');
plot(rJ*10^3,Jfit,'linewidth',1.5,'displayname','$J_{finite}$');
grid on; grid minor;
set(gca,'ticklabel','latex');
xlim([0 2*para.rout*10^3]);
legend('location','north','interpreter','latex');
xlabel('r [mm]','interpreter','latex');
ylabel('Eddy current density J [$A/m^2$]','interpreter','latex');
plot([0 para.rout*10^3],[-0.001*max(Jinf) -0.001*max(Jinf)],'color','k',...
    'linewidth',2,'handlevisibility','off'); % plot conductor
text(para.rout*10^3,-0.07*max(Jinf),'$\uparrow$ $r_{conductor}^{projected}$'...
    ,...
    'fontsize',9,...
    'verticalalignment','bottom','horizontalalignment','center',...
    'interpreter','latex'); % text box for conductor
plot([0 para.rmag*10^3],[-0.01*max(Jinf) -0.01*max(Jinf)],'color','r',...
    'linewidth',2,'handlevisibility','off'); % plot magnet
text(para.rmag*10^3,-0.08*max(Jinf),'$\uparrow$ $r_{magnet}$',...
    'fontsize',9,'color','r',...
    'verticalalignment','bottom','horizontalalignment','center',...
    'interpreter','latex'); % text box for magnet
title(strcat('Vertical velocity $\dot{z}$ =',...
    sprintf(' %.2f',zdot*10^3),' mm/s'),...
    'interpreter','latex');
hold off;

%% Find J for yaw mode
rstart = 1e-9;
rend = 2*para.rout;
r = linspace(rstart,rend,rn);
thetadot_lg = fn(1)*(0.001);
[Binf] = magfield_current(para,r,zstart);
[Bfit] = magfield_current(para,2*para.rout - r,zstart);
Jinf = para.sigma*sqrt(Binf.Bz.^2*thetadot_lg^2 + Binf.Br.^2*thetadot_lg^2);
Jimg = para.sigma*sqrt(Bfit.Bz.^2*thetadot_lg^2 + Bfit.Br.^2*thetadot_lg^2);
for ri = 1:length(r)
    if r(ri) <= para.rout
        rJ(1,ri) = r(ri);
        if Jinf(ri) <= Jimg(ri)
            Jfit(1,ri) = 0;
        else
            Jfit(1,ri) = Jinf(ri) - Jimg(ri);
```

```matlab
66            end
67        end
68  end
69
70  %% Plot J for yaw mode
71  figure(2);
72  plot(r*10^3,Jinf,':','linewidth',1.5,'displayname','$J_{infinite}$');
73  hold on;
74  plot(r*10^3,Jimg,':','linewidth',1.5,'displayname','$J_{imaginary}$');
75  plot(rJ*10^3,Jfit,'linewidth',1.5,'displayname','$J_{finite}$');
76  grid on; grid minor;
77  set(gca,'ticklabel','latex');
78  xlim([0 2*para.rout*10^3]);
79  legend('location','north','interpreter','latex');
80  xlabel('r [mm]','interpreter','latex');
81  ylabel('Absolute Eddy current density J [$A/m^2$]','interpreter','latex');
82  plot([0 para.rout*10^3],[-0.001*max(Jinf) -0.001*max(Jinf)],'color','k',...
83      'linewidth',2,'handlevisibility','off'); % plot conductor
84  text(para.rout*10^3,-0.07*max(Jinf),'$\uparrow$ $r_{conductor}^{projected}$'...
        ,...
85      'fontsize',9,...
86      'verticalalignment','bottom','horizontalalignment','center',...
87      'interpreter','latex'); % text box for conductor
88  plot([0 para.rmag*10^3],[-0.01*max(Jinf) -0.01*max(Jinf)],'color','r',...
89      'linewidth',2,'handlevisibility','off'); % plot magnet
90  text(para.rmag*10^3,-0.08*max(Jinf),'$\uparrow$ $r_{magnet}$',...
91      'fontsize',9,'color','r',...
92      'verticalalignment','bottom','horizontalalignment','center',...
93      'interpreter','latex'); % text box for magnet
94  title(strcat('Tangential arc velocity $\dot{\theta}$ =',...
95      sprintf(' %.2f',thetadot_lg*10^3),' mm/s'),...
96      'interpreter','latex');
97  hold off;
```

Appendix H

CALCULATING MOTIONAL DAMPING COEFFICIENT

```matlab
%% Find motional damping coefficient caused by Eddy Current from 1 magnet
function [Cver,Crot] = motionalcoeff(para,z)

%% Extract parameters
sigma = para.sigma;
del = para.del;
rout = para.rout;
rin = para.rin;

%% Call Gauss function
G = 10;
[wt,m] = gaussquad(G);
rm = ((rout - rin)/2)*m + (rout + rin)/2;

%% Find integral for infinite plate from 1 magnet
for Gi = 1:G
    % Find B at the quadrature point
    [Binf] = magfield_current(para,rm(Gi),z);

    % Find Cver at quadrature points
    Iver_inf_i(Gi,1) = rm(Gi)*(Binf.Br^2)*((rout-rin)/2)*wt(Gi);

    % Find Crot at quadrature points
    Irot_inf_i(Gi,1) = rm(Gi)*(Binf.Br^2 + Binf.Bz^2)*((rout-rin)/2)*wt(Gi);
end

% Sum them up
Iver_inf = sum(Iver_inf_i);
Irot_inf = sum(Irot_inf_i);

%% Find integral for imaginary eddy current from 1 magnet
for Gi = 1:G
    % Find B at the quadrature point
    [Bimg] = magfield_current(para,2*rout-rm(Gi),z);

    % Find Cver at quadrature points
    Iver_img_i(Gi,1) = rm(Gi)*(Bimg.Br^2)*((rout-rin)/2)*wt(Gi);

    % Find Crot at quadrature points
    Irot_img_i(Gi,1) = rm(Gi)*(Bimg.Br^2 + Bimg.Bz^2)*((rout-rin)/2)*wt(Gi);
end

% Sum them up
Iver_img = sum(Iver_img_i);
Irot_img = sum(Irot_img_i);

%% Find overall vertical motional damping coeff using the image method
if Iver_inf - Iver_img <= 0
    Cver = 0;
else
    Cver = sigma*(2*pi)*del*(Iver_inf - Iver_img);
end

%% Find overall rotational motional damping coeff using the image method
if Irot_inf - Irot_img <= 0
    Crot = 0;
else
    Crot = sigma*(2*pi)*del*(Irot_inf - Irot_img);
end

end
```

ANIMATION CODE FOR TIME DOMAIN RESPONSES

```matlab
%% Prep for animation window
w = stage_radius*2*10^3; [mm]
h = 0.0254*10^3; [mm]

% Define plot size
figure(3);
set(gcf,'position',[250 200 1200 600]);

% Define x-related variables for vertical mode
xcenter = 0;
x1 = xcenter - w/2;
x2 = xcenter + w/2;
x3 = xcenter + w/2;
x4 = xcenter - w/2;
X = [x1 x2 x3 x4 x1];

% Define y-related variables for vertical mode
ycenter = z(1,2)*10^3;
y1 = ycenter - h/2;
y2 = ycenter - h/2;
y3 = ycenter + h/2;
y4 = ycenter + h/2;
Y = [y1 y2 y3 y4 y1];

% Normalize parameters time subplot for vertical mode
timenorm_z = t_z/tspanz(2);
posnorm_z = z(1,2)/y0(2,1);

% Normalize parameter for time subplot for yaw mode
timenorm_theta = t_theta/tspantheta(2);
posnorm_theta = theta(1,2)/theta0(2,1);

% Position subplot for vertical mode
subplot(2,2,1);
z1 = plot(X,Y,'linewidth',1.5,'color',[0.8500 0.3250 0.0980]);
hold on;
z2 = plot(xcenter,ycenter,'.','markersize',15,'color',[0 0.4470 0.7410]);
grid on; grid minor;
axis equal;
xlim([-0.6*w 0.6*w]);
ylim([-0.8*h 0.8*h]);
xlabel('X distance (mm)','interpreter','latex');
ylabel('Y distance (mm)','interpreter','latex');
set(gca,'ticklabel','latex');
tt1 = title(sprintf('Time = %.1f s',t_z(1)),'interpreter','latex');
hold off;

% Time subplot for vertical mode
subplot(2,2,2);
z3 = plot(timenorm_z(1),posnorm_z(1),'.','markersize',15);
hold on;
z4 = plot(timenorm_z(1),posnorm_z(1),'linewidth',0.7,'color',[0 0.4470
    0.7410]);
grid on; grid minor;
axis equal;
xlim([0 tspanz(2)]);
ylim([-1 1]);
xlabel('Time (s)','interpreter','latex');
ylabel('Normalized amplitude','interpreter','latex');
set(gca,'ticklabel','latex');
title(strcat('Initial vertical displacement = ',...
    sprintf(' %.3f',y0(2)),' m'),...
    'interpreter','latex');
hold off;

% Position subplot for yaw mode
```

```matlab
subplot(2,2,3);
t1 = plot(stage_radius*10^3*cos(theta0(2)),stage_radius*10^3*sin(theta0(2)),...
    '.','markersize',15);
hold on;
pos = [-stage_radius -stage_radius stage_radius*2 stage_radius*2]*10^3;
t2 = rectangle('Position',pos,'Curvature',[1 1],'linewidth',1.5,'edgecolor'...
    ,[0.8500 0.3250 0.0980]);
axis equal;
grid on; grid minor;
xlim([-0.6*w 0.6*w]);
ylim([-0.35*stage_radius*10^3 0.35*stage_radius*10^3]);
xlabel('X distance (mm)','interpreter','latex');
ylabel('Y distance (mm)','interpreter','latex');
set(gca,'ticklabel','latex');
tt2 = title(sprintf('Time = %.1f s',t_theta(1)),'interpreter','latex');
hold off;

% Time subplot for yaw mode
subplot(2,2,4);
t3 = plot(timenorm_theta(1),posnorm_theta(1),'.','markersize',15);
hold on;
t4 = plot(timenorm_theta(1),posnorm_theta(1),'linewidth',0.7,'color',[0
    0.4470 0.7410]);
grid on; grid minor;
axis equal;
xlim([0 tspantheta(2)]);
ylim([-1 1]);
xlabel('Time (s)','interpreter','latex');
ylabel('Normalized amplitude','interpreter','latex');
set(gca,'ticklabel','latex');
title(strcat('Initial angular displacement = ',...
    sprintf(' %.3f',theta0_deg),'$^o$'),...
    'interpreter','latex');
hold off;

%% Update vertical animation
figure(3);
tic;
for ni = 1:length(t_z)
    % Update position-related variables for vertical mode
    ycenter = z(ni,2)*10^3;
    y1 = ycenter - h/2;
    y2 = ycenter - h/2;
    y3 = ycenter + h/2;
    y4 = ycenter + h/2;
    Y = [y1 y2 y3 y4 y1];

    % Update position subplot for vertical mode
    z1.YData = Y;
    set(tt1,'string',sprintf('Time = %.1f s',t_z(ni)));
    z2.YData = ycenter;

    % Update time-related variables for vertical mode
    timenorm_z = t_z(ni)/tspanz(2);
    posnorm_z = z(ni,2)/y0(2,1);
    timeseries_z(ni,1) = timenorm_z;
    posseries_z(ni,1) = posnorm_z;

    % Update time subplot for vertical mode
    set(z3,'xdata',timenorm_z*tspanz(2),'ydata',posnorm_z);
    set(z4,'xdata',timeseries_z*tspanz(2),'ydata',posseries_z);

    % Control frame
    pause(0.0030);

    % Store frames
    frame1(ni,1) = getframe(figure(3));

end
toc;
clear timeseries_z posseries_z;

%% Update yaw animation
```

```matlab
136  figure(3);
137  tic;
138  for mi = 1:length(t_theta)
139      % Update position subplot for yaw mode
140      t1.XData = stage_radius*cos(theta(mi,2))*10^3;
141      t1.YData = stage_radius*sin(theta(mi,2))*10^3;
142      set(tt2,'string',sprintf('Time = %.1f s',t_theta(mi)));
143
144      % Update time-related variables for yaw mode
145      timenorm_theta = t_theta(mi)/tspantheta(2);
146      posnorm_theta = theta(mi,2)/theta0(2,1);
147      timeseries_theta(mi,1) = timenorm_theta;
148      posseries_theta(mi,1) = posnorm_theta;
149
150      % Update time-subplot routine for yaw mode
151      set(t3,'xdata',timenorm_theta*tspantheta(2),'ydata',posnorm_theta);
152      set(t4,'xdata',timeseries_theta*tspantheta(2),'ydata',posseries_theta);
153
154      % Control frame
155      pause(0.008);
156
157      % Store frames
158      frame2(mi,1) = getframe(figure(3));
159
160  end
161  toc;
162  clear timeseries_theta posseries_theta;
163
164  %% Make GIF
165  % Turn frames to images for vertical mode
166  for g1i = 1:length(t_z)
167      im1{g1i,1} = frame2im(frame1(g1i));
168  end
169
170  % Turn images to GIF for vertical mode
171  count1 = 0;
172  filename = 'animation_full.gif';
173  for g1i = 1:17:size(im1,1)
174      [A,map] = rgb2ind(im1{g1i,1},256);
175      if g1i == 1
176          imwrite(A,map,filename,'gif','LoopCount',Inf,'DelayTime',0);
177      else
178          imwrite(A,map,filename,'gif','WriteMode','append','DelayTime',0);
179      end
180      count1 = count1 + 1;
181  end
182
183  % Turn frames to images for yaw mode
184  for g2i = 1:(length(t_theta))
185      im2{g2i,1} = frame2im(frame2(g2i));
186  end
187
188  % Turn images to GIF for yaw mode
189  count2 = 0;
190  for g2i = 1:9:size(im2,1)
191      [A,map] = rgb2ind(im2{g2i,1},256);
192      if g2i == 2 % don't need this since we append the yaw mode to vertical
                mode
193          imwrite(A,map,filename,'gif','LoopCount',Inf,'DelayTime',0);
194      else
195          imwrite(A,map,filename,'gif','WriteMode','append','DelayTime',0);
196      end
197      count2 = count2 + 1;
198  end
```